STUDY ON THE EFFECTS OF SPACER SHAPE, SPACER GEOMETRY AND REYNOLDS NUMBER IN SPACER-FILLED MEMBRANE CHANNEL USING COMPUTATIONAL FLUID DYNAMICS (CFD)

By

TEOH HUI CHIEH

A thesis submitted to the Department of Chemical Engineering,
Lee Kong Chian Faculty of Engineering and Science,
Universiti Tunku Abdul Rahman,
in partial fulfilment of the requirements for the degree of
Doctor of Philosophy in Engineering
December 2018

ABSTRACT

STUDY ON THE EFFECTS OF SPACER SHAPE, SPACER GEOMETRY AND REYNOLDS NUMBER IN SPACER-FILLED MEMBRANE CHANNEL USING COMPUTATIONAL FLUID DYNAMICS (CFD)

Teoh Hui Chieh

The occurrence of concentration polarisation and fouling phenomena are two major problems that can affect the performance of a membrane and should be minimised whenever possible. It was found in previous literatures that the spacers in a spiral-wound membrane (SWM) can help to reduce these two phenomena at the expense of higher energy consumption. In the present work, the flow hydrodynamics, concentration polarisation and fouling behaviours in a narrow spacer-filled membrane channel were investigated through two-dimensional and three-dimensional models using computational fluid dynamics (CFD) approach. A total of twelve spacer shapes and four flow attack angles were successfully investigated in this work and the results showed that different spacer shapes had different performance in terms of mass transfer, pressure drop, concentration polarisation and fouling control. Arc 0.50 shape spacer, with a flow attack angle of 45°, appeared to be the best design among all the spacers investigated, where it showed potential in improving the performance of membrane processes with a good balance between energy consumption and better control on concentration polarisation and fouling. Arc 0.50 shape had a mass transfer enhancement of 11% and pressure drop reduction of 4% compared to the conventional circle shape spacer. The investigations on the effect of Reynolds number (*Re*) showed that the increase in pressure drop gradient was faster than the decrease in the average concentration polarisation as *Re* increases. This implies the need of a balance between the increases in feed velocity and the increases in pressure drop across a membrane module.

APPROVAL SHEET

This thesis entitled "**STUDY ON THE EFFECTS OF SPACER SHAPE, SPACER GEOMETRY AND REYNOLDS NUMBER IN SPACER-FILLED MEMBRANE CHANNEL USING COMPUTATIONAL FLUID DYNAMICS (CFD)"** was prepared by TEOH HUI CHIEH and submitted as partial fulfilment of the requirements for the degree of Doctor of Philosophy in Engineering at Universiti Tunku Abdul Rahman.

Approved by:

_____

(Dr. LAI SOON ONN) Date:……..
Associate Professor/Supervisor
Department of Chemical Engineering
Lee Kong Chian Faculty of Engineering and Science
Universiti Tunku Abdul Rahman

_____

(Dr. LEE KHIA MIN) Date:……..
Assistant Professor/Co-supervisor
Department of Civil Engineering
Lee Kong Chian Faculty of Engineering and Science
Universiti Tunku Abdul Rahman

LEE KONG CHIAN FACULTY OF ENGINEERING AND SCIENCE

UNIVERSITI TUNKU ABDUL RAHMAN

Date: _____

SUBMISSION OF THESIS

It is hereby certified that Teoh Hui Chieh (ID No: 09UED04930) has completed this thesis entitled "**STUDY ON THE EFFECTS OF SPACER SHAPE, SPACER GEOMETRY AND REYNOLDS NUMBER IN SPACER-FILLED MEMBRANE CHANNEL USING COMPUTATIONAL FLUID DYNAMICS (CFD)**" under the supervision of Dr Lai Soon Onn (Supervisor) from the Department of Chemical Engineering, Lee Kong Chian Faculty of Engineering and Science, and Dr Lee Khia Min (Co-Supervisor) from the Department of Civil Engineering, Lee Kong Chian Faculty of Engineering and Science.

I understand that University will upload softcopy of my thesis in pdf format into UTAR Institutional Repository, which may be made accessible to UTAR community and public.

Yours truly,

_____

(*Teoh Hui Chieh*)

DECLARATION

I hereby declare that the thesis is based on my original work except for quotations and citations which have been duly acknowledged. I also declare that it has not been previously or concurrently submitted for any other degree at UTAR or other institutions.

Name: Teoh Hui Chieh

Date: _____

TABLE OF CONTENTS

LIST OF TABLES

LIST OF FIGURES

LIST OF SYMBOLS / ABBREVIATIONS

A	permeation area, m^2
C_D	drag coefficient
C_{vm}	virtual mass factor
D	diffusion coefficient, m^2/s
d_h	hydraulic diameter, m
d_p	particle diameter, m
d_s	spacer filament diameter, m
d_{ij}	deformation tensor
F_D	drag force, N
F_G	gravitational force, N
F_L	Saffman's lift force, N
F_P	pressure gradient force, N
F_V	virtual mass force, N
g	gravitational acceleration, m/s^2
h_{ch}	channel height, m
J_v	permeation flux, m/s
k	mass transfer coefficient, m/s
l_{ch}	channel length, m
m_{A0}	initial salt mass fraction
m_{Ac}	salt mass fraction adjacent to wall
m_{Aw}	salt mass fraction at wall (membrane)
P	pressure, Pa
Pn	power number
R	rejection coefficient
Re	Reynolds number
R_m	membrane resistance, m^{-1}
Sc	Schimidt number
Sh	Sherwood number
$S_{v,sp}$	specific surface of the spacer, m^{-1}
t	time, s
u_p	particle velocity, m/s
u	velocity components in *X*-direction
v	velocity components in *Y*-direction
w	velocity components in *Z*-direction
V	volume of permeate, m^3
y	species mass fraction
α	flow attack angle, °
δ	concentration boundary layer thickness, m
δ_c	distance between membrane wall and adjacent cell, m
ε	porosity
μ	dynamics viscosity, Pa·s
ρ	fluid density, kg/m^3

ρ_p	particle density, kg/m^3
ν	kinematic viscosity, m^2/s
π	osmotic pressure, Pa
Γ	dimensionless concentration factor

CFD	computational fluid dynamics
GPH	gallons per hour
MF	microfiltration
NF	nanofiltration
RO	reverse osmosis
SPC	specific power consumption
SWM	spiral-wound membrane
TMP	transmembrane pressure
UF	ultrafiltration

CHAPTER 1

INTRODUCTION

1.1 Membrane Processes

Over the past two decades, membrane processes have played an increasingly important role in industrial separation. It can be used in a broad range of applications and has been firmly established as a primary technology for ensuring the purity, safety and efficiency of the treatment of water. One of the advantages of membrane processes compared to conventional separation methods, for example distillation, is that they require lesser energy because membrane processes usually operate at room temperature. In addition, the relatively low capital and operating costs also make membrane processes to be more appealing compared to conventional methods (such as distillation, adsorption, absorption, extraction and stripping), particularly when involving dilute solution (Nath, 2017).

In a membrane separation process (Figure 1.1), a feed mixture consisting of two or more species is separated using a semi-permeable barrier through which some components move faster than the others. The barrier (membrane) is usually a thin, non-porous polymeric film, but it may also be porous polymer, ceramic, or even liquid or gel. The membrane must be strong enough that it will not break, disintegrate or dissolve. The feed that does not pass through the membrane is

known as the retentate, and those that passes through the membrane is known as the permeate.

The optional sweep can be a liquid or gas that facilitates the removal of the permeate.

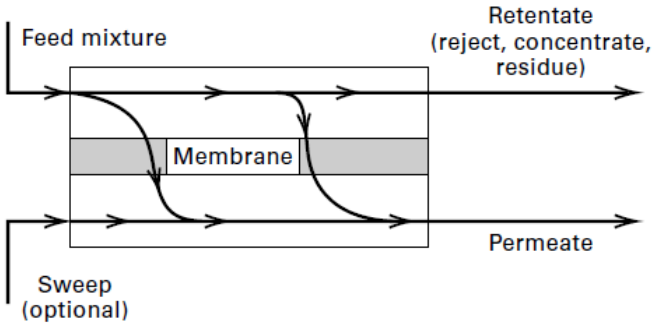

Figure 1.1: Membrane separation process (Henley, Seader and Roper, 2011).

Membrane operations can be divided into four categories according to their driving forces, namely pressure-driven, concentration-driven, electric-potential-driven and temperature-driven. A difference in pressure between two sides of a membrane, i.e. the transmembrane pressure, is the driving force for pressure-driven membrane separations. There are several types of pressure-driven membrane processes such as reverse osmosis (RO), nanofiltration (NF), ultrafiltration (UF) and microfiltration (MF). The basic characteristics of these processes are as shown in Figure 1.2. RO is typically used to remove dissolved salts or ionic solutes from solution and normally operates at very high pressure. NF membranes have pore size in the range of one to tens of nanometres, just slightly larger than that in RO. It is used when high sodium rejection is not required and used most often for water with low total dissolved solids with the

purpose of softening or removal of disinfections. UF and MF processes are similar to NF. Their main differences are the bigger pore size of the membrane and lower transmembrane pressure compared to NF. UF can retain much smaller particles compared to MF. The particles size retain by UF typically is measured by molecular weight, and this process is usually used to purify and concentrate macromolecular (10^3 to 10^6 *Da*) solutions, such as protein solutions. For particles of micron or sub-micron size such as colloids or microorganisms, the separation can be effectively performed using MF.

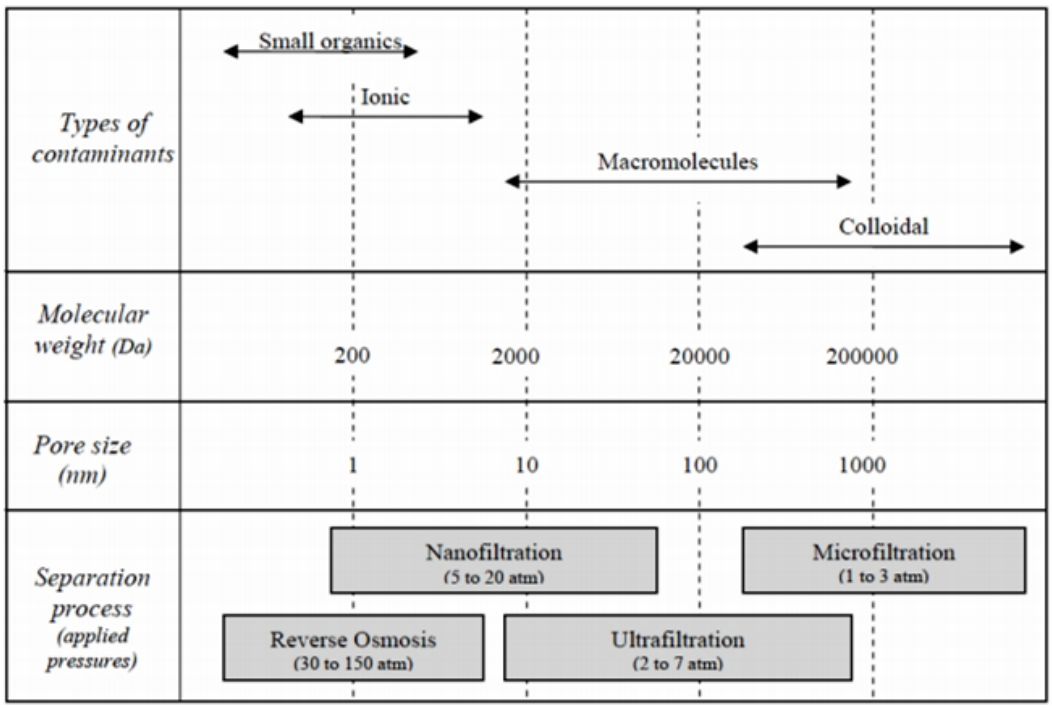

Figure 1.2: Membrane filtration spectrum (Giwa and Ogunribido, 2012).

For concentration-driven membrane operation, mass transfer across the membrane is a consequence of a difference in concentration between the feed and the permeate sides of the membrane. Examples of concentration-driven membrane operation are dialysis, forward osmosis, gas separation and pervaporation. For electric-potential-driven and temperature-driven membrane

operations, mass transfer occurs due to the difference in electric potential and temperature across the membrane, respectively. Electrodialysis is an example of electric-potential-driven membrane operation and membrane distillation is an example of temperature-driven operation.

For industrial scale applications, the usage of membrane by itself during operation are not economical feasible because it requires massive area to achieve the desired outcome. Thus, membranes are usually made into modules to reduce the space they occupy and increase their practicability for use. There are a variety of membrane modules available in today's market to address different needs, and the selection of membrane modules for a particular application depends on their compatibility. There are four primary modules for membrane processes, i.e. spiral-wound, plate-and-frame, hollow-fibre and tubular. Table 1.1 presented the various membrane modules and their general applications in the industries.

Table 1.1: Membrane modules for typical applications (Baker, 2012).

Application	Membrane Module
Reverse Osmosis (seawater, brackish water, industrial water)	Spiral-wound modules dominate. Hollow-fibre is too susceptible to scaling and fouling.
Ultrafiltration	Tubular, hollow-fibre, spiral-wound modules. Tubular generally limited to highly fouling feeds and spiral-wound to clean feeds.
Gas Separation	Hollow-fibre for high volume applications with low flux and low selectivity membranes. Spiral-wound when fluxes are higher and feed gases are more contaminated.
Pervaporation	Most pervaporation systems are small so plate-and frame modules are used.

Although membrane technologies have been widely used in the industries nowadays, membrane fouling and concentration polarisation are still the few critical factors that can reduce the performance of many membrane processes. Fouling is mainly caused by particles deposition on the membrane surface and plugging of membrane pores. Particulates or gels resulting in fouling can enter the process together with the feed, or they may precipitate from the feed solution itself. Due to the flow of fluids or flux through the membrane, the fouling materials tend to move towards the membrane surface and deposit there. Fouling will reduce the effective separation area leading to a reduced flux, and finally the membrane needs to be cleaned or replaced. The cleaning or replacement of a membrane will interrupt the operation of normal process and thus increase the cost of operation.

Concentration polarisation phenomenon occurs when a membrane is permeable to a certain solute and relatively impermeable to another, and the impermeable molecules will accumulate at the membrane surface causing their concentration at the surface to increase in a “polarisation layer”. A concentration gradient is then formed at the location adjacent to the membrane surface. If the concentration of the impermeable component reached its solubility limit on the membrane, a precipitation gel may form and result in fouling on the membrane surface or within its pores. Concentration polarisation phenomenon will reduce the flux and subsequently the performance of the membrane process. This phenomenon is most common in pressure-driven membrane separation such as ultrafiltration and reverse osmosis.

1.2 Computational Fluid Dynamics Studies in Membrane Processes

Computational fluid dynamics (CFD) can be used to model the flow and concentration polarisation phenomenon or fouling in a membrane narrow channel or module. The parameters that affect the performance of a membrane process are usually non-linear and are suitable to be solved using numerical simulation such as CFD approach. CFD simulation is an attractive approach because it not only yields a better understanding of the phenomena involved in membrane processes, but also minimises the number of experiments needed to explore a wide range of parameters. Experimental studies may only provide qualitative information on fouling phenomena and concentration polarisation, whereas CFD simulation offers the possibility to model various situations with minimal cost (Karabelas, Kostoglou and Koutsou, 2015). The adoption of CFD over the recent years has increased, as conducting experiments usually involve higher costs and more time consumption. With the enhancement of computing power and efficiency, CFD has become an effective tool to achieve the objective of a better design, especially in spacer design, for spiral-wound membrane (SWM) process.

Numerous CFD works have been carried out in two dimensions (2D) due to its simplicity and smaller computational demands. These 2D CFD studies provided insights into the effect of spacer geometry for different spacers, indicating that careful selections of spacer thickness, spacing, shape and configuration are crucial for minimising fouling and concentration polarisation phenomenon (Shakaib et al., 2009; Li et al., 2012; Saeed et al., 2012; Amokrane, et al., 2015a).

The three-dimensional (3D) qualitative results presented by Koutsou, Yiantsios and Karabelas (2007) had provided a better insight compared to 2D models with regard to the phenomena taking place in a spacer-filled channel and enhanced the understanding of how spacer configurations influenced the eddies formation and ultimately affected the fouling layer. Rahimi et al. (2009) attempted to explore the ability of 3D CFD modelling in predicting membrane fouling. They successfully employed the discrete phase model to study the particle deposition pattern on the membrane surface. The predicted particle deposition pattern showed that membrane surface with lower shear stress exhibited higher tendency for fouling to occur. Both their CFD prediction and experimental observation confirmed that membrane surface did not foul uniformly, but depending on the flow hydrodynamics. Bucs et al. (2015) also performed a 3D CFD simulation using the same geometries and flow parameters as their experiments and the simulated results showed good agreement with the experimental results. These previous works support the use of CFD simulation models in the studies of spacer geometrical optimisation and operational conditions of a spiral-wound membrane system.

1.3 Problem Statements

For water treatment applications, spiral-wound membrane modules (SWM) as shown in Figure 1.3 are commonly used because of their high packing density and low cost. It also has advantage over hollow-fibre membranes due to its better fouling control properties. However, in spite of having better fouling

resistance, the occurrence of fouling and concentration polarisation phenomenon in SWM is still inevitable. The extent of fouling and concentration polarisation occuring on a membrane should be minimised whenever possible because they will adversely affect its performance, and hence the permeate flux will be reduced and the lifespan of the membrane will be shortened.

In a spiral-wound membrane module, the membrane layers are wound around a perforated central tube and the adjacent membrane layers are kept apart by spacers to provide a channel for the feed and permeate. The net-type spacers in a SWM, on one hand periodically disrupt the flow resulting in disturbance that can inhibit the development of fouling/concentration polarisation layers that lead to the increase in mass transfer rate, but on the other hand, flow disruption can cause greater extent of pressure drop resulting in higher energy consumption. This situation calls for a balance between the desired increase in mass transfer and the undesired increase in energy consumption. Therefore, spacer designs which can promote mass transfer, while minimising energy consumption will result in economic improvements for a membrane process.

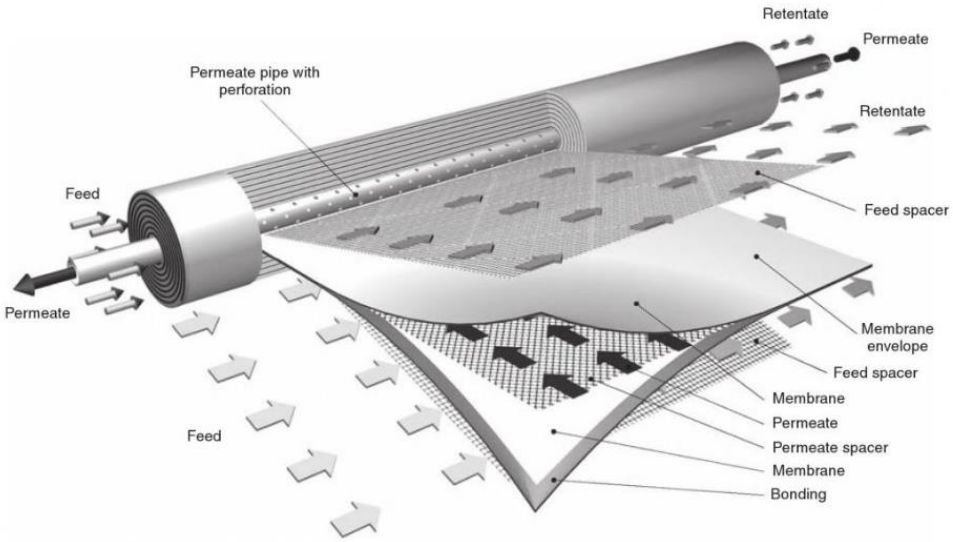

Figure 1.3: Spiral-wound membrane module (Drioli and Giorno, 2010).

1.4 Research Aim and Objectives

Since the important role of spacers in reducing fouling and concentration polarisation phenomenon in a spiral-wound membrane module as mentioned in the previous section has been recognised, the aim of this research focused on studying the effects of spacer parameters on mass transfer enhancement, fouling/concentration polarisation tendency and energy consumption. New spacer designs were developed to search for the optimum spacer parameters that trade-off between the increase in mass transfer and the reduction of fouling/concentration polarisation tendency and energy consumption. The objectives of the research as listed below were carried out by simulating two-dimensional (2D) and three-dimensional (3D) models using computational fluid dynamics (CFD) approach to examine the conditions in a narrow spacer-filled channel.

The objectives of the research were:

1. Investigate the effects of spacer shape on fluid flow, pressure drop, mass transfer, concentration polarisation and particle deposition on membrane using 2D and 3D CFD simulations.
2. Investigate the effects of spacer geometry (flow attack angle) on fluid flow, pressure drop, mass transfer, concentration polarisation and particle deposition on membrane using 2D and 3D CFD simulations.
3. Study the effects of Reynolds number on fluid flow, pressure drop, mass transfer, concentration polarisation and particle deposition on membrane using 2D CFD simulations.

4. Determine the optimum spacer parameters from this work that balance between the increase in mass transfer, and the reduction in fouling/concentration polarisation tendency and pressure drop.

1.5 Contribution of Study

The efficiency of a membrane process can be increased and the lifespan of a membrane module can be prolonged with improved spacer design that is capable of reducing fouling and concentration polarisation phenomenon. Improved spacer design is also able to reduce energy consumption of a membrane separation process by reducing the pressure drop across the membrane module.

CHAPTER 2

LITERATURE REVIEW

2.1 Feed Spacers in Spiral Wound Membrane

In recent years, spiral wound membrane (SWM) module has becomes the most dominant module in a very broad range of water treatment facilities and desalination. A typical spiral wound membrane module is schematically shown in Figure 1.3. The feed spacer functions as a device to separate the two adjacent membrane layers and at the same time provides a narrow channel for the feed to flow across the membrane. The presence of feed spacer poses obstacles to the fluid flow and hence it can disrupt the bulk flow within the channel. This disruption on one hand is desired because it can promotes mixing due to the formation of eddies which can help in reducing concentration boundary layer and improve mass transfer. Schock and Miquel (1987) had long ago investigated the mass transfer in a channel with and without spacers and found that the measured Sherwood numbers in a spacer-filled channel were significantly higher than an empty channel. But on the other hand, flow instabilities and resistance induced by the feed spacer will cause higher increase in pressure drop, and this is associated with higher increase in operational cost.

Therefore, a high performance feed spacer must be able to yield a good balance between mass transfer enhancement and pressure drop. Although the

design of such feed spacer can be a sophisticated task as the correlation between mass transfer and pressure drop is not straightforward and the fluid hydrodynamics in a spacer-filled channel can be complicated, fortunately with the fast pace of advancement in computing power in the current era, a wide range of spacer designs as discussed in the subsequent sections can be explored more efficiently through numerical simulations such as computational fluid dynamics (CFD) to search for optimum spacer's parameters for a given application.

For the past decades, intensive researches had been devoted to seek detailed understanding on the impact of spacers on fluid dynamics, concentration polarisation and fouling behaviour in a spacer-filled membrane channel (Cao, Wiley and Fane, 2001; Schwinge, Wiley and Fletcher, 2002; Neal, et al., 2003; Geraldes, Semião and de Pinho, 2004; Ahmad and Lau, 2006; Wardeh and Morvan, 2008; Guillen and Hoek, 2009; Koutsou, Yiantsios and Karabelas, 2009; Lau, et al. 2010; Saeed, et al., 2012; Radu, et al. 2014; Haaksman, et al. 2017). A consensus of opinions among the researchers was established in which an optimum spacer design exists for a particular operating condition that can provide good mass transfer rate and fouling control at minimal energy consumption. Over the years, researchers had also done quite a number of reviews on the progress of the impact of spiral-wound membrane's feed spacer characteristics on pressure drop, concentration polarisation and fouling control so as to provide a bigger picture of the works done and the opportunities that exist for further improvement (Schwinge, et al. 2004; Fimbres-Weihs and Wiley, 2010; Karabelas, et al., 2015; Abid, et al., 2017).

2.2 Studies on the Effect of Spacer Shape

In the current market, most of the spacers in commercial spiral wound membranes are of circular shape. However, there are no rules of any standard shape requirement on the spacers, thus one can be creative and propose various kinds of possible shape and investigate their effects on the flow hydrodynamics, concentration polarisation and fouling behaviour. In view of this, researchers have been continuously studying the performance of various novel spacer shapes, either experimentally or through numerical simulation, with the aim to obtain a better performance spacer.

Earlier works by Dendukuri, Karode and Kumar (2004) and Ahmad, Lau and Abu Bakar (2005) had investigated the effect of spacer shapes on the flow hydrodynamics, pressure drop and the tendency of concentration polarisation in a spacer-filled membrane channel. Dendukuri, Karode and Kumar (2004) proposed new design of spacers by making the convex surface of a circular spacer to be concave so as to create favourable flow conditions, and showed that the new spacers could reduce the pressure drop across the channel as compared to circular spacer.

Ahmad, Lau and Abu Bakar (2005) utilised 2D CFD simulations to investigate the effect of different spacer shapes (circular, triangular and square as shown in (Figure 2.1) on concentration polarisation behaviour with Reynolds number ranging from 400 to 1000. Their results found that triangular spacer shape exhibited the highest ability to reduce concentration polarisation but also

exhibited the highest degree of pressure drop. It is noted by the researchers that in order to control concentration polarisation phenomenon with minimal energy consumption, the design of spacer must be carefully evaluated.

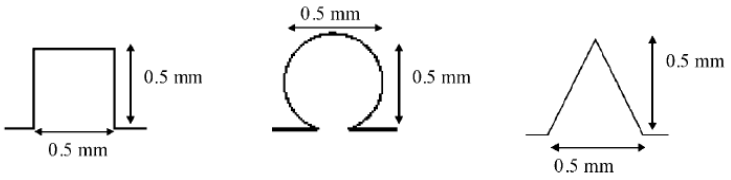

Figure 2.1: Spacer of different shapes as investigated by Ahmad, Lau and Abu Bakar (2005).

Teoh and Lai (2014) noted the different effects of spacer shape on velocity profile, wall shear stress and pressure drop, thus in their work, they combined various spacer shapes into a channel, namely combination of triangle and circle shape, and combination of triangle and square shape, to take advantage of the different characteristics offered by different spacer shapes. They found that the combination of triangle and circle spacers provided lower energy consumption compared to channel with purely triangle spacers. The results indicated the potential of spacer shape combination in a membrane module.

Amokrane, et al. (2015b) developed a 2D numerical model to study the impact of ellipse and oval spacer shapes on concentration polarisation behaviour and pressure drop for spacers arranged in zig-zag configuration. Based on their numerical prediction, the new spacer designs were more superior to the conventional circular shape spacer whereby pressure drop was minimised, probability of fouling was decreased and mass transfer was enhanced.

2.3 Studies on the Effect of Spacer Geometry

2.3.1 Spacer Filament Angles

Conventional spacer is made up of two layers (the bottom filament layer and the top filament layer) on top of each other (non-woven type) in which both of the filaments are perpendicular to each other. Nevertheless, the angle between these two layers (the internal angle) can be manipulated to achieve the desired performance. Apart from the internal angle, the angle of the spacer filament with respect to the feed flow direction (flow attack angle) also can be adjusted so that the spacer can be positioned at a desired angle with the incoming flow (Figure 2.2). The changes in both the internal angle and flow attack angle can alter the direction of the flow and also the fluid velocity, resulting in different behaviours of concentration polarisation and fouling condition.

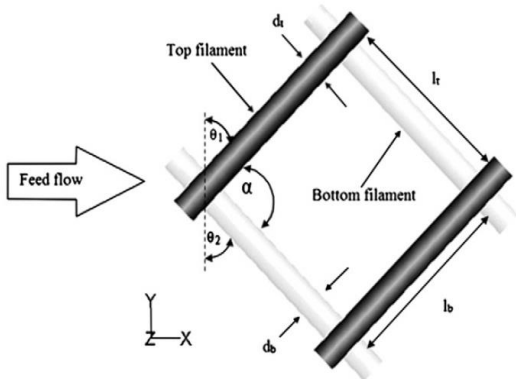

Figure 2.2: Spacer filament angles, α and θ as defined by Saeed, et al. (2012).

Varying the spacer filament angles to evaluate its impact on pressure drop, mass transfer, concentration polarisation and fouling control are often been

treated as one of the important criteria to be studied by many researchers (Da Costa and Fane, 1994; Neal, et al., 2003; Shakaib et al., 2007; Koutsou et al., 2009; Siddiqui, et al., 2016).

Lau, et al. (2009) used a 3D laminar transient hydrodynamics modelling approach and validated them against experimental results to determine an optimised mesh angle for feed spacer in SWM. The mesh angle is described by two parameters, i.e. α and β, where α is the angle between the upper and lower spacer filaments and β is the angle between the spacer and the mean flow direction. They concluded that spacer with different mesh angles would cause different extent of disruption on concentration polarisation layer under particular energy consumption. Based on their simulated results, spacer with α of 120° and β of 30° was the optimal parameter that yielded the highest magnitude of unsteady hydrodynamics with moderate pressure loss and demonstrated the minimum effective concentration polarisation factor. Nevertheless, Karabelas, et al. (2015) commented that the optimum mesh angle as proposed by Lau, et al. (2009) would introduce asymmetric flow in the channel that would be a detrimental feature of exhibiting an uneven fouling condition on the two membrane surfaces. This would consequently cause unequal lifespan of the membranes due to uneven deteriorating rates.

Saeed, et al. (2012) attempted to study the effect on flow pattern by manipulating the spacer filament angle and found that the generation of secondary flow patterns which could be helpful for self sustaining cleaning on membrane was greatly influence by the flow attack angle. They concluded that

the optimisation of spacer filament angle could lead to enhanced membrane performance through generation of desirable flow pattern within the membrane channel. Their investigation also found higher pressure drop for spacer filaments that were inclined more towards the channel axis.

Chaumeil and Crapper (2013) used a 3D CFD model coupled with discrete element method to numerically model the initial colloidal size particles deposition on non-woven membrane spacers. They found that when flow attack angle bisected the spacers' angle, deposition of particles increased around the spacer joint, whereas deposition occurred uniformly on the spacer when the spacer was aligned with the feed direction. An evaluation of particle deposition patterns in SWM channel was performed by Radu, et al. (2014) and their in-situ observations on particle deposition in the experimental flow cell which could very well be described by their 3D CFD modelling, also revealed that feed spacer orientations had an effect on the formation of specific fouling patterns.

Gurreri, et al. (2016) found that flow attack angle of 45° will have more displacement in the lateral direction hence lesser stagnant area in the channel. They concluded that woven spacer with length over height ratio of 2 and flow attack angle of 45° demonstrated the most promising parameters to provide better mixing in the membrane channel. It was also found that these parameters exhibited the highest Sherwood number under all the cases investigated in this work. Gu, Adjiman and Xu (2017) investigated the impact of feed spacer geometry (Figure 2.3) with fully woven, partially-woven, middle layer and non-woven arrangements by means of 3D CFD simulations and found that spacers

with mesh angle of 90° exhibited the lowest pressure drop among all the cases investigated in their study.

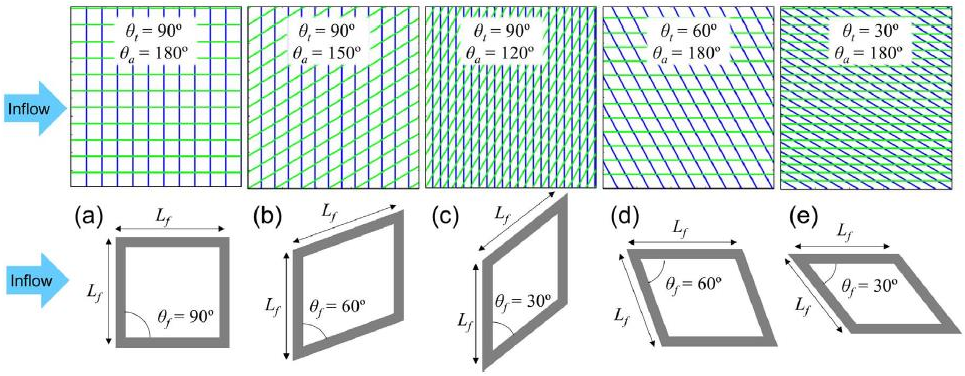

Figure 2.3: Mesh angles and filament arrangements as investigated by Gu, Adjiman and Xu (2017).

2.3.2 Spacer Filament Spacing and Diameter

Spacer filament spacing is the distance between each spacer filament and spacer filament diameter (or sometimes is also referred to as thickness) is the diameter of circular spacer, or for other shapes, the height of the spacer filament. Due to the fact that conventional spacer is made up of two spacer filament layers on top of each other, thus a membrane channel height is usually two times the spacer filament diameter. In literatures, most of the studies on spacer filament spacing (L) are reported as a dimensionless ratio with respect to the spacer filament diameter (D) or the membrane channel height (H), for example, L/D ratio or L/H ratio.

Karode and Kumar (2001) used commercially available spacers which has unequal filament diameters and carried out 3D CFD simulations to study the fluid

flow in a narrow channel. Their simulation results were in good agreement with literature experimental data. Although their findings showed that spacers with unequal diameters (asymmetric spacers) could result in lower pressure drop, the induced shear stresses on the top and bottom membrane surfaces were unequal. They noted that these unequal shear stresses could have different mass transfer characteristics on both sides of the membrane and negatively impacting the membrane module performance.

Earlier work by Schwinge, Wiley and Fletcher, (2002c) showed that although mass transfer increases with the spacer filament diameter, the overall performance indicated by mass transfer enhancement over pressure loss increases at smaller filament diameter. They also found that by decreasing the filament spacing, mass transfer enhancement and pressure loss will increase. However, for cavity and zig-zag configurations, the increase in mass transfer enhancement will reach a maximum value and decreases as the spacing decreases.

Another earlier work by Shakaib, Hasani and Mahmood (2007) found that the effect of spacer filament spacing was less pronounced on pressure drop as compared to the effect of spacer filament diameter. The work by Lau, et al. (2010) involved the simulation and optimisation of spacer filament spacing (Figure 2.4) in SWM using a 2D integrated CFD approach (permeation properties were incorporated with hydrodynamics modelling). They determined that the optimum mesh length ratio to be 3 based on the results of its ability to generate high intensity of unsteady hydrodynamics with the lowest concentration polarisation factor.

Koutsou, Yiantsios and Karabelas (2009) did a 3D systematic study to investigate the effect of Reynolds number and Schmidt number on Sherwood number for a narrow spacer-filled channel. It is evident from their study that spacer geometry had an influence on Sherwood number distribution, where the distribution had a tendency to be shift towards lower values when the *L/D* ratio increases. Another noteworthy result from this study was that the distribution of shear stresses on the channel wall was generally corresponding with the distribution of mass transfer coefficient.

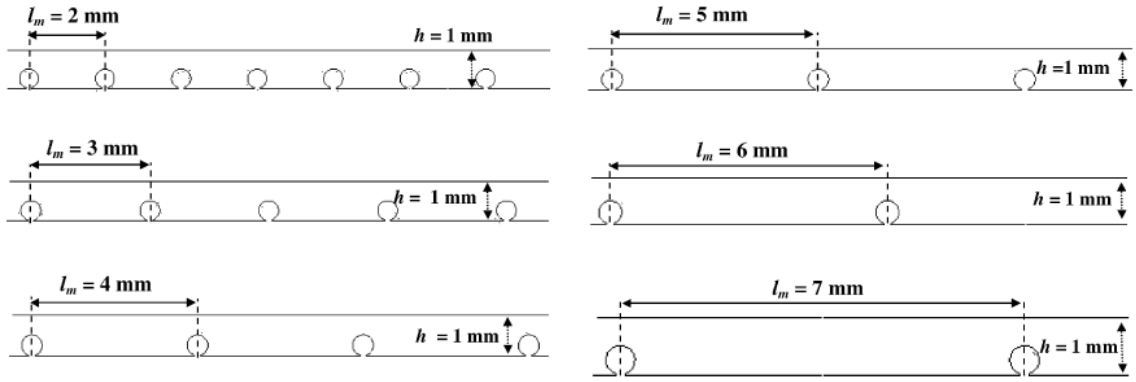

Figure 2.4: Spacer filament spacing as investigated by Lau, et al. (2010).

Kavianipour, Ingram and Vuthaluru (2019) recently investigated the performance of four commercial feed spacers with different geometries using CFD modelling by considering mass transfer and energy consumption, which include parameters such as Sherwood number, pressure drop, specific power consumption, power number etc. Their results found that the Naltex spacer from DelStar Technologies is the best with respect to the parameters investigated and indicated that at low flow rates, large energy savings can be achieved with a small loss in mass transfer performance.

2.4 Studies on the Effect of Spacer Configuration

The top and bottom spacers in a membrane channel can be arranged in a variety of ways such as cavity, zig-zag or submerged (Figure 2.5). These three configurations were the most common types used by researchers in their studies to understand how the arrangement of spacers can affect the flow, mass transfer and fouling conditions (Schwinge, et al., 2003; Li, et al. 2006, 2012; Guillen and Hoek, 2009; Amokrane, et al., 2015a)

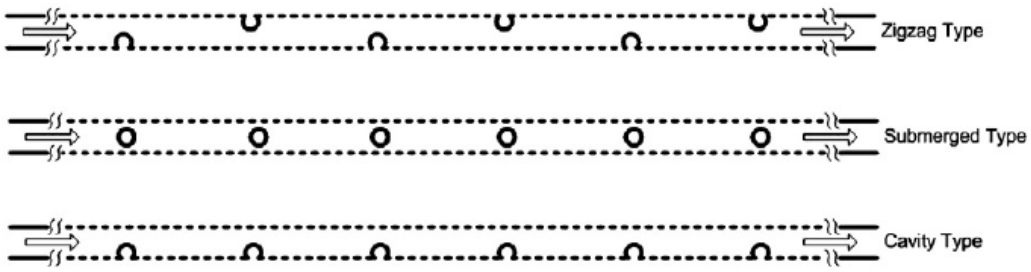

Figure 2.5: Zig-zag, submerged, cavity spacer configurations (Li et al., 2012)

The common opinion by Schwinge, et al. (2002b, c) and Wardeh and Morvan (2008) found that zig-zag configuration was the most efficient arrangement for a spiral-wound membrane module. Li, et al. (2012) simulated particle deposition behaviour using Eulerian-Lagrangian numerical method for four spacer configurations, namely submerged, zig-zag, i-cavity and o-cavity spacer filled channels. Their study took the effect of curvature into account and revealed that particle deposition profile was affected by the variations in curvature. They also found that zig-zag configuration was best at reducing the influence of channel curvature and particle deposition on the membrane for a given permeation rate and feed velocity.

The work by Amokrane, et al. (2015a) found that the presence of wall eddies could enhance mass transfer for both zig-zag and submerged configurations that were their under investigation. For submerged configuration, the axial profile of time-average mass transfer coefficient was relatively uniform compared to zig-zag configuration which was much more non-uniform due to recirculation regions before and after the spacer. Their findings show that zig-zag configuration resulted in greater mass transfer coefficient and smaller pressure drop compared to submerged case.

2.5 Studies on the Effect of Non-Conventional Spacer

Apart from the conventional two-layer spacer filament that lies on top of each other, the filaments can weave like fabrics (woven spacers) or a layer of filament can "pass through" the centre of another filament layer to provide more complex geometries such as those shown in Figure 2.6. The spacer filament layers also not necessary to be constructed only in two layers, but can be more, such as the three-layer design by Schwinge, Wiley and Fane (2004b). One of the advantages of using numerical simulation to study the effect of these non-conventional spacers is that it allows the researchers to construct model of complex spacer geometries that are currently not available in the market and offer the capabilities to manipulate the influencing parameters.

Schwinge, Wiley and Fane (2004b) were among the early researchers that proposed a more complicated spacer design compared to conventional one. In

this study, their experimental results showed that the advanced 3-layer spacer that they had fabricated has lesser fouling tendency and superior mass transfer characteristics (up to 20% higher flux) as compared with conventional 2-layer type. The 3-layer spacer reduced the membrane area covered by spacer filaments and hence increased the flux. However, the pressure loss for the new spacer was higher due to the additional transverse filament that caused higher flow resistance. Although the researchers noted the disadvantages of increased pressure loss and difficulties in the spacer fabrication, overall it still can be a promising economic advantage due to the higher flux that it can produced.

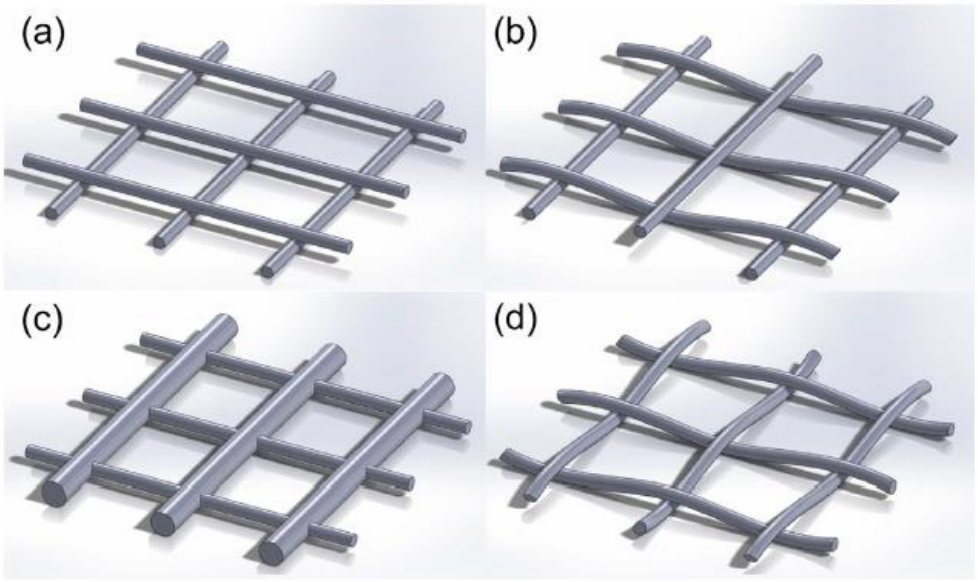

Figure 2.6: Spacer filament arrangement: (a) non-woven, (b) partially woven, (c) middle layer and (d) fully woven (Gu, Adjiman and Xu, 2017).

A novel spacer was designed by Koutsou and Karabelas (2015) which comprised of spherical nodes connected with cylindrical filaments (Figure 2.7). The key feature of this design was a much smaller contact-region (contact point nodes) with the membrane compared to conventional longer filament contact-

region (contact lines). Filament contact-region is undesired because it can create stagnant zones that promote concentration polarisation and fouling. Direct numerical simulations revealed that this novel spacer exhibited broader distributions of time-averaged parameters such as fairly uniform shear stress and mass transfer distributions, and regions of zero values were of very limited extend. The absence of stagnant zones also suggested that this design will exhibit improved performance regarding fouling. Experiments had also been conducted and the results were in agreement with the simulation findings.

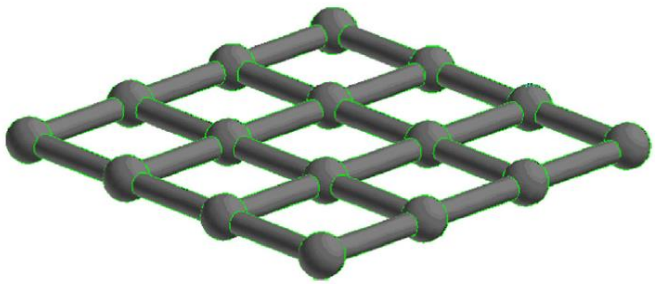

Figure 2.7: A novel spacer geometry as investigated by Koutsou and Karabelas (2015).

Li, et al. (2016) has introduced some flexible and dynamics structures into the spacer mesh known as “hairy structures”. Their experimental results indicate that the hairy structure vibrations may enhance the flux up to ~ 20% and could have big impact on the mass transfer in the vicinity of the membrane surface.

Recently, Gu, Adjiman and Xu (2017) investigated the effect of feed spacer with fully woven, partially-woven, middle layer and non-woven arrangements (Figure 2.6) using 3D CFD simulations and found that fully woven spacers outperform the other spacer arrangements in mitigating concentration polarisation.

During the fabrication of SWM, in order to achieve module compactness, the spacers are subjected to compressive stresses that can cause spacers deformation and affect the performance of a membrane process. Karabelas, Koutsou and Sioutopoulos (2018) presented a comprehensive method, which involved both computational and experimental methods, to study the effect of these stresses on their impact on a SWM module, such as spacer compaction, membrane indentations, effective channel-gap, and flow pressure drop.

2.6 Studies on the Effect of Feed Reynolds Number

Although the feed spacer parameters have an impact on the membrane module performance, the feed flow rate or velocity also play an important role in the effectiveness of the module. Feed velocity usually is reported in Reynolds number, typically using the relationship introduced by Schock and Miquel (1987), so that it can take into account the different geometries of spacer and membrane channel and thus can provide a consistent comparison between various geometries.

A study conducted by Ahmad, Lau and Abu Bakar (2005) had investigated the effect of different spacer shapes and Reynolds number ranging from 400 to 1000 on concentration polarisation behaviour. They found that the optimum spacer geometries depend on the Reynolds number, where circular shape was recommended for high flow rate processes due to lower energy consumption and triangular and square shapes were better for low flow rate

processes because they could offer better gain in concentration polarisation reduction compared to moderate increase in pressure drop.

Gurreri, et al. (2016) carried out 3D CFD simulations of a spacer-filled channel with a variety of spacer parameters such as woven/non-woven spacers, spacer filament spacing, flow attack angle and Reynolds numbers (1, 4, 16. 64). In all the cases, the flow was found to be steady. Creeping flow condition were observed for low Reynolds number and secondary flow started to develop as Reynolds number increases and mixing enhancement was obtained. At very low Reynolds number, the presence of spacers mainly act as resistances that hindered mass transfer; only beyond a specific cut-off value of Reynolds number did spacers provide mass transfer enhancement.

In the recent study by Kavianipour, Ingram and Vuthaluru (2017), they used 3D CFD simulations to study the effect of Reynolds number on various spacer configurations and their results were validated against the works by previous researchers. The performance of the membrane was found to be strongly affected by Reynolds number in the range of 50 to 200 and also the spacer geometry. The study also found that the ranking of a better spacer design in improving the membrane performance may change with Reynolds number, showing that Reynolds number could also be an important parameter to consider when designing the feed spacer.

CHAPTER 3

METHODOLOGY

3.1 Introduction

This chapter describes the fundamentals and techniques used in computational fluid dynamics (CFD) to simulate the fluid flow in a spacer-filled narrow membrane channel with mass transfer, concentration polarisation and fouling phenomena included. It presents the theory of CFD, investigated parameters (mass transfer, concentration polarisation and fouling), and detailed approaches used in the simulations to obtain the data in this research. The experimental setup used to validate the simulation results was described at the end of this chapter.

3.2 CFD Theory

Transport processes can be described by equations obtained from mass, momentum and energy balances. These are partial differential equations which can only be solved analytically for simple cases. For complex cases, the system is usually solved numerically. Computational fluid dynamics (CFD) is a technique that uses numerical analysis and computer power to numerically solve the equations of continuity, momentum, energy and species transport.

The continuity equation represents the conservation of mass and is given as

$$\frac{\partial \rho}{\partial t} + \nabla \cdot (\rho \mathbf{u}) = 0 \tag{3.1}$$

where ρ is fluid density, t is time and $\mathbf{u}$ is fluid velocity vector (ANSYS® FLUENT® Theory Guide, 2016).

The Navier-Stokes equations represent the conservation of momentum and they govern the motion of fluids. They can be viewed as Newton's second law of motion for fluids and for a compressible Newtonian fluid, it is given as

$$\left[\frac{\partial}{\partial t}(\rho \mathbf{u}) + \nabla \cdot (\rho \mathbf{u}\mathbf{u})\right] = -\nabla P + \nabla \cdot \left[\mu\left((\nabla \mathbf{u} + \nabla \mathbf{u}^T) - \frac{2}{3}\nabla \cdot \mathbf{u}\mathbf{I}\right)\right] + \rho \mathbf{g} + \mathbf{F} \tag{3.2}$$

where μ is fluid dynamic viscosity, P is fluid pressure and $\mathbf{I}$ is identity matrix. The terms on the left correspond to inertial forces, while the terms on the right correspond to pressure forces, viscous forces, gravitational body force and external body forces, respectively (ANSYS® FLUENT® Theory Guide, 2016).

The species transport equation is given as

$$\frac{\partial}{\partial t}(\rho y_i) + \nabla \cdot (\rho \mathbf{u} y_\mathbf{i}) = \nabla \cdot (\rho D_{i,m} \nabla y_i) \tag{3.3}$$

where y_i is mass fraction of species i and $D_{i,m}$ is the mass diffusion coefficient for species i in the mixture (ANSYS® FLUENT® Theory Guide, 2016).

3.3 CFD Simulation Procedures

In general, performing a CFD analysis is divided into three main steps: (1) pre-processing, (2) solving and (3) post-processing. In the pre-processing step, the geometry and mesh were created, the physical models and boundary conditions were specified and the numerical options were chosen. The mathematical inputs from the pre-processor were then organised into numerical arrays and were solved iteratively. Finally, the results from simulation were processed and analysed in the form of contour plots, vector plots, streamlines, line charts and bar charts.

3.3.1 Computational Domains

The spacer-filled narrow membrane channel geometries were created using ANSYS® DesignModeler™ application, which is a part of the analysis in ANSYS® Workbench™.

3.3.1.1 2D Channel Geometry and Spacer Configurations

The two-dimensional (2D) computational domain comprised of a rectangular channel 31.5 mm long (*X*-direction) and 1 mm high (*Y*-direction). The

channel was filled with 5 spacers of different configurations (cavity and zig-zag) as shown in Figure 3.1. Each spacer had the same height of 0.5 mm. The first spacer was located 5 mm from the inlet face and the last spacer was located 10 mm from the outlet face to eliminate the effect of entrance and exit on the fluid flows. The distance between each spacer was fixed to 4 mm.

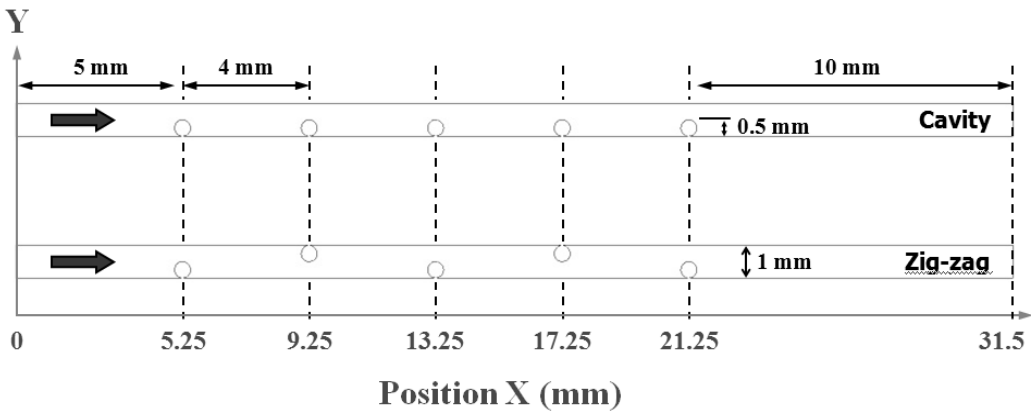

Figure 3.1: 2D channel geometry and spacer configurations.

3.3.1.2 3D Channel Geometry and Spacer Geometry

The three-dimensional (3D) computational domain as shown in Figure 3.2 comprised of a cuboid channel 23 mm long (*X*-direction), 8 mm wide (*Z*-direction) and 1 mm high (*Y*-direction). The observation channel had a length in the *X*- and *Z*-direction of 8 mm and a height of 1 mm in the *Y*-direction. The observation channel was located 5 mm from the inlet face and 10 mm from the outlet face to eliminate the effect of entrance and exit on the fluid flows. The observation channel was filled with two bottom spacers and two top spacers with different flow attack angles, α (Figure 3.3) in cavity configuration as shown in Figure 3.4.

Each spacer had the same height of 0.5 mm and the distance between each spacer was fixed to 4 mm.

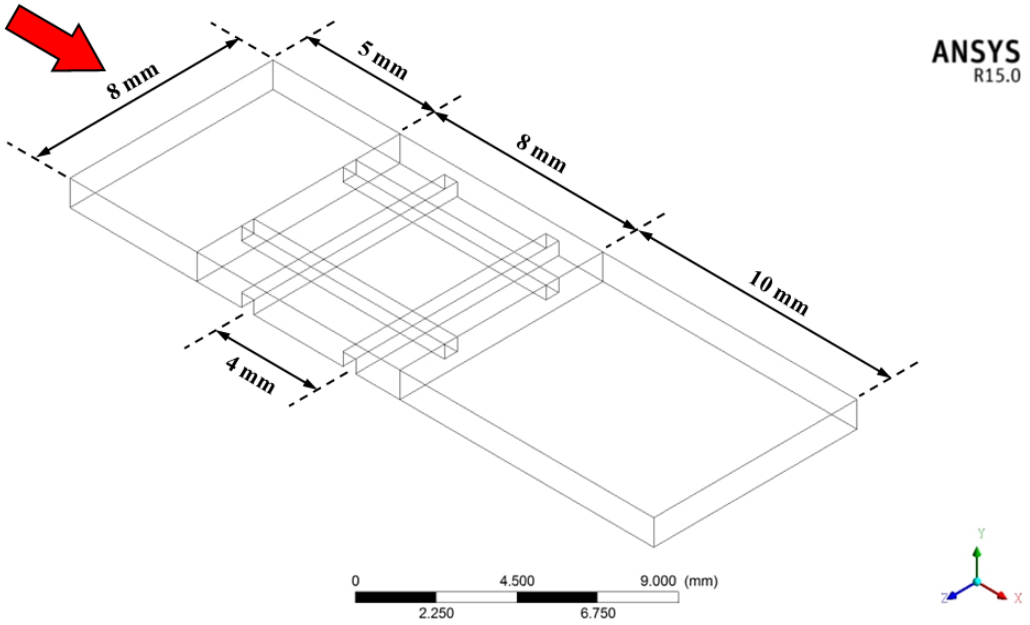

Figure 3.2: 3D channel geometry.

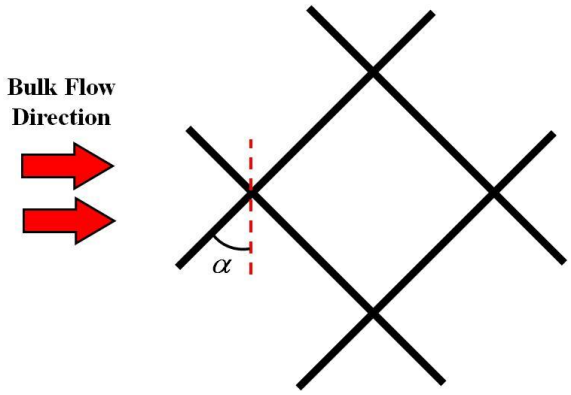

Figure 3.3: Flow attack angle, α.

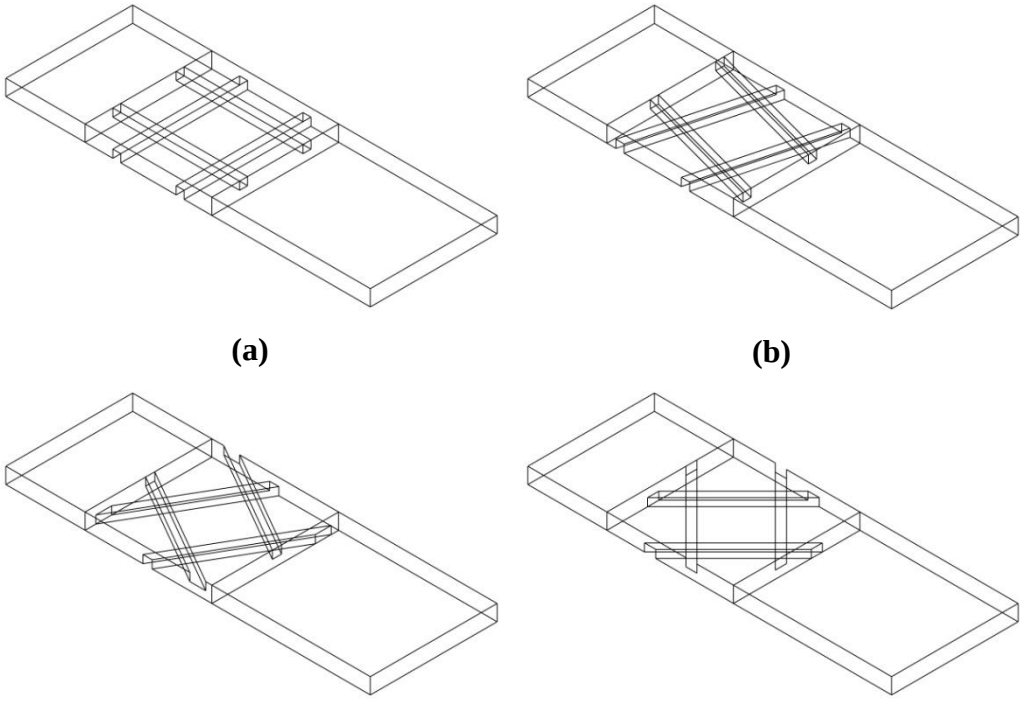

(a) **(b)**

(c) **(d)**

Figure 3.4: Spacers in 3D channel with flow attack angle, α of (a) 90°, (b) 15°, (c) 30° and (d) 45°.

3.3.1.3 New Spacer Designs

Previous studies had showed that the performance of SWM modules could be improved by varying the shapes of the spacer (Ahmad and Lau, 2006; Ranade and Kumar, 2006; Amokrane, et al., 2015b). In this work, new spacer shapes were created by making modifications to the common shapes (circular, triangular and square) to investigate the effectiveness of these new spacer designs in improving the performance of SWM modules. The new spacer designs are shown in Figure 3.5 – 3.7 for modification of circular, triangular and square shapes, respectively.

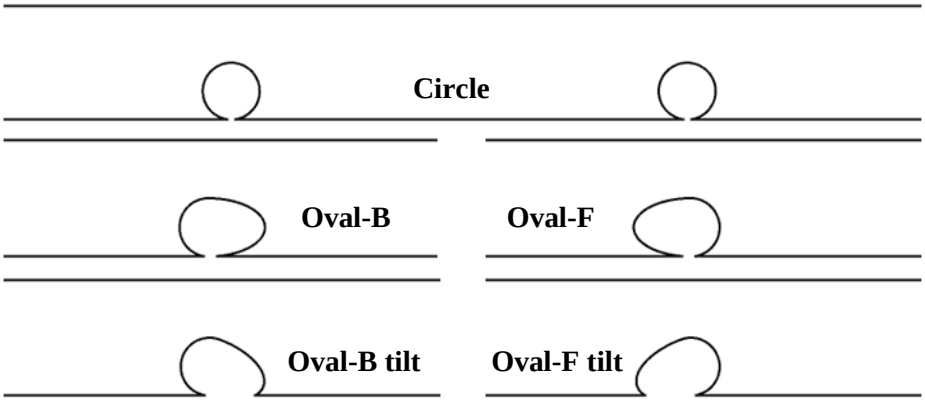

Figure 3.5: New spacer design: modification of circular shape.

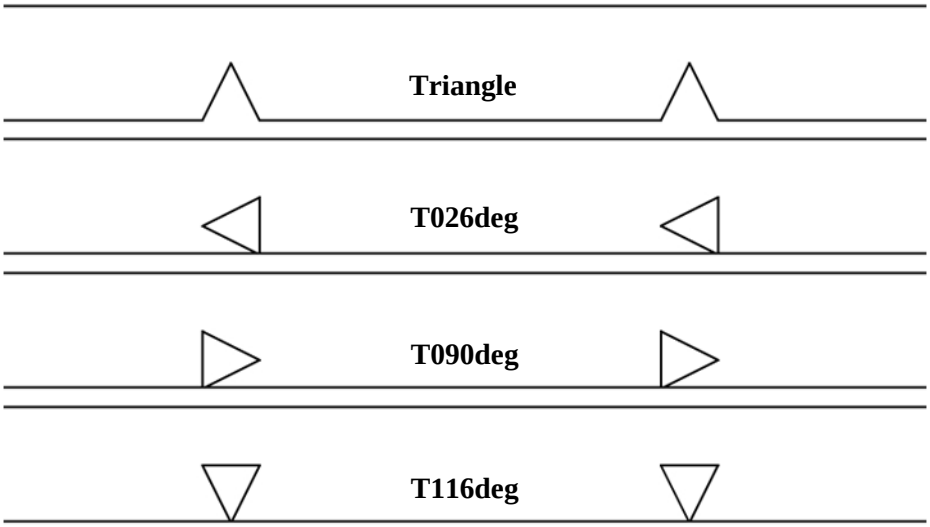

Figure 3.6: New spacer design: modification of triangular shape.

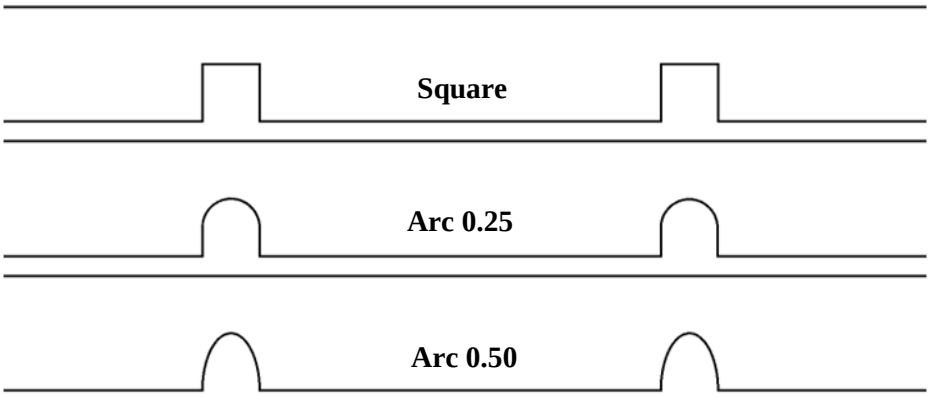

Figure 3.7: New spacer design: modification of square shape.

3.3.2 Meshing and Mesh Independence Analysis

The computational domains were meshed using ANSYS® Meshing™ application, which is a part of the analysis in ANSYS® Workbench™.

3.3.2.1 Meshing for 2D Channel Geometry

The 2D computational domain was meshed with quadrilateral cell shape (Figure 3.8), which is the most common structured grid. The grids were refined near both the membrane surfaces (top and bottom boundaries) as the velocity and concentration gradients are steeper in these regions.

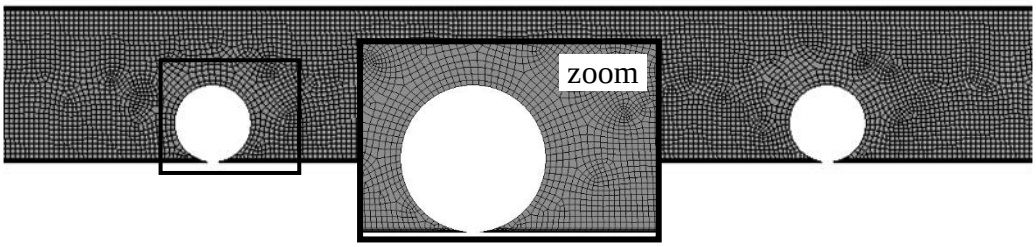

Figure 3.8: Mesh for 2D channel geometry.

Mesh independence test was performed on the computational domains to ensure that the results were independent of the mesh size. Initial simulations were carried out with finer and finer mesh size until further increase in the mesh elements did not produce significant difference in the results for the velocity, pressure drop and wall shear stress.

For 2D simulation, initial simulations were carried out with 20k, 30k, 40k, 50k and 60k mesh elements. The differences in velocity, pressure drop and wall shear stress for 60k and 50k mesh elements were less than 0.5% compared to those for 40k mesh elements (Figure 3.9). Thus, 40k mesh elements were sufficient to mesh the 2D system.

3.3.2.2 Meshing for 3D Channel Geometry

The 3D computational domain was meshed with tetrahedron and hexahedron cell shapes (Figure 3.10). The existence of spacers in the observation channel causes difficulty in creating structured grids, and thus tetrahedron cell shape was used to mesh the observation channel (Kavianipour, Ingram and Vuthaluru, 2017). On the other hand, since the inlet and outlet domains are empty (without spacers), they were meshed with hexahedron cell shape which can provide better space efficiency and convergence. The meshes were refined near both the membrane surfaces (top and bottom surface boundaries) as the velocity and concentration gradients are steeper in these regions.

For 3D simulation, initial simulations were carried out with 300k, 510k, 700k and 970k mesh elements. The differences in velocity, pressure drop and wall shear stress for 700k and 970k mesh elements were less than 1.0% compared to those for 510k mesh elements. Thus, 510k mesh elements were sufficient to mesh the 3D system (Figure 3.11).

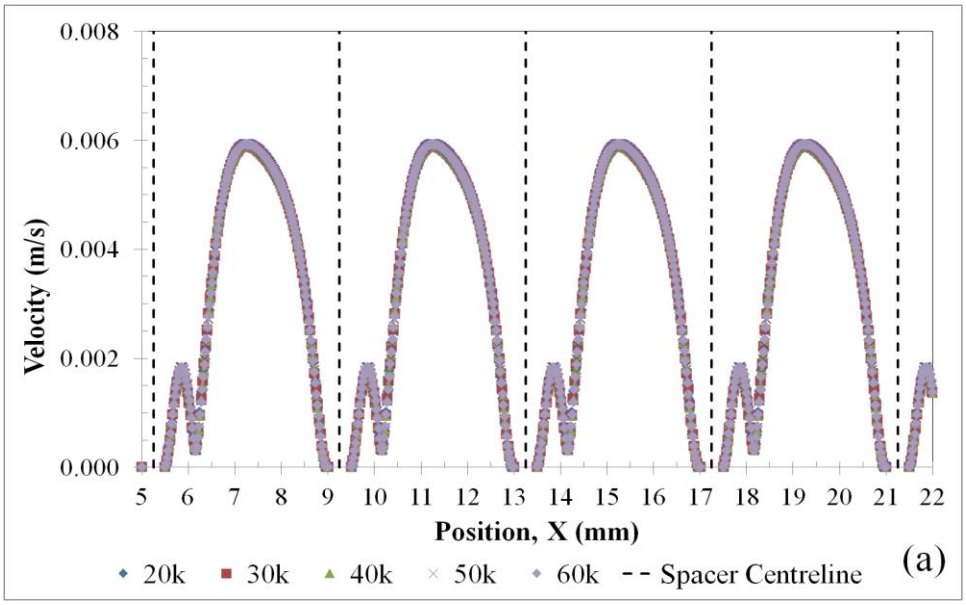

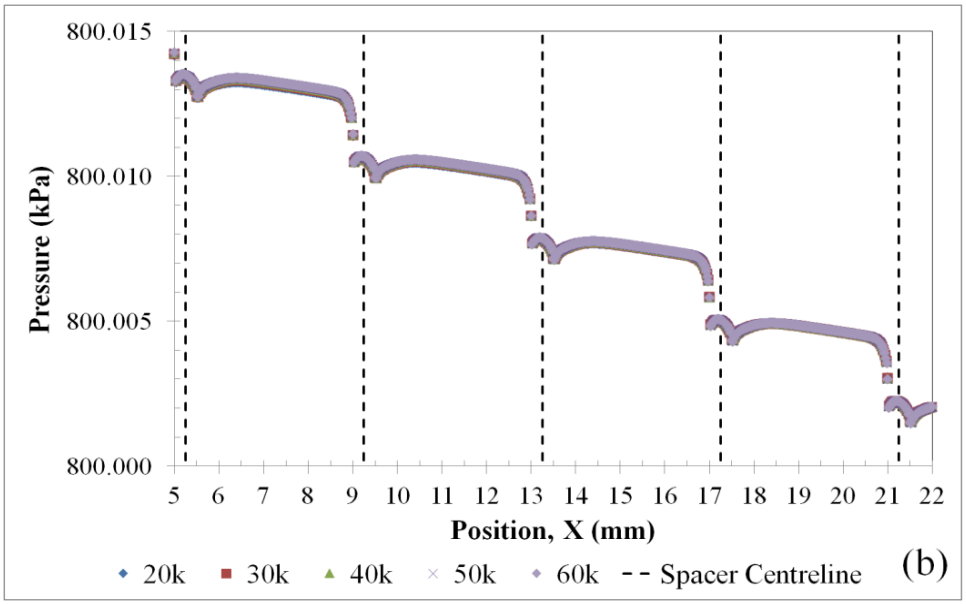

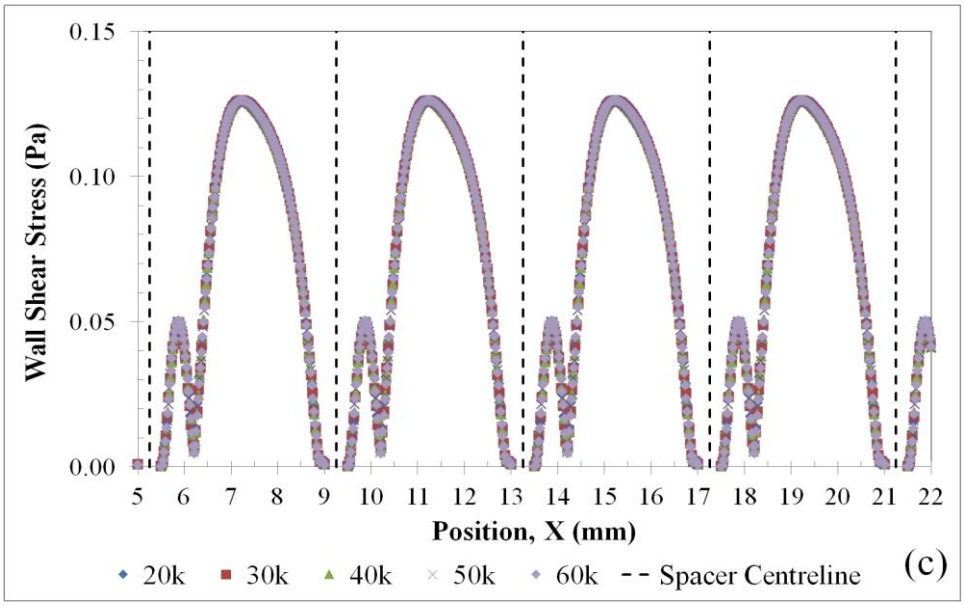

Figure 3.9: Comparison of five different mesh elements for 2D simulation for (a) velocity, (b) pressure and (c) wall shear stress at bottom membrane.

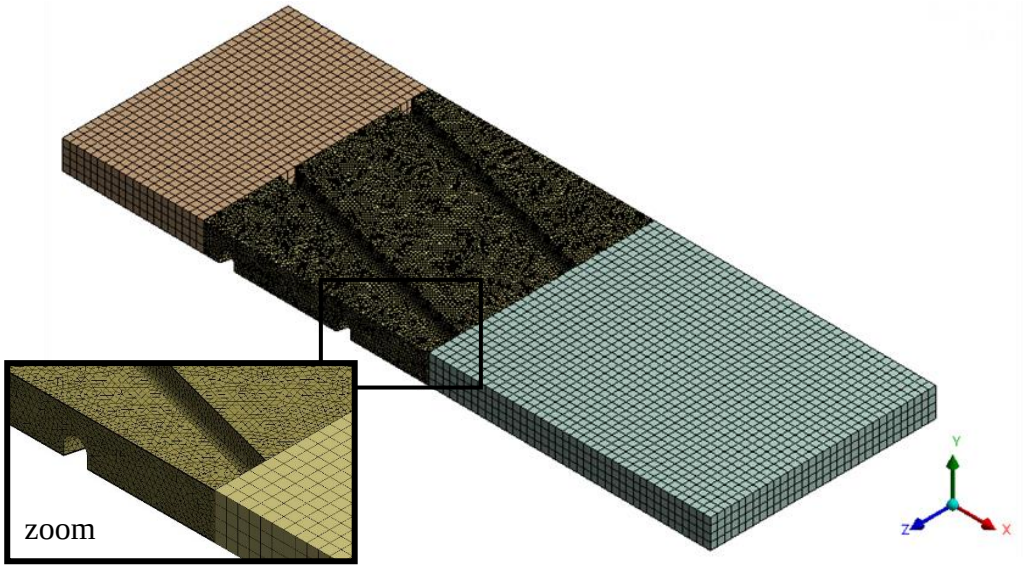

Figure 3.10: Mesh for 3D channel geometry.

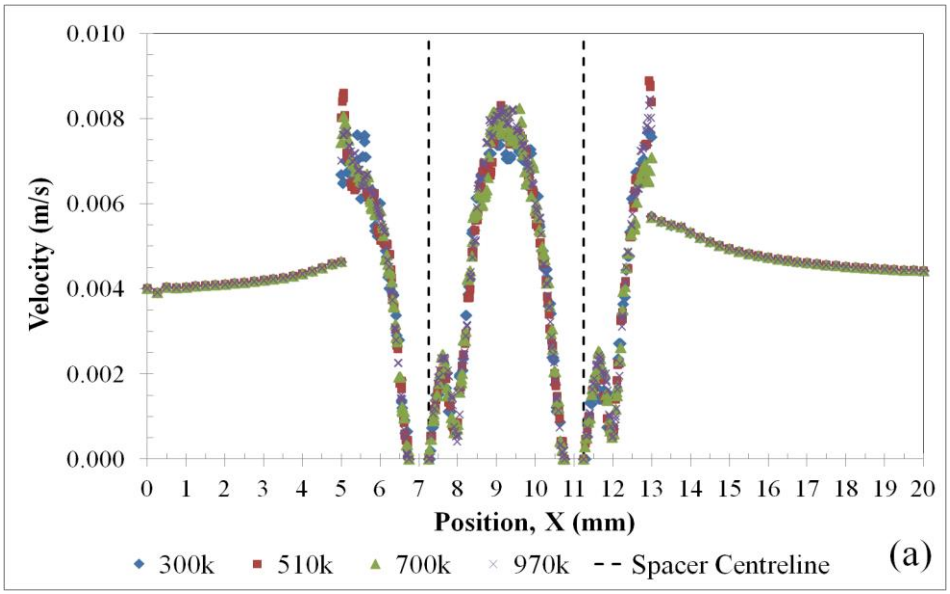

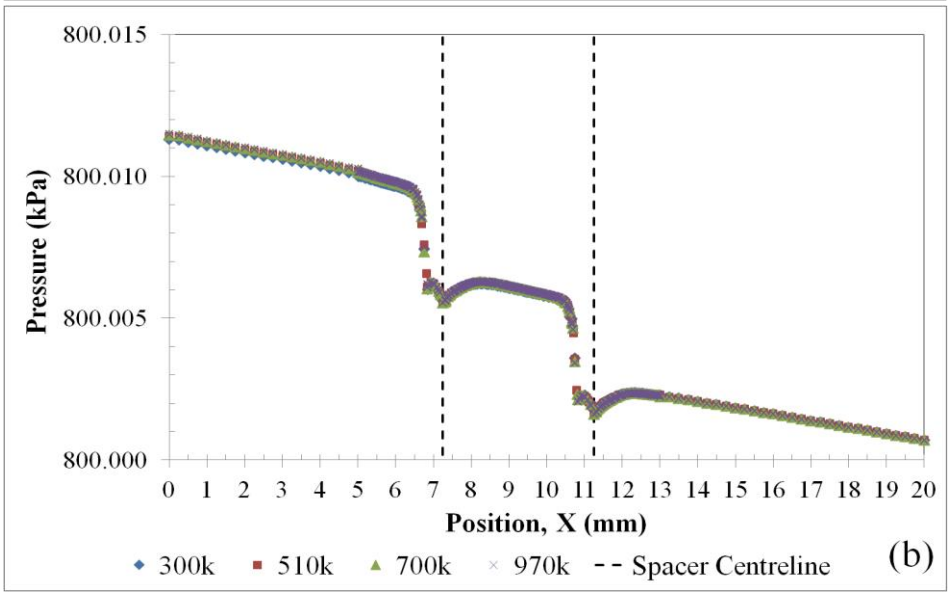

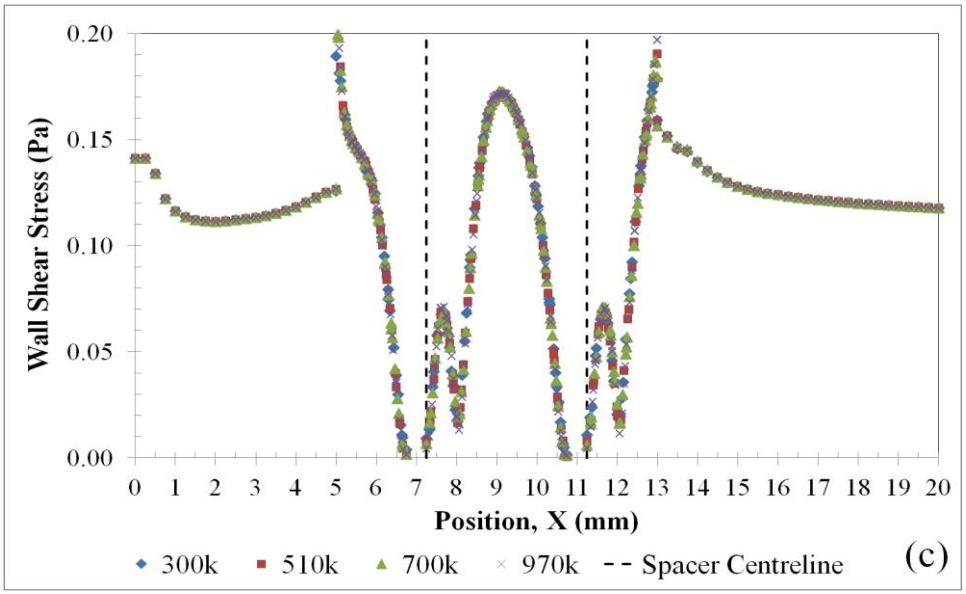

Figure 3.11: Comparison of four different mesh elements for 3D simulation for (a) velocity, (b) pressure and (c) wall shear stress at bottom membrane.

3.3.3 Solution Methods

The hydrodynamics of the fluid flow with consideration of solute concentration in a narrow membrane channel could be obtained by discretising and solving the governing equations as expressed by Eq. (3.1) – (3.3) in Section 3.2.

In the present work, ANSYS® FLUENT® 15.0 was used to simulate the fluid flow and transport phenomena in the spacer-filled narrow membrane channel. The governing equations were converted to algebraic equations that could be solved numerically using a control-volume-based technique. In a control-volume-based technique, the computational domain was divided into discrete control volume using a computational grid and the governing equations were integrated on the individual control volumes to yield algebraic equations for the discrete dependent variables, such as pressure, velocities and conserved

scalars. The algebraic equations were then linearised and solved to obtain updated values of the dependent variables.

In ANSYS® FLUENT®, the discrete values of the scalar were stored at cell centre by default. However, for convection terms, face values were required and they could be obtained via interpolations of the cell centre values. This was accomplished using Quadratic Upstream Interpolation for Convective Kinematics (QUICK) scheme, which is based on a weighted average of second-order upwind, and is most appropriate for steady flow (Lin, 2008). The QUICK scheme was also used for the discretisation of momentum equation.

The pressure and velocity were coupled and solved by Semi-Implicit Method for Pressure Linked Equation Consistent (SIMPLEC) algorithm. The SIMPLEC algorithm uses a relationship between velocity (velocity field is obtained from the momentum equations) and pressure corrections to obtain the pressure field and to enforce mass conservation (continuity equation). The simulations were benefited from using SIMPLEC algorithm because of the increased pressure-correction under-relaxation factor that could be applied, which helped in convergence speed-up. Since the governing equations were coupled and non-linear, the solution loop had to be repeated iteratively to obtain a converged numerical solution (Figure 3.12).

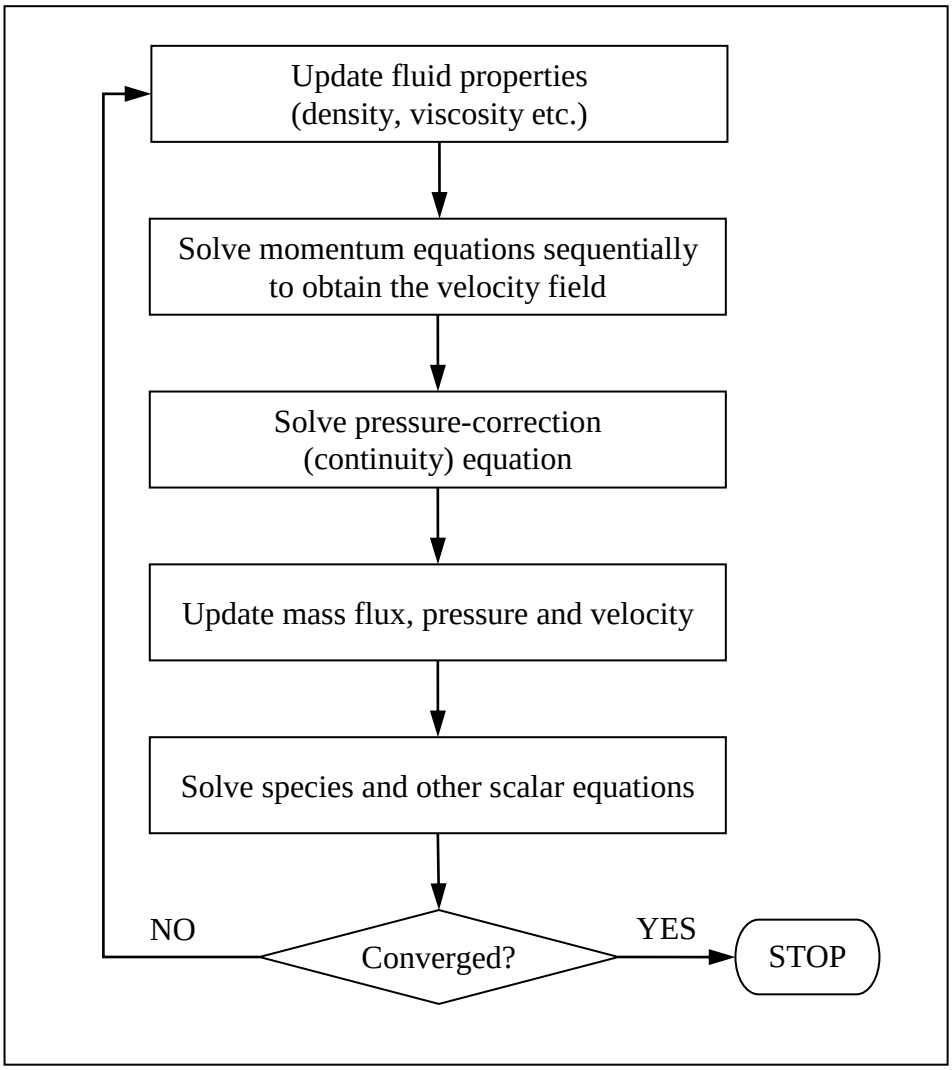

Figure 3.12: Solution loop for SIMPLEC pressure-velocity coupling algorithm (segregated solution method)

3.3.4 Simulation Assumptions and Convergence Criterion

The CFD models for fluid flow and mass transfer in this work were developed under the assumptions of isothermal and steady-state system, laminar flow and incompressible Newtonian fluid. No slip condition was fixed for the wall. The convergence criterion for the residuals of continuity, momentum and species equations was set to a value up to 10^{-6}.

3.4 Investigation on Concentration Polarisation Phenomenon

The fluid used in the simulation of concentration polarisation phenomena was NaCl aqueous solution. The physical properties of NaCl solution such as density, viscosity and diffusivity are dependent on the salt mass fraction, and are given by Geraldes, Semião and Pinho (2001) for a mass fraction not exceeding 9%:

$$\pi = 805.1\times10^{5} m_A \tag{3.4}$$

$$\rho = 997.1\times\left(1+0.696m_A\right) \tag{3.5}$$

$$\mu = 0.89\times10^{-3}\left(1+1.63m_A\right) \tag{3.6}$$

$$D_{AB} = \max\left(1.61\times10^{-9}\left(1-14m_A\right), 1.45\times10^{-9}\right) \tag{3.7}$$

where ρ is density (kg/m^3), π is osmotic pressure (Pa), μ is dynamic viscosity (Pa·s), D_{AB} is binary diffusion coefficient (m^2/s) and m_A is salt mass fraction.

The mass transfer coefficient, k is given as

$$k = \frac{D_{AB}}{\delta} \tag{3.8}$$

where δ is the developing concentration boundary layer thickness given by film theory as

$$\delta = \ln\left(\frac{m_{Aw}R}{m_{A0}-(1-R)m_{Aw}}\right)\times\frac{D_{AB}}{J_v} \tag{3.9}$$

where m_{A0} and m_{Aw} are the initial salt mass fraction and salt mass fraction at wall (membrane), respectively; R is rejection coefficient and J_v is permeation flux. Steady state conditions were reached when the diffusive back-transport of solute plus the permeate flow were equal to the convective transport of solute to the membrane.

3.4.1 Simulation Conditions

In this work, transmembrane pressure (TMP) of 800 kPa and membrane resistance, R_m of 1.56×10^{14} m^{-1} were used, which are typical values for brackish water desalination with salt mass fraction of 0.2% (Amokrane et al., 2015a). The inlet velocity into the channel was 0.02 m/s, which is a typical value for spiral-wound membrane operation and it falls into the laminar flow regime (Bucs, et al., 2015). The channel's Reynolds number introduced by Schock and Miquel (1987) was kept below 300 to enable the use of laminar flow model to simulate the flow through the computational domain (Gurreri, et al., 2016; Schwinge, Wiley and Fletcher, 2002).

The channel Reynolds number is given as

$$\mathrm{Re}_{ch} = \frac{u_{av}d_h}{\nu} \tag{3.10}$$

where ν is the kinematic viscosity, d_h is the hydraulic diameter (m) for a spacer-filled channel given as

$$d_h = \frac{4\varepsilon}{\frac{2}{h_{ch}} + (1-\varepsilon)S_{v,sp}} \tag{3.11}$$

ε is the porosity of the spacer-filled channel given as Eq. (3.12), h_{ch} is the channel height and $S_{v,sp}$ is the specific surface of the spacer given as Eq. (3.13).

$$\varepsilon = 1 - \frac{\text{spacer volume}}{\text{total volume}} \tag{3.12}$$

$$S_{v,sp} = \frac{\text{wetted surface of spacer}}{\text{volume of spacer}} \tag{3.13}$$

3.4.2 Boundary Conditions

A velocity-inlet was applied at the entrance of the simulated membrane channel, whereas a pressure-outlet was applied at the exit. The spacer surfaces were defined as wall in the simulation. The top and bottom boundaries were treated as membrane and defined as permeable walls using a user-defined function (UDF) boundary condition as described in Section 3.4.3 to model the permeation flux and concentration profile at the membrane surfaces. The boundary conditions of the computational domain were described by Eq. (3.14) – (3.17). Concentration polarisation developed due to salt accumulation on the membrane surfaces is represented by Eq. (3.16) and (3.17) (Amokrane et al., 2015a).

At inlet: $X = 0$ and $0 < Y < h_{ch}$

$$u = u_0, \quad v = 0, \quad w = 0, \quad m_A = m_{A0} \tag{3.14}$$

At outlet: $X = l_{ch}$ and $0 < Y < h_{ch}$

$$\frac{\partial u}{\partial X} = 0, \quad \frac{\partial v}{\partial X} = 0, \quad \frac{\partial w}{\partial X} = 0, \quad \frac{\partial m_A}{\partial X} = 0 \tag{3.15}$$

At bottom membrane: $Y = 0$ and $0 < X < l_{ch}$

$$u = 0, \quad v = -J_V = -\frac{1}{R_m \mu}\left(\Delta P - \Delta \pi\right), \quad w = 0,$$

$$m_A = m_{Aw} = \exp\left(\frac{J_v \delta_c}{D_{AB}}\right) \frac{m_{Ac}}{R + (1-R)\exp\left(\frac{J_v \delta_c}{D_{AB}}\right)} \tag{3.16}$$

At top membrane: $Y = h_{ch}$ and $0 < X < l_{ch}$

$$u = 0, \quad v = J_V = \frac{1}{R_m \mu}\left(\Delta P - \Delta \pi\right), \quad w = 0,$$

$$m_A = m_{Aw} = \exp\left(\frac{J_v \delta_c}{D_{AB}}\right) \frac{m_{Ac}}{R + (1-R)\exp\left(\frac{J_v \delta_c}{D_{AB}}\right)} \tag{3.17}$$

where u, v and w represent the velocity components in X-, Y-, and Z-direction, respectively; h_{ch} and l_{ch} are the channel height and length, respectively; m_{Aw} and m_{Ac} are the salt mass fraction at wall (membrane) and adjacent to wall, respectively; J_v is the permeation flux, R_m is the membrane resistance, δ_c is the distance between membrane wall and adjacent cell, and R is the rejection coefficient.

3.4.3 User-Defined Function (UDF) for Permeable Membrane

In general, a user-defined function (UDF) is a function written in C programming language that can be loaded into ANSYS® FLUENT® solver to enhance its standard features such as customise boundary conditions and define material properties. The UDFs must be compiled and loaded into the solver library before it can be used. The UDFs will then access the solver data, perform the necessary calculations and update the solver data repeatedly for every iteration.

In the current simulation works, as water permeated through the membrane, the concentration of NaCl in the feed solution, especially next to the membrane, would increase. Consequently, the density, viscosity and diffusivity of NaCl aqueous solution would also change as these physical properties were a function of the salt mass fraction as defined in Eq. (3.5) – (3.7). To take into account of these changes, UDF for these properties were integrated into the solver solution. The "DEFINE_PROPERTY" and "DEFINE_DIFFUSIVITY" macros were utilised together with Data Access macro in the UDFs to extract the salt mass fraction value from the solver for calculations and then return the updated values of density, viscosity and diffusivity to the solver for every iteration.

The permeate flux J_v through the membrane is related to the osmotic pressure $\Delta\pi$, which was calculated by Eq. (3.4) accounting for concentration polarisation effect on the membrane. In order to model a salt mass fraction profile rather than applying a constant mass fraction value on the membrane surface,

UDF was written for the permeate flux J_v and the salt mass fraction adjacent to wall m_{Aw} based on Eq. (3.16) – (3.17), and integrated into the solution of the governing equations. The film theory, which relates the permeation properties with the channel hydrodynamics, was incorporated in the UDF using "DEFINE_PROFILE" macro together with Adjacent Cell Index macro. The "DEFINE_PROFILE" macro was used to define the salt mass fraction profile that varies as a function of spatial coordinate at the membrane boundaries. The Adjacent Cell Index macro would extract the hydrodynamics changes next to the membrane from the solver for calculations by the UDF and predicted the new membrane wall mass fraction. It then updated the solver data with the new value and the iterations continue until the convergence criteria were met (Figure 3.13).

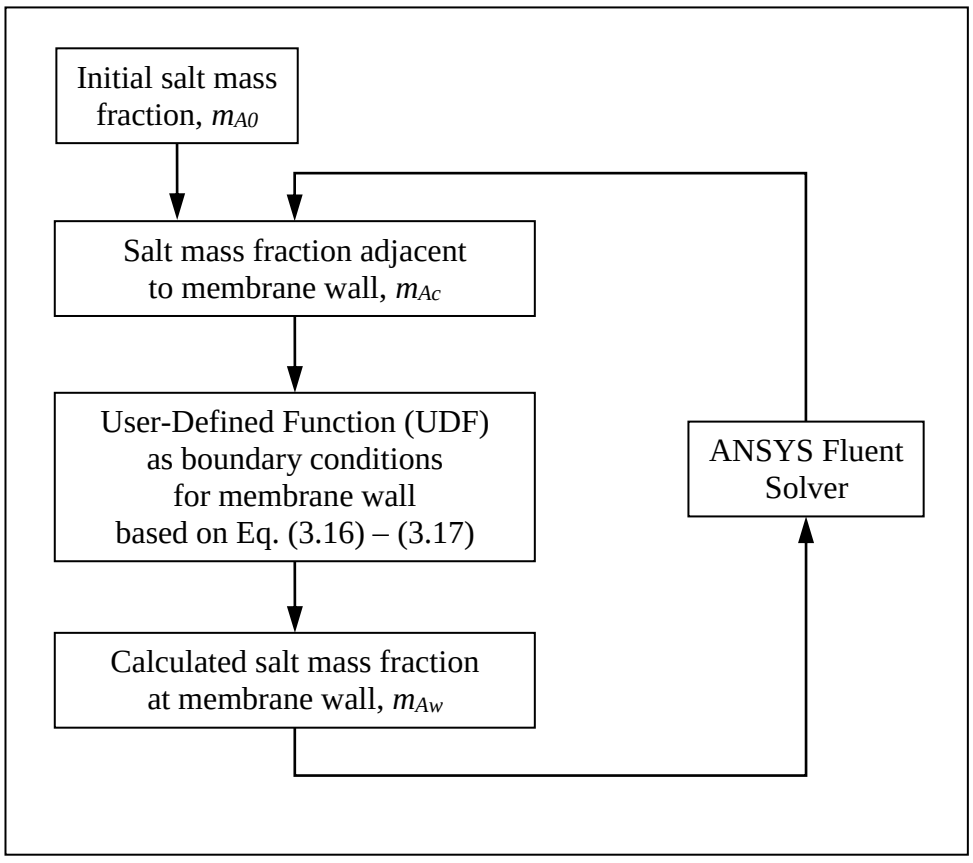

Figure 3.13: Iteration loop for UDF membrane boundary condition.

3.4.4 Validation of Simulation Results

In order to provide sufficient confidence in the current simulation works, the developed simulation model was compared against the results reported by Ahmad, Lau and Abu Bakar (2005) with the same boundary conditions and assumptions, and the difference in results was less than 3%. Figure 3.14 shows the comparison of both works on the profiles of concentration factor across the empty membrane channel for different Reynolds number. The study by Amokrane (2015a) was also validated against the work by Ahmad, Lau and Abu Bakar (2005), and the comparisons were also in very good agreement.

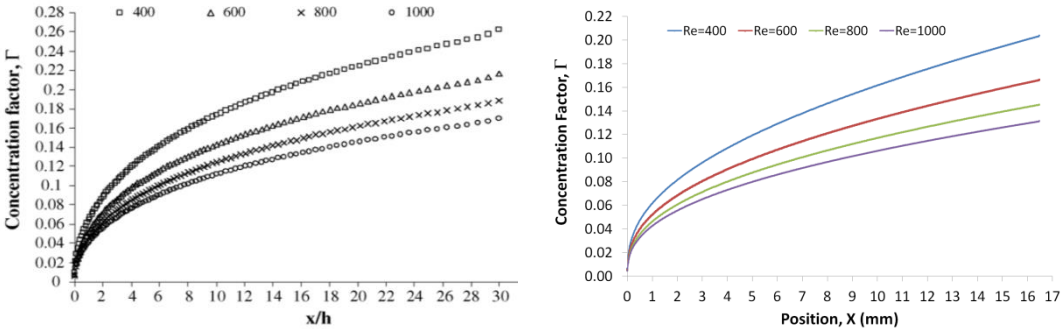

(a) (b)

Figure 3.14: Profiles of concentration factor, Γ across empty membrane channel for different Reynolds number. (a) Work by Ahmad, Lau and Abu Bakar (2005) and (b) current work.

3.5 Investigation on Particle Deposition (Fouling) on Membrane

3.5.1 Discrete Phase Model (DPM)

In order to simulate the condition of particle deposition (fouling) on the membrane surfaces, the flow field and particle transport in the membrane channel

with permeable membranes were determined by enabling the discrete phase model (DPM) in ANSYS® FLUENT®.

The discrete phase model used in this simulation work followed the Euler-Lagrange approach. The system consisted of two phases, i.e. the fluid phase and the dispersed phase. The fluid phase was taken to be continuous by solving the Navier-Stokes equations, and the dispersed phase was calculated by tracking the particles through the flow field. Particle size of 1 μm and particle density of 1210 kg/m^3 was used in the simulation as suggested by Li, et al. (2012). The volume fraction of particles was ensure to be less than 10% so that the existence of a dispersed phase in the fluid phase will not noticeably affect the fluid physical properties (Li, et al., 2006).

The motion or trajectory of the particles was calculated by integrating the force balance on the particles (ANSYS® FLUENT® Theory Guide, 2016). This force balance, which equates the particle inertia with the forces acting on the particle, is given as

$$\frac{du_p}{dt} = F_D\left(u - u_p\right) + F_G + F_V + F_P + F_L \tag{3.18}$$

where u is the fluid velocity, u_p is the particle velocity, F_D $(u - u_p)$ is the drag force, F_G is the gravitational force, F_V is the virtual mass force (force required to accelerate the fluid surrounding the particle), F_P is the pressure gradient force (force arises due to the pressure gradient in the fluid) and F_L is the Saffman's lift force. As recommended by ANSYS® FLUENT® Theory Guide (2016), when the

fluid density is comparable to the particle density (density ratio between the two is larger than 0.1), the virtual mass force and pressure gradient force become important and they are recommended to be included in the simulation.

The forces above are based on per unit particle mass defined by the following equations (ANSYS® FLUENT® Theory Guide, 2016):

$$F_D = \frac{18\mu}{\rho_p d_p{}^2} \frac{C_D Re}{24} \tag{3.19}$$

$$F_G = \frac{g(\rho_p - \rho)}{\rho_p} \tag{3.20}$$

$$F_V = C_{vm} \frac{\rho}{\rho_p} \left(u_p \nabla u - \frac{du_p}{dt} \right) \tag{3.21}$$

$$F_P = \frac{\rho}{\rho_p} u_p \nabla u \tag{3.22}$$

$$F_L = \frac{5.2\nu^{0.5} \rho d_{ij}}{\rho_p d_p (d_{lk} d_{kl})^{0.25}} (u - u_p) \tag{3.23}$$

where μ is the molecular viscosity of the fluid, ν is the kinematic viscosity, ρ is the fluid density, ρ_p is the particle density, d_p is the particle diameter, Re is the relative Reynolds number defined as $Re \equiv \rho d_p |u_p - u| / \mu$, g is the gravitational

acceleration, C_D is the drag coefficient, C_{vm} is the virtual mass factor and d_{ij} is the deformation tensor.

3.5.2 Boundary Conditions

A velocity-inlet was applied at the entrance of the simulated membrane channel and the particles were injected into the computational domain from the inlet surface. A pressure-outlet was applied at the exit and the fate of the particle trajectory at this boundary is "escape", where the particle was removed from the calculation when it encountered the boundary. The spacer surfaces were defined as wall in the simulation. The top and bottom surface boundaries were treated as permeable membranes and a particle would be trapped when it came into contact with the membranes so as to simulate the condition of fouling.

3.5.3 Solution Procedures

The solution procedures for particle deposition analysis on membrane surfaces to investigate the condition of fouling were summarised in Figure 3.15.

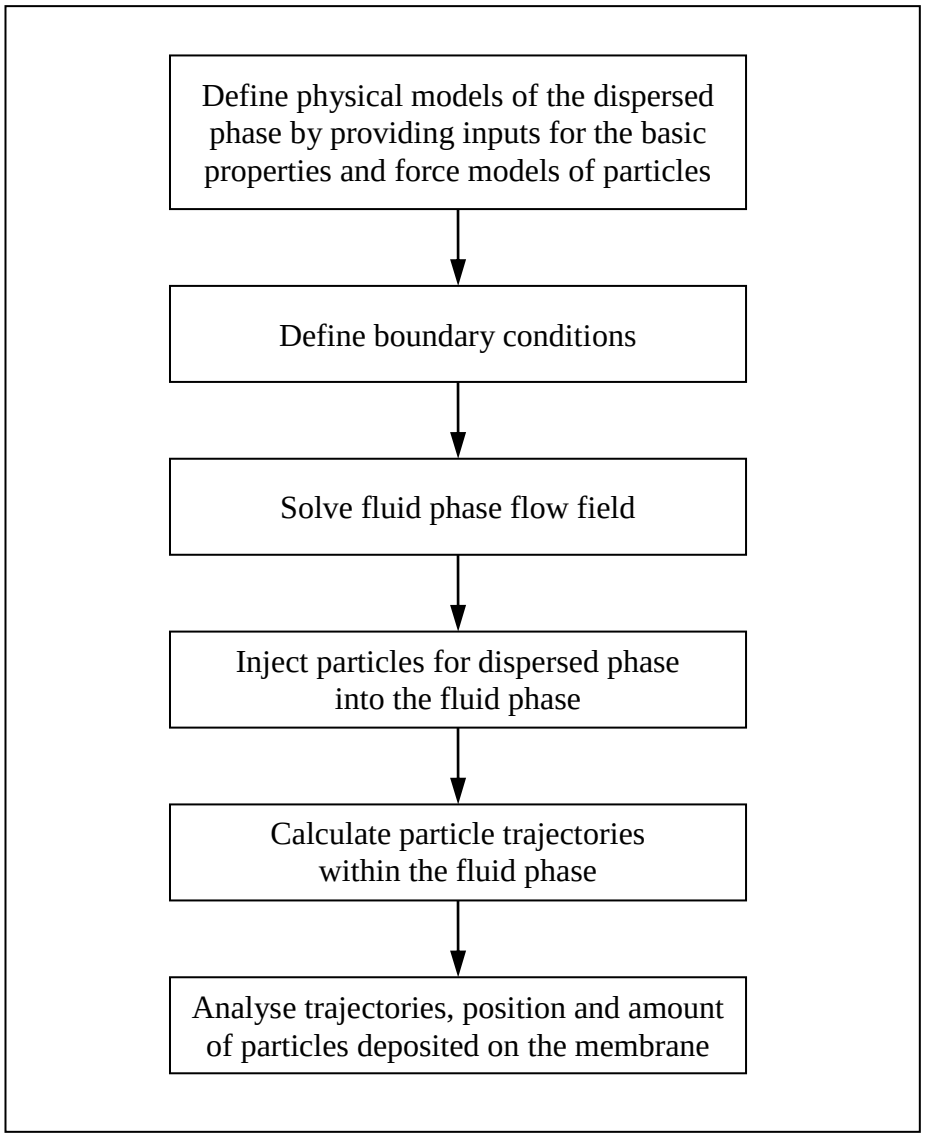

Figure 3.15: Solution procedures for particle deposition analysis (discrete phase model).

3.6 Dimensionless Factors and Ratios

A normalisation procedure was employed throughout this work to obtain dimensionless results that were used to better compare the simulation results for different spacer shapes and geometries with the same characteristics. The dimensionless concentration factor, Γ, which represents the extend of concentration polarisation, is given as

$$\Gamma = \frac{m_{Aw} - m_{A0}}{m_{A0}} \tag{3.24}$$

where m_{Aw} is the salt mass fraction at wall (membrane) and m_{A0} is the initial salt mass fraction.

The physical parameters for mass transport in a spacer-filled channel are the dimensionless numbers Schmidt number, *Sc* and Sherwood number, *Sh*. Schmidt number is the ratio of the rate of viscous diffusion (momentum diffusivity) to the rate of mass diffusion (mass diffusivity) whereas Sherwood number is the ratio of the rate of convective mass transfer to the rate of diffusive mass transfer and can be defined as a function of the Reynolds and Schmidt numbers.

$$Sc = \frac{\nu}{D_{AB}} = \frac{\mu}{\rho D_{AB}} \tag{3.25}$$

$$Sh = \frac{k}{D_{AB}/d_s} = aRe^m Sc^n \tag{3.26}$$

where ν is the kinematic viscosity, d_s is the spacer filament diameter and *a*, *m* and *n* are correlation coefficients.

Power number, *Pn*, as defined by Li, et al. (2004), represents the cross-flow power consumption in a membrane channel, and can be used to compare the energy consumption with different spacer shapes and geometries. The power

number was calculated using pressure drop results, ΔP obtained from simulations and Eq. (3.27) and (3.28). The dimensionless power number is defined as the ratio of the power number in a membrane channel with a specific type of spacer to the maximum value of all the systems under consideration.

$$Pn = SPC \frac{\rho^2 h_{ch}^4}{\mu^3} \tag{3.27}$$

where *SPC* is the specific power consumption given as

$$SPC = \frac{u_{av} \Delta P}{l_{ch}} \tag{3.28}$$

The condition of fouling on a membrane surface was investigated by analysing the amount of particles deposited (trapped) on the membrane surface. The fouling tendency or behaviour of the particles was described using a particle deposition ratio, defined as the amount of particle deposited on the membrane over the total amount of particle injected into the domain.

3.7 Experimental Setup

The schematic diagram for the experimental work and the actual experimental setup are shown in Figure 3.16 and Figure 3.17, respectively. The experimental setup in general composed of a feed tank, a mechanical diaphragm metering pump (OBL Simplex, Model: MD101PPM1153) that has a maximum

working pressure of 10 bar, a pump dampener (BLACOH SENTRY) that was used to control and stabilise pressure fluctuation in the system, a custom-fabricated membrane testing cell, a digital pressure indicator (Autonics, PSAN Series), a flow meter (Dwyer, RMB-SSV), a pressure differential meter (WIKA, Model: DPGS40) and a data recorder (Simex, SRD-99) or collectively referred to as pressure drop meter in this work, piping and ball valves. This experimental setup was based on the typical setup used to study fluid flow across a membrane channel by other researchers (Ahmad and Lau, 2007; Karabelas, Kostoglou and Koutsou, 2015).

3.7.1 Membrane Testing Cell

The membrane testing cell, custom-fabricated by Affplus Engineering & Trading, consists of two detachable plates as shown in Figure 3.18. Membrane and spacers were placed in a channel on the bottom plate, and the top plate was then covered on top, sealed with an O-ring. The two plates were tightened together with twelve bolts and nuts. The testing cell has four connections, one for inlet, one for outlet, and two for pressure drop meter connections (Figure 3.19). The permeate was collected through the holes in the middle of the channel.

The testing cell was made from polymethyl methacrylate (PMMA), or commonly known as acrylic. The transparency property of this material was useful as it allowed the conditions in the channel to be monitored during the experiment. The testing cell is 340 mm long, 140 mm wide and 70 mm thick while the membrane channel is 280 mm long, 40 mm wide and 13 mm deep with a permeation area of 92 mm × 22 mm.

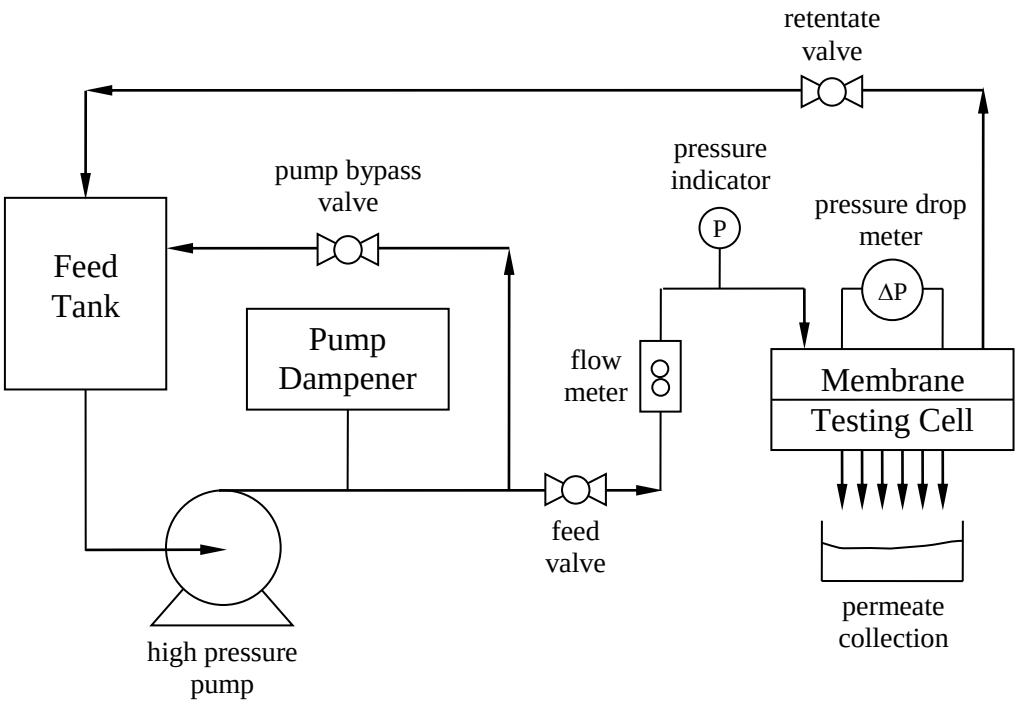

Figure 3.16: Schematic representation of the experimental work.

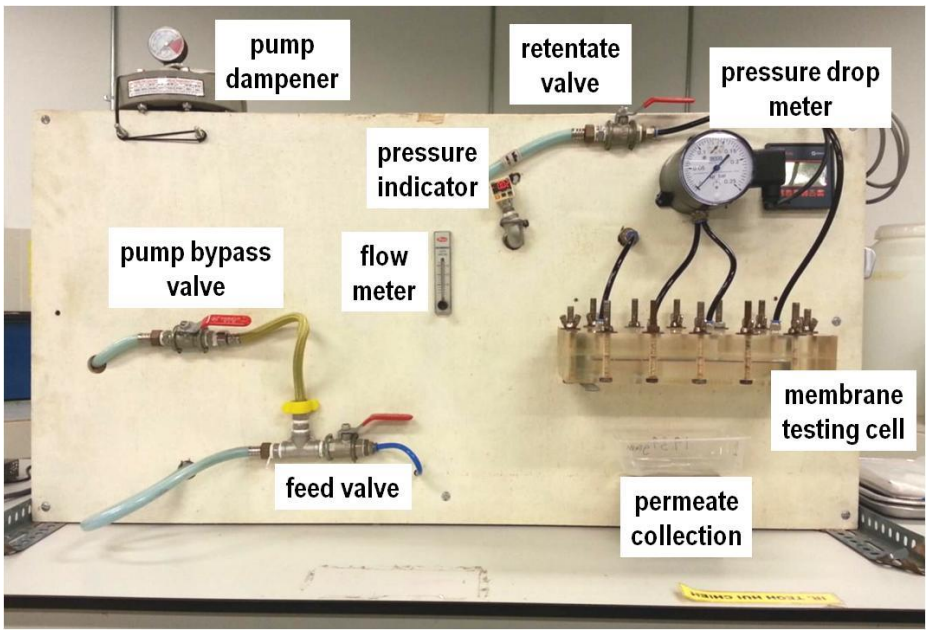

(a)

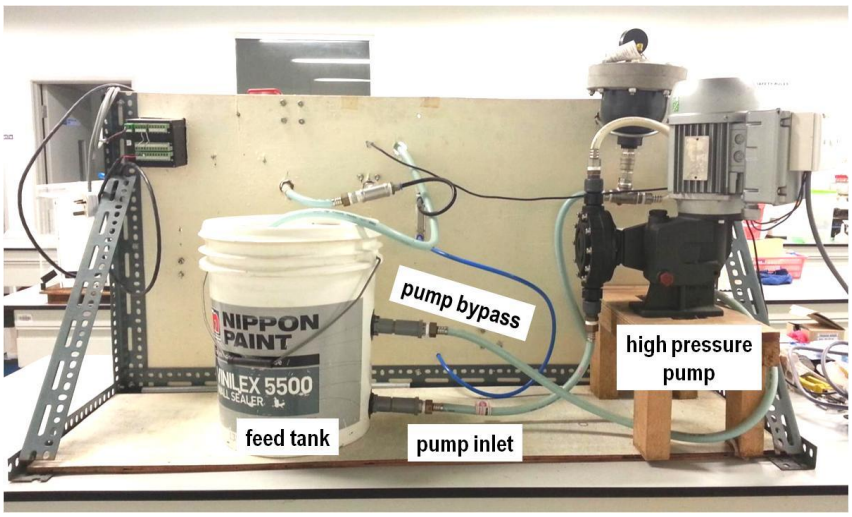

(b)

Figure 3.17: Actual experimental setup. (a) front and (b) back.

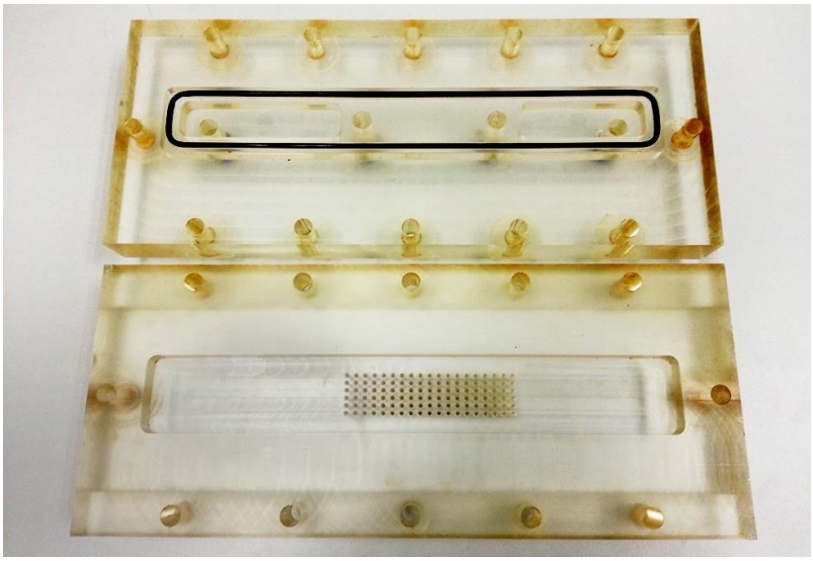

Figure 3.18: Membrane testing cell showing the two detachable plates and an O-ring on the top plate.

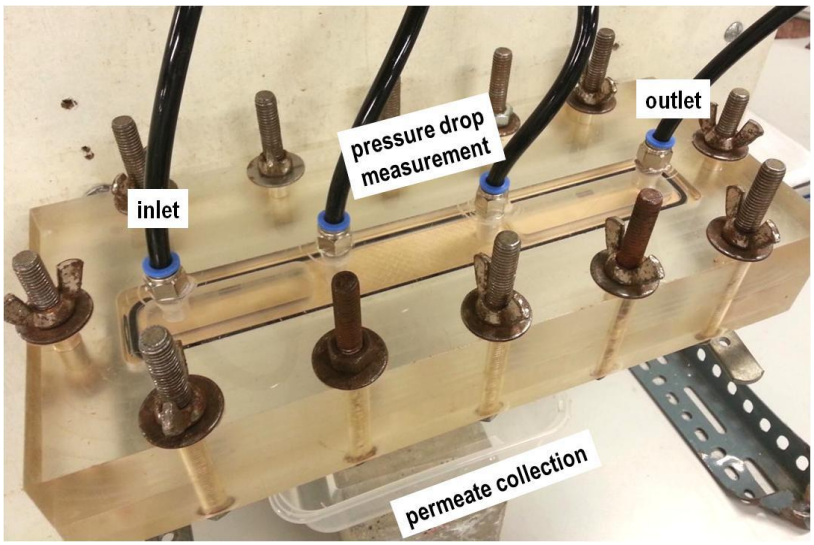

Figure 3.19: Connections at the membrane testing cell.

3.7.2 Experimental Materials

A commercial spiral wound reverse osmosis element with polyamide thin-film composite membrane (DOW FILMTEC™ BW60-1812-75) purchased from Crystal Water Enterprise Sdn. Bhd. was used in the experimental work (Figure 3.20). This membrane had a resistance, R_m in the order of 10^{14} m^{-1}. The membrane was cut to the size that fitted the channel of the testing cell and was replaced with a new piece after each experiment.

Figure 3.20: DOW FILMTEC™ spiral wound reverse osmosis element.

The spacers (Figure 3.21) were obtained from Delstar Technologies, Inc. The distance between the spacers filaments is approximately 4 mm and the diameter of the filament is 0.5 mm. The spacers were arranged in cavity configuration with a flow attack angle of 90°.

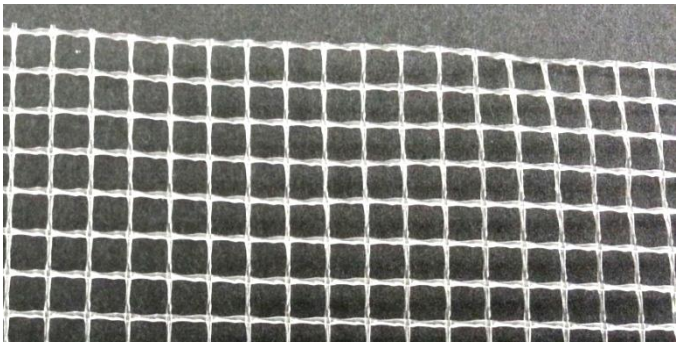

Figure 3.21: Spacers.

3.7.3 Experimental Procedures

The experiment was conducted to validate the simulation results as a mean to provide confidence in the simulation works. The experiments were run for four different flow rates, i.e. 2.5, 5.0, 7.5 and 10.0 GPH which correspond to Reynolds number of 105, 211, 316 and 422, to obtain the relationships between Reynolds number and pressure drop, and between Reynolds number and permeate flux. The feed to the system was NaCl solution with a mass fraction of 0.2% and the transmembrane pressure was maintained at 8 ± 0.5 bar.

The first pressure drop data was only collected after the system had run for at least five minutes to ensure that the system stabilised before the data was gathered. The pressure drop data were taken every five minutes for 30 minutes, the volume of permeate collected over 30 minutes was recorded, and the same experiment was repeated three times. The average values from these three sets of data were used to validate the simulation results.

The permeate flux, J_v was calculated using Eq. (3.29)

$$J_v = \frac{V}{A} \tag{3.29}$$

where V (volumetric flow rate, m^3/min) is the volume of permeate collected over 30 minutes and A is the permeation area, m^2.

CHAPTER 4

RESULTS AND DISCUSSION

4.1 Introduction

The results from the 2D and 3D CFD simulations are presented and discussed in this chapter. Analysis of the effects of Reynolds number, spacer geometries and flow attack angles on velocity, wall shear stress, pressure drop (power number), concentration polarisation and particle deposition on membrane surfaces are provided. The results are presented in the forms of contours, streamlines, line charts and bar charts to illustrate the effects of spacer geometries and flow attack angles on membrane performance.

4.2 2D Simulations

4.2.1 Effect of Spacers on Membrane Performance

This study investigated the effect of spacers (empty channel, cavity configuration and zig-zag configuration) in a membrane channel on concentration polarisation and pressure drop. Figure 4.1 shows the profiles of concentration factor on the top and bottom membranes across the channel for different circle spacer configurations.

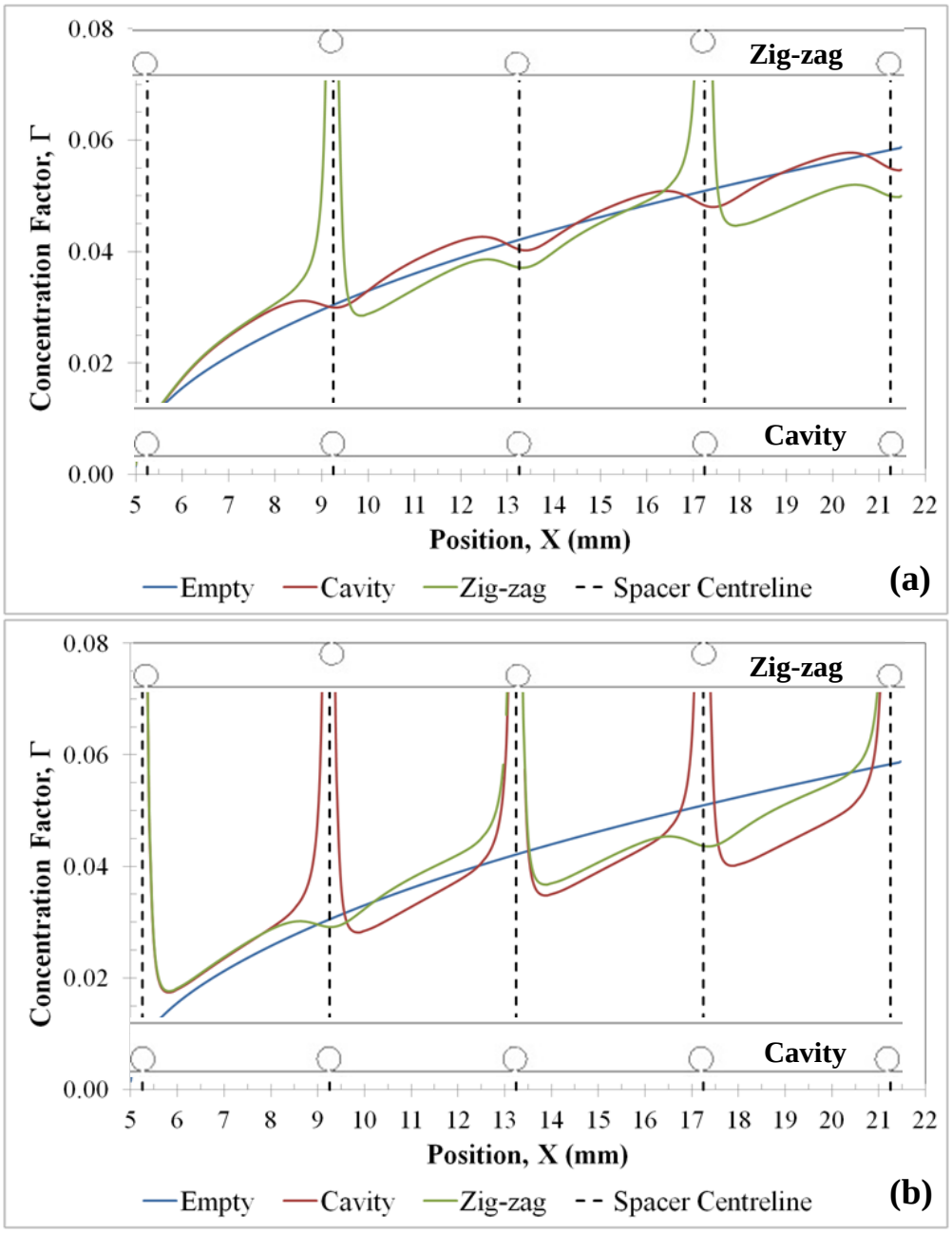

Figure 4.1: Profiles of concentration factor, Γ on (a) top and (b) bottom membranes across channel length for empty channel, cavity and zig-zag configurations.

At the top membrane, the concentration factor for zig-zag configuration is lower than cavity configuration due to the existence of spacers. It can be seen that the concentration factor dropped as the flow passed through the spacers. The opposite is true at the bottom membrane where the concentration factor for cavity configuration is lower than zig-zag configuration, again due to the existence of

(more) spacers at the bottom membrane for cavity configuration. Figure 4.1 also show that the reduction of concentration factor is higher further down the channel. All these results concluded that the existence of spacers can help to reduce concentration polarisation phenomenon on the membrane.

Table 4.1 summarised the average mass transfer coefficient across the channel length for the three different spacer configurations. Comparing the cavity and zig-zag configurations, the mass transfer coefficient results agreed with the concentration factor results where lower concentration factor would give higher mass transfer. The mass transfer coefficient for empty channel was higher compared to either two of the other configurations due to the lower concentration factor between the first and second spacer, causing the average mass transfer coefficient to be slightly higher. However, further down the channel after subsequent spacers, it can be observed in Figure 4.1 that the concentration factor for empty channel increased drastically, thus giving a lower mass transfer coefficient compared to the other two configurations.

Although the results proved that the existence of spacers is able to increase mass transfer, it does come with a cost. Spacers in a channel pose obstacle to the flow and result in higher pressure drop across the channel. In general, pressure drop across a spacer-filled channel is attributed to form drag, viscous drag on walls (spacer walls and membrane surfaces) and directional flow changes. During a membrane separation process, although pressure drop along the channel is inevitable, higher pressure drop causes the necessity to pump the feed at higher pressure to compensate the pressure loss in order to maintain the desired product specifications. Subsequently, this will result in higher power

consumption (represented by dimensionless power number in Figure 4.2) and higher operating cost.

Table 4.1: Average mass transfer coefficient, *k* across channel length for empty channel, cavity and zig-zag configurations.

Configuration	Average Mass Transfer Coefficient, *k* (m/s) 10^{-4}	
	Top	**Bottom**
Empty	1.3305	1.3256
Cavity	1.2630	1.3639
Zig-zag	1.3211	1.3095

An analysis by Da Costa, Fane and Wiley (1994) on the processing costs in spacer-filled channels demonstrated that there were possibilities to optimise the spacers in order to reduce energy losses. In spite of the fact that pressure drop in a channel cannot be eliminated, its extent can be minimised. One of the ways is by altering the flow pattern in a channel through the modification of the geometrical characteristics of spacers in the channel. Amokrane, et al. (2015a) also noted that the increase in mass transfer coefficient values is associated with the undesirable increase in pressure drop and these two factors can be balanced through the selection of appropriate spacer design. In view of these results, the new spacer designs investigated in the subsequent sections aimed to address this issue.

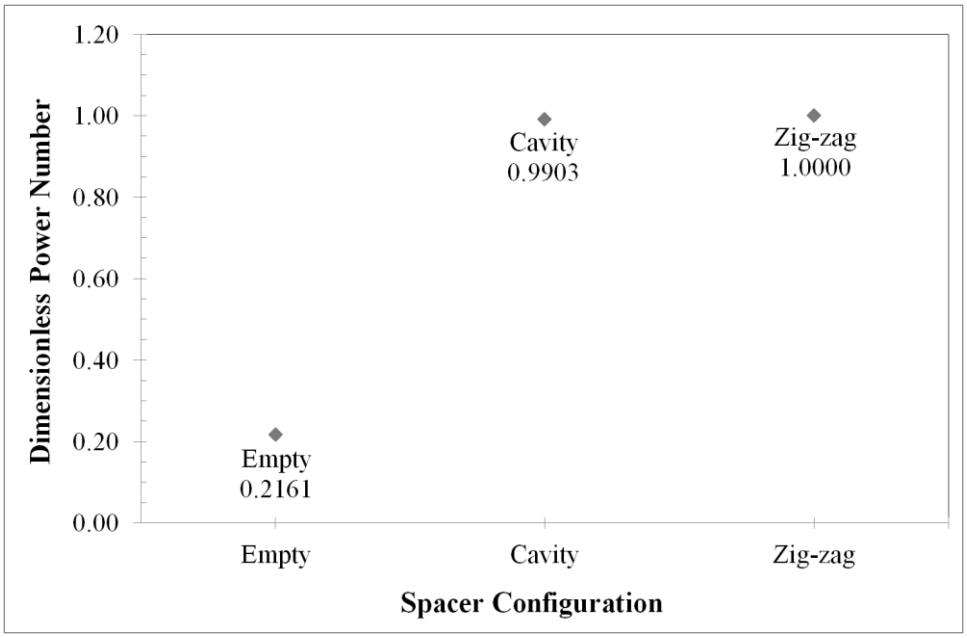

Figure 4.2: Dimensionless power number across channel length for empty channel, cavity and zig-zag configurations.

4.2.2 Effect of Reynolds Number on Membrane Performance

This study investigated the effect of feed Reynolds number (from 34 to 172) in a cavity configuration membrane channel with circle spacer on membrane performance such as the tendency for concentration polarisation and particle deposition to occur, pressure drop and mass transfer coefficient. The simulation results from this study were validated against the experimental results so as to provide confidence to the CFD models used in this work.

Figure 4.3 depicts the profiles of concentration factor on the top and bottom membranes across the channel length for different Reynolds number. The results in Figure 4.3 – 4.5 indicated that concentration polarisation phenomenon could be reduced and mass transfer could be increased by increasing the Reynolds number. This result was found to be in agreement with the findings of Ahmad, et al. (2005). The average concentration factor (calculated between the

first and the last spacers) at the bottom membrane was lower compared to the top (Figure 4.4). This finding again proved that spacers could help to reduce the effect of concentration polarisation.

Figure 4.6 shows the distance travelled by the particles injected at different channel height before depositing on the membrane surfaces. For example in Figure 4.6 (a), for particles injected at position Y = 0.95 mm, the particles travelled a distance of 6.88, 8.74, 10.7, 12.6 and 14.4 mm before depositing on the top membrane for *Re* of 34, 69, 103, 138 and 172, respectively. This finding suggested that higher *Re* allows particles to travel further before deposition, meaning that higher *Re* can aid in reducing fouling on membrane surfaces. Figure 4.6 (b) shows the particle deposition condition on the bottom membrane. The spacers at the bottom membrane helped to reduce the amount of particle deposited as *Re* increases.

From these results, it can be inferred that accelerated flow can serve as a factor to mitigate fouling phenomenon, as particle is exposed to greater shear-induced lift force arising from higher velocity magnitude. The particle will be lifted off and away from the membrane, reducing the likelihood of particle deposition on the membrane surfaces.

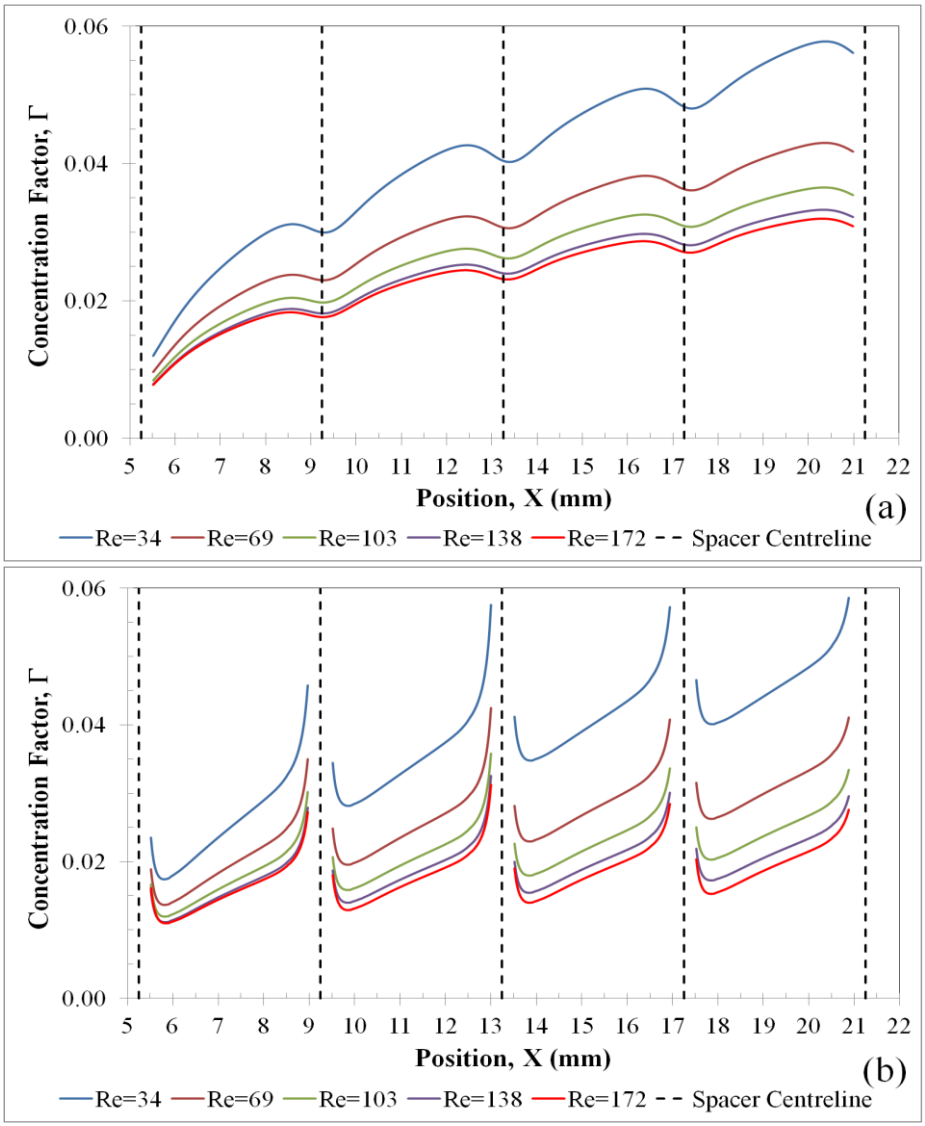

Figure 4.3: Profiles of concentration factor, Γ on (a) top and (b) bottom membranes across channel length for different *Re*.

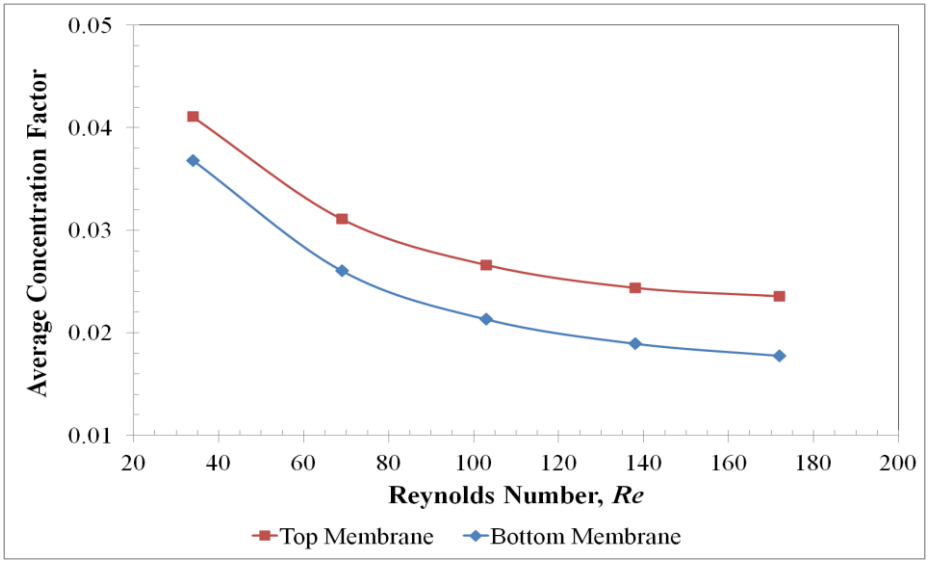

Figure 4.4: Average concentration factor, Γ_{avg} on top and bottom membranes between the first and last spacers as a function of *Re*.

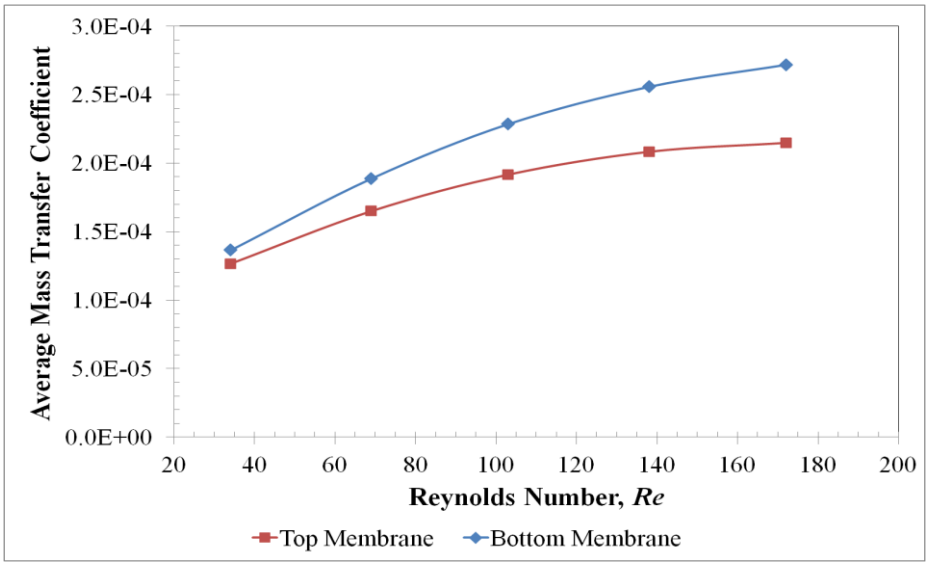

Figure 4.5: Average mass transfer coefficient, k_{avg} on top and bottom membranes between the first and last spacers as a function of *Re*.

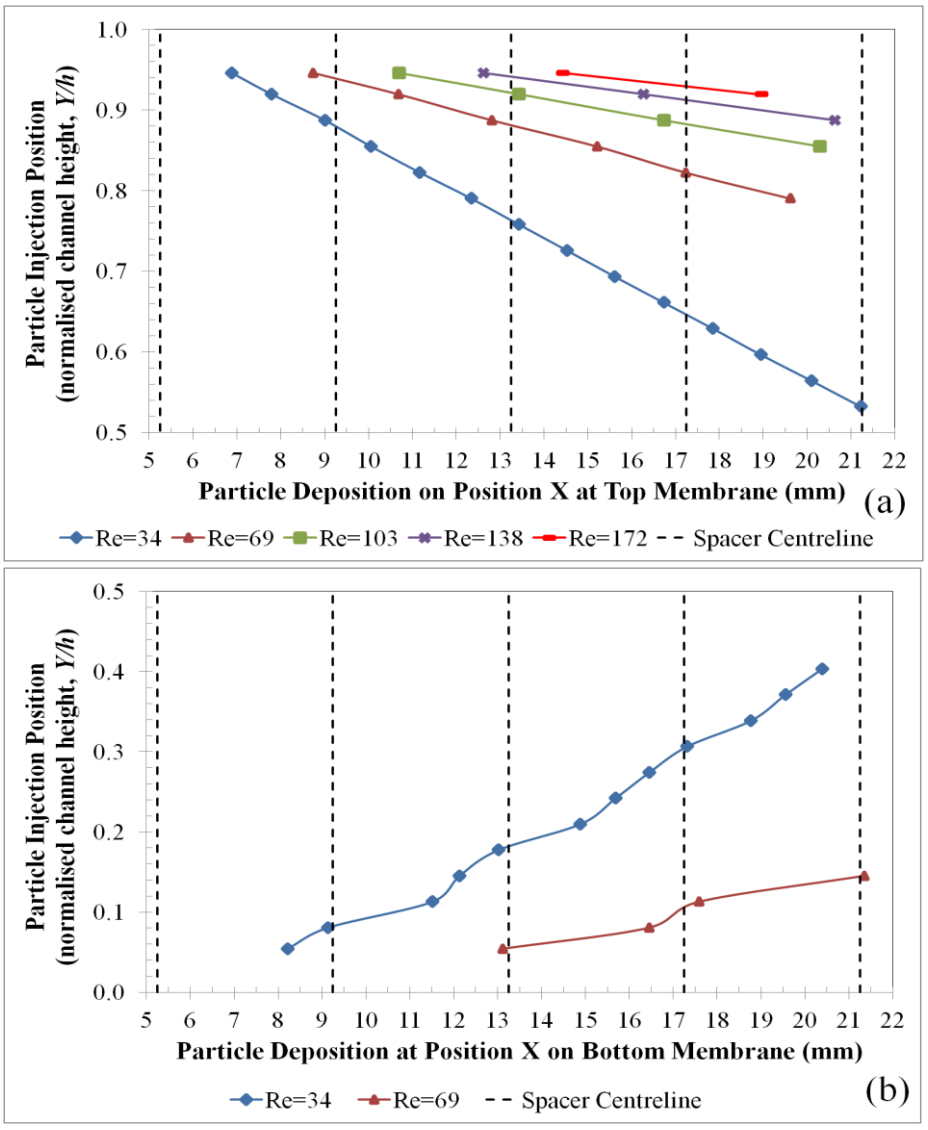

Figure 4.6: Particle deposition on (a) top and (b) bottom membranes across channel length for different *Re*.

Figure 4.7 shows the effect of Reynolds number on the average concentration factor and particle deposition on the top membrane. As *Re* increased, the average concentration factor reduced and the particle travelled further before depositing on the membrane surface. The result implied that the distance the particle travelled before deposition is linearly proportional to the Reynolds number, whereas the decrease of average concentration factor becomes less significant as *Re* increases. The results in Figure 4.7 concluded that higher *Re* is favourable in terms of reducing concentration polarisation and particle deposition.

However, Figure 4.8 shows that as *Re* increased, the pressure drop per unit length also increased, and the increase in the pressure gradient is faster than the decrease in the average concentration polarisation. The results suggested the need of a balance between the increases in feed velocity (to reduce concentration polarisation and particle deposition) and the increases in pressure drop (which causes the increase in energy consumption) across a membrane module.

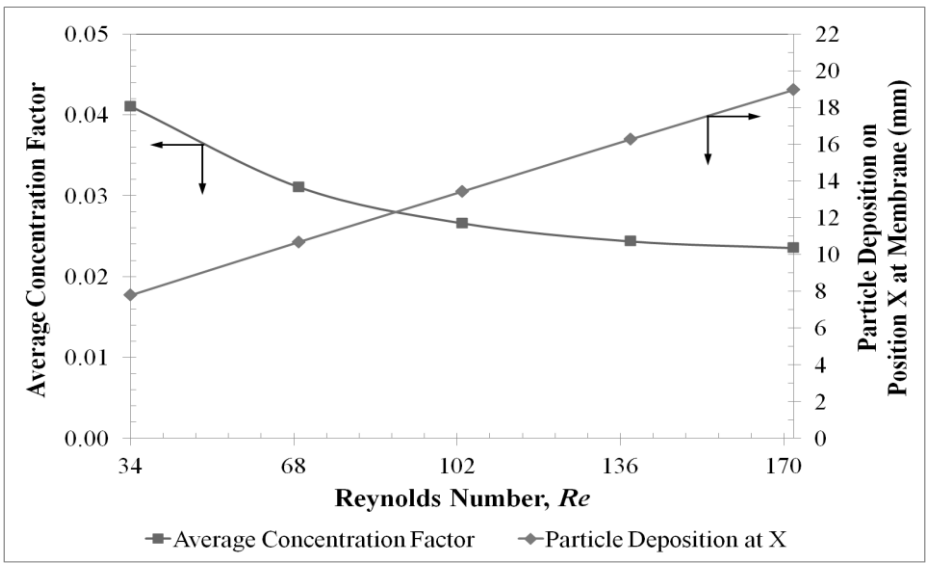

Figure 4.7: Average concentration factor, Γ_{avg} and particle deposition on top membrane across channel length as a function of *Re*.

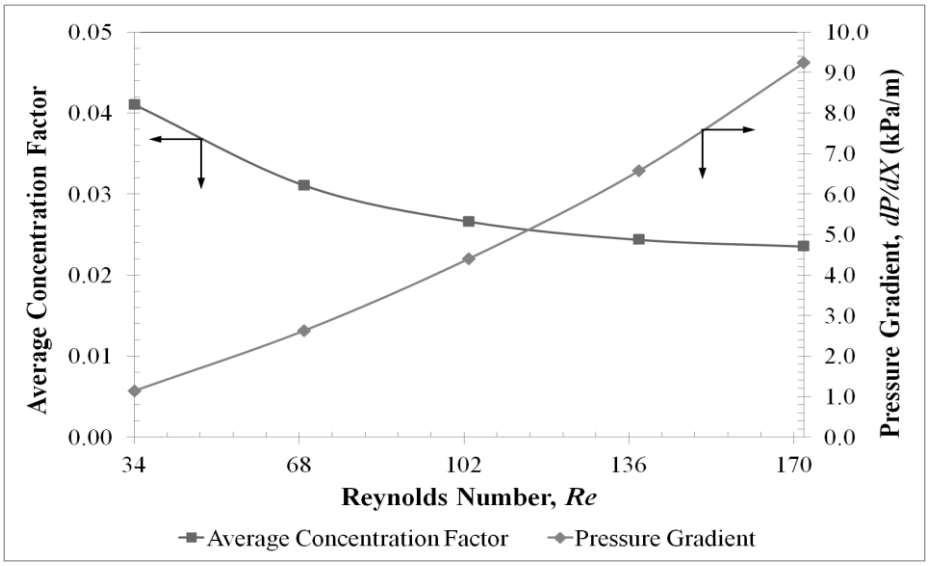

Figure 4.8: Average concentration factor, Γ_{avg} on top membrane and pressure gradient, *dP/dX* across channel length as a function of *Re*.

Mass transfer in a spacer-filled channel and the underlying flow phenomena can be better understood through the dependency of Sherwood number on Reynolds number, given that mass transfer at the membrane is directly proportional to the Sherwood number. In Figure 4.9, the simulated results for channel with spacers arranged in cavity configuration on Sherwood number and power number versus Reynolds number were presented and correlated. It was noted that, as expected, Sherwood number increased with increasing Reynolds number, with the exponent for *Re* equals to 0.39, which fell into the laminar flow regime. Previous work by Fimbres-Weihs, Wiley and Fletcher (2006) determined a value of *Re* exponent of 0.332 for empty channel and 0.605 for zig-zag channel at steady state. Amokrane, et al. (2015a) found a *Re* exponent value of 0.34 for submerged and 0.58 for zig-zag configuration.

The correlation of power number with Reynolds number exhibits the same trend as Sherwood number. As expected, the power number increased with increasing Reynolds number due to the existence of spacers in the channel that

caused higher pressure drop across the channel. The exponent for *Re* in the power law correlation is 2.3, which was found to be in good agreement with the range of 2.25 to 2.83 reported by Haaksman, et al. (2017). Figure 4.10 presents the Sherwood number as a function of power number, which indicated that higher mass transfer in a membrane channel would have to come with a cost of higher power consumption and careful selection of appropriate spacer for a particular process is crucial to optimise the performance of a membrane operation. In the power law correlation between Sherwood number and power number, the exponent for *Pn* was found to be 0.17, which is within the range (0.125 – 0.234) reported by Kavianipour, Ingram and Vuthaluru (2017).

The CFD models from this study were validated against the experimental results as shown in Figure 4.11 and Figure 4.12. The results for pressure gradient and permeate flux agreed within 8% and 9%, respectively.

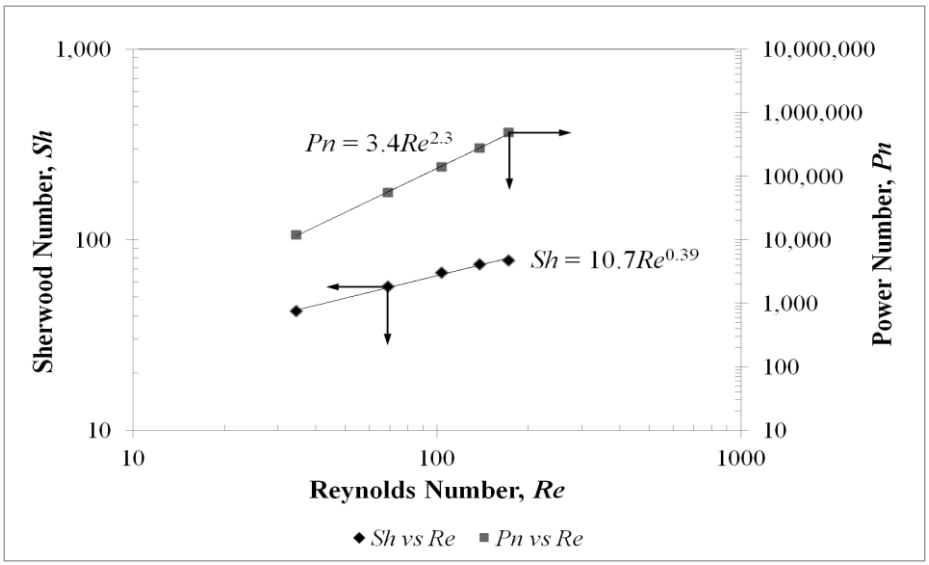

Figure 4.9: Dependence of average Sherwood number and Power number on Reynolds number for cavity configuration.

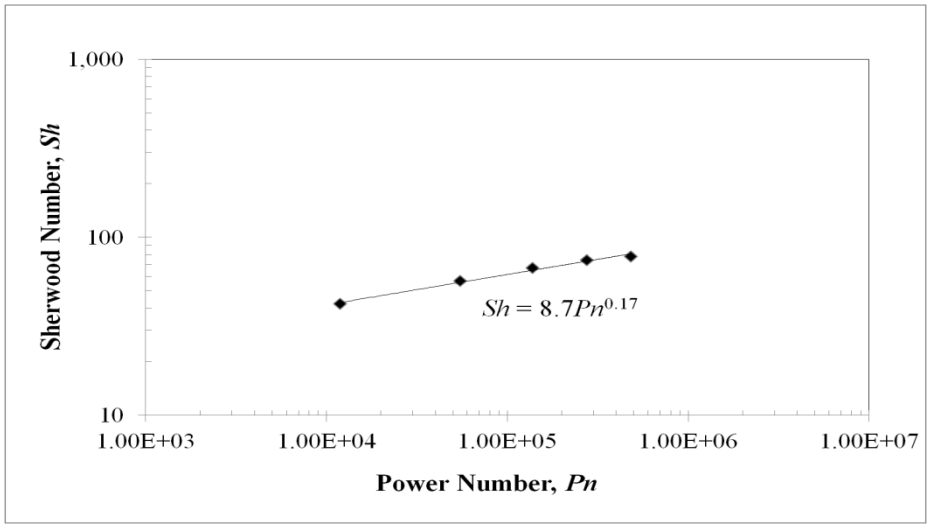

Figure 4.10: Average Sherwood number as a function of Power number for cavity configuration.

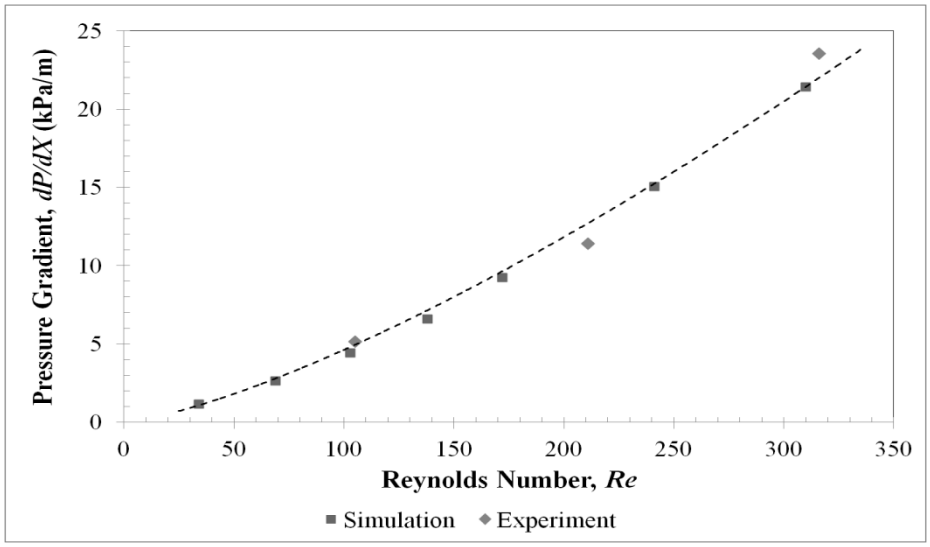

Figure 4.11: Comparison of pressure gradient, *dP/dX* across channel length between simulated data and experimental data as a function of *Re*.

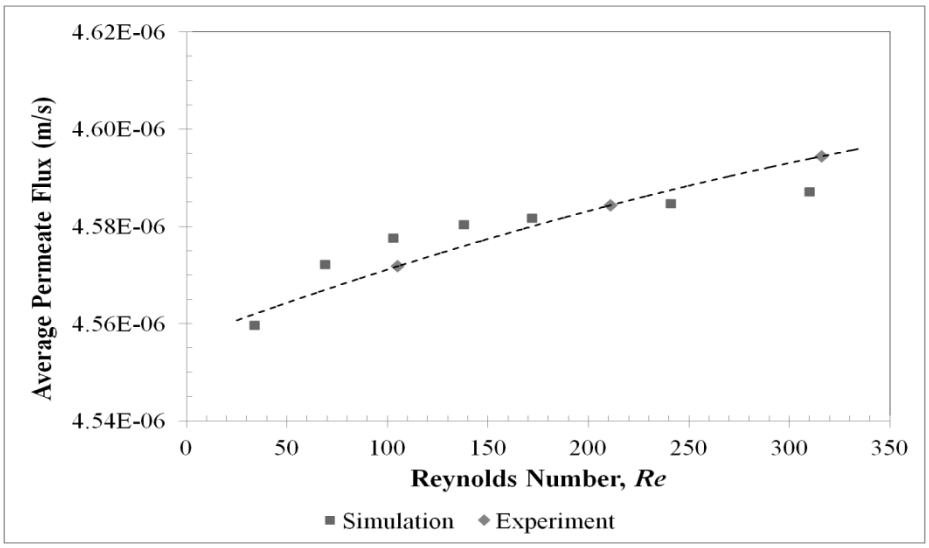

Figure 4.12: Comparison of average permeate flux across channel length between simulated data and experimental data as a function of *Re*.

4.2.3 Flow Field Simulations for New Spacer Designs

4.2.3.1 Modification of Circular Spacers

The modification of circular spacer resulted in four new spacer shapes, i.e. Oval-B, Oval-B tilt, Oval-F and Oval-F tilt. The velocity contour and velocity profile for these spacers are shown in Figure 4.13 and Figure 4.14, respectively. The increment or reduction in the velocity at various locations across the channel indicated that the presence of spacer can play a role as turbulent promoter to alter the flow in a channel. When the fluid flowed through the narrow space above the spacer, it was accelerated and thus high velocity regions could be observed near the top membrane directly above the spacers. Stagnant regions were observed right before and after the spacers at the bottom membrane. Higher velocity implies higher shearing effect on the membrane wall which subsequently can reduce the formation of fouling and concentration polarisation (Amokrane, et al., 2015b).

From the velocity contours in Figure 4.13, the stagnant regions upstream and downstream of the spacers were smaller for tilted shaped spacers, i.e. Oval-B tilt and Oval-F tilt shapes, and the high velocity regions for Oval-B spacer and Oval-F spacer were more spread out compared to the other shapes. Figure 4.14 (b) presents the velocity profiles across the second spacer and the results show that Oval-B and Oval-F spacers generated highest velocity magnitude as the flow passed around the spacers. The results also show that modification of circular spacer shape is able to generate higher velocity magnitude compared to the conventional circle shape. Oval-B and Oval-F spacer not only generated highest velocity, but also caused highest wall shear stress on the membrane as shown in

Figure 4.15. High wall shear stress is desired as it will increase the scouring force on the membrane which could help in reducing concentration polarisation effect and fouling on the membrane. However, the better performance in terms of higher wall shear stress for Oval-B and Oval-F spacers come with a cost, namely higher power consumption, as can be observed in Figure 4.16.

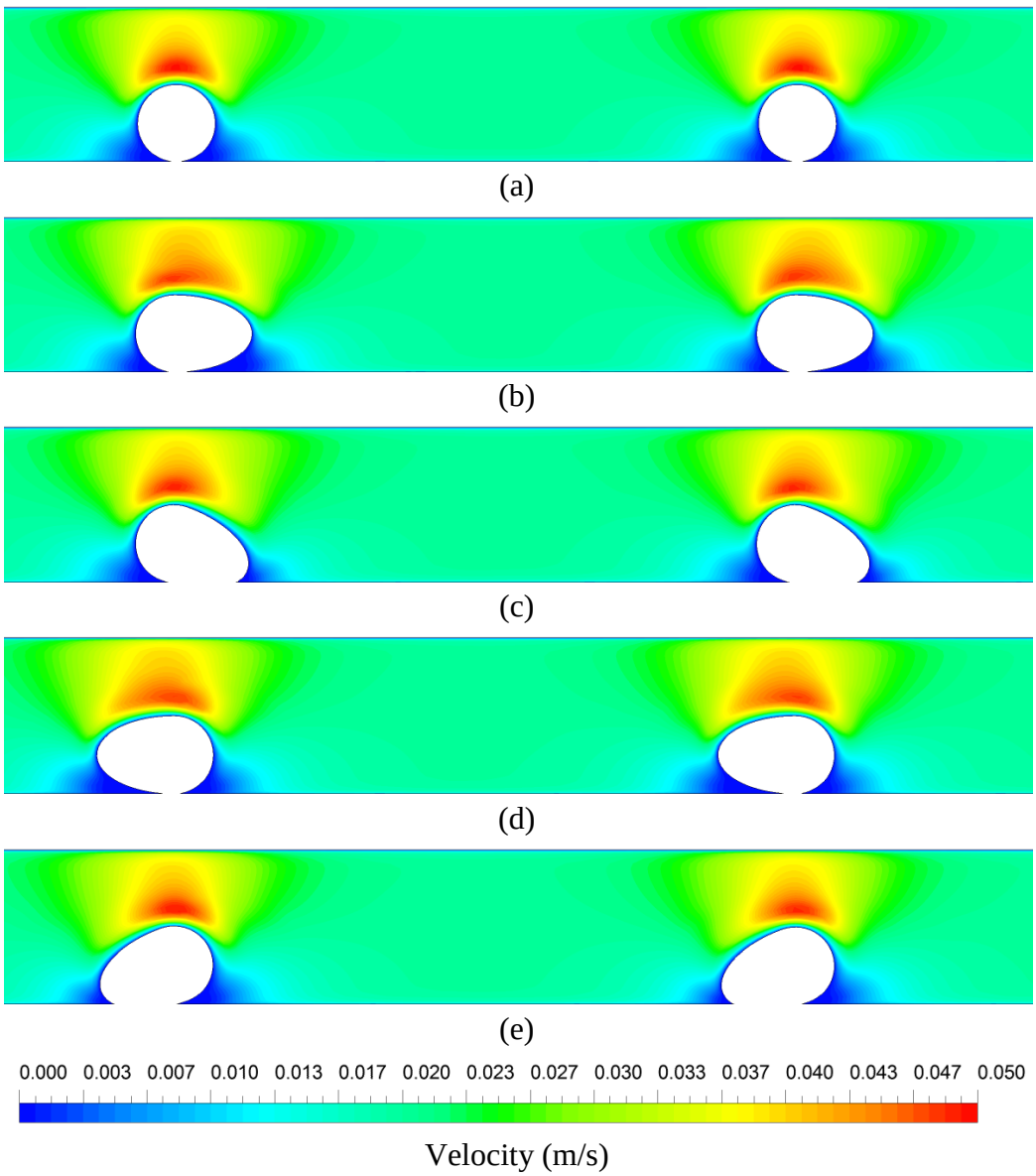

Figure 4.13: Velocity contours for modification of circular spacer shapes. (a) Circle, (b) Oval-B, (c) Oval-B tilt, (d) Oval-F and (e) Oval-F tilt. Flow direction is from left to right.

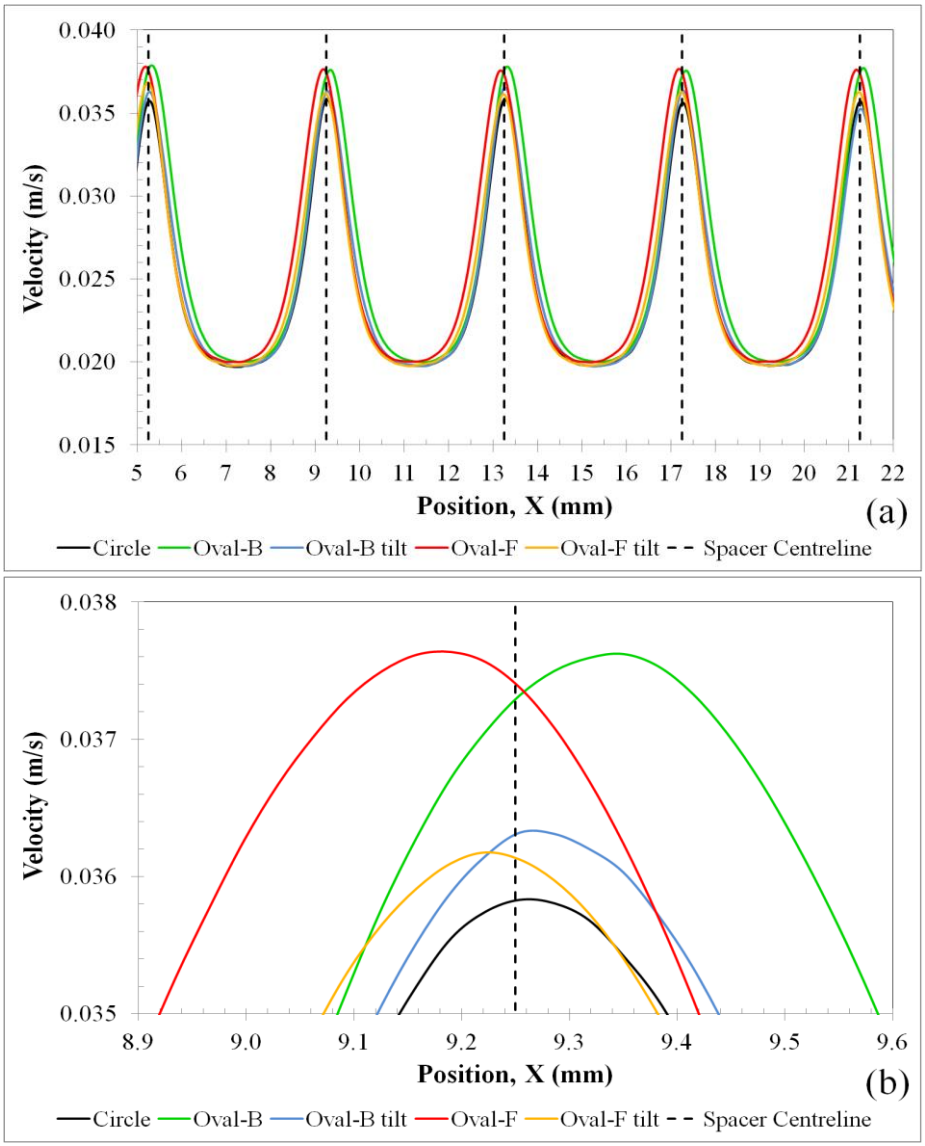

Figure 4.14: Velocity profiles at Y = 0.95 mm across (a) channel length and (b) second spacer for modification of circular spacer shapes.

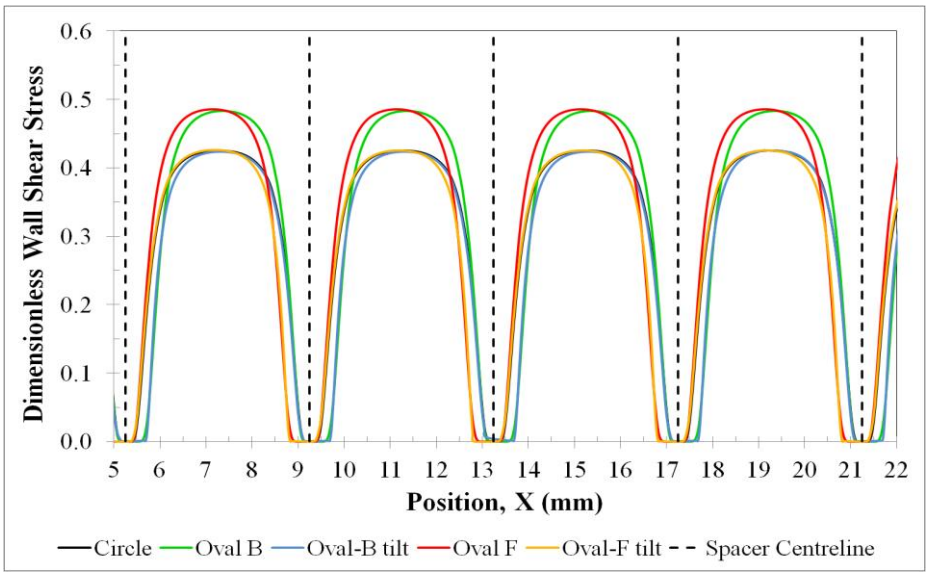

Figure 4.15: Dimensionless wall shear stress at bottom membrane across channel length for modification of circular spacer shapes.

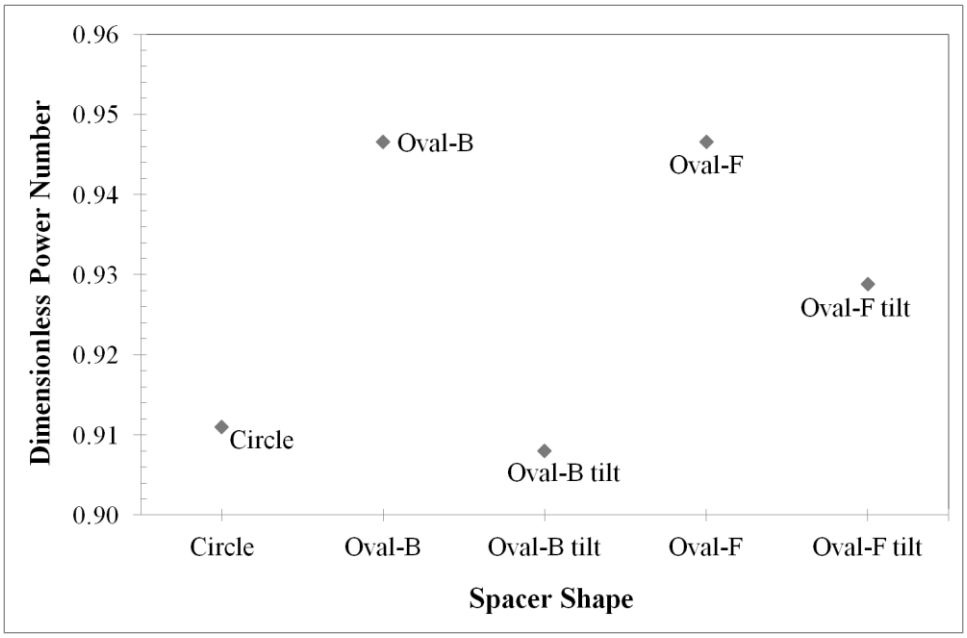

Figure 4.16: Dimensionless power number across channel length for modification of circular spacer shapes.

Based on the performance comparison as shown in Table 4.2, spacer shapes that have lower wall shear stress at the bottom membrane also have lower power number. Since lower power number means lower energy consumption in the membrane module, spacer shapes with lower power number, i.e. Circle and Oval-B tilt shapes are better designs in terms of energy consumption.

Table 4.2: Performance comparison for modification of circular spacers.

Shape	Wall Shear Stress at Bottom	Power Number
Circle	low	low
Oval-B	high	high
Oval-B tilt	low	low
Oval-F	high	high
Oval-F tilt	low	medium

4.2.3.2 Modification of Triangular Spacers

The modification (rotation) of triangular spacer resulted in three new spacer shapes, i.e. T026deg, T090deg and T116deg. The velocity contours in Figure 4.17 show that the pointed tip of triangular spacers can accelerate and cause a very high increase in the velocity magnitude around that region. The stagnant regions upstream and downstream of the spacers are smaller for Triangle spacer compared to the rest. This is attributed to the absence of "hidden" areas between the spacer and the membrane, whereby its slanted sides provide a smoother and unobstructed path to the flow (Teoh and Lai, 2014).

Referring to Figure 4.18, the velocity magnitude for T116deg spacer as the flow passed across the spacer is very much higher compared to the other shapes. The highest velocity magnitude generated for T116deg spacer is due to the spacer geometry, whereby the base of its triangle that was parallel to the top membrane created a narrow "tunnel" that accelerated the flow that passed through. The reduction in cross-sectional area causes an increase in the fluid velocity. For Triangle spacer, because the "tunneling effect" was very much lesser compared to the other shapes, it has the lowest velocity magnitude among the triangular spacers.

T116deg spacer also causes the highest wall shear stress on the membrane as depicted in Figure 4.19, followed by Triangle, T090deg and T026deg shapes. The power consumption across the channel for these spacers (Figure 4.20) also show similar trend where the dimensionless power number is the highest for T116deg spacer and the lowest for T026deg spacer.

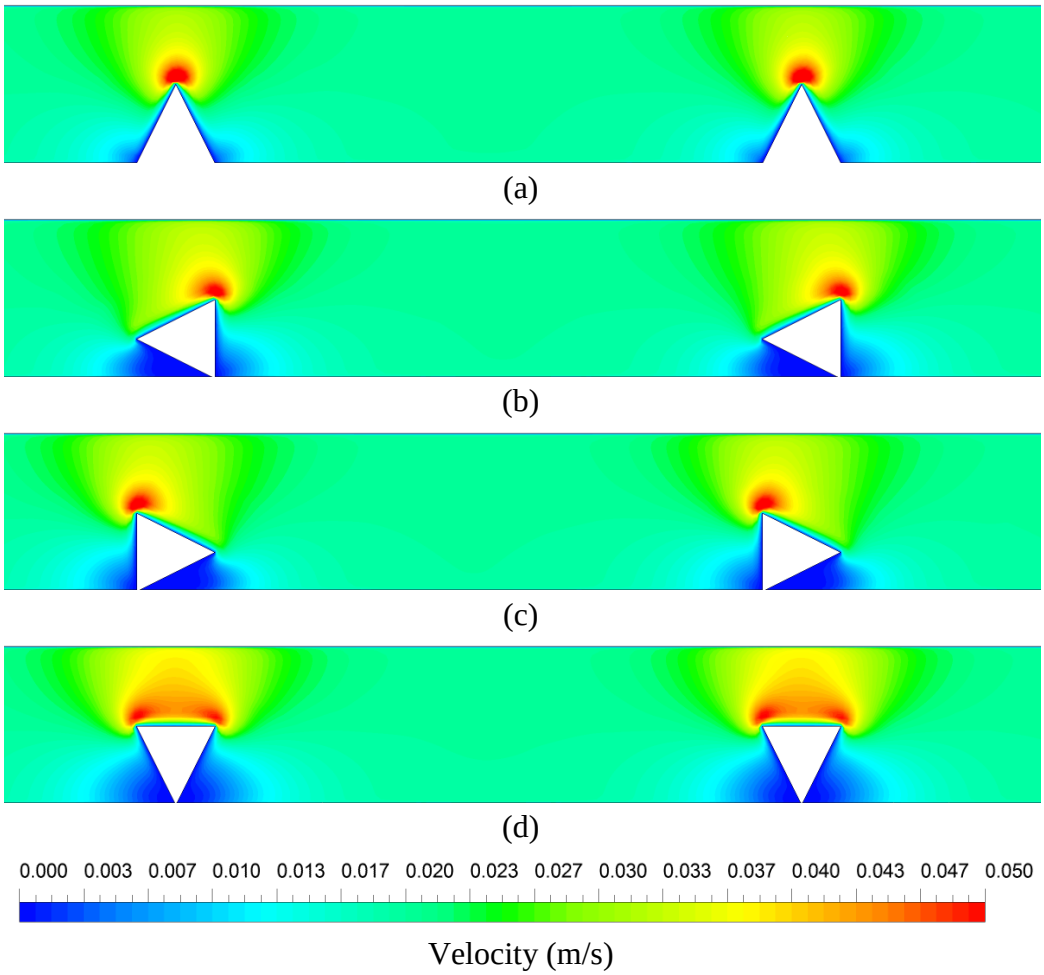

Figure 4.17: Velocity contours across channel length for modification of triangular spacer shapes. (a) Triangle, (b) T026deg, (c) T090deg and (d) T116deg. Flow direction is from left to right.

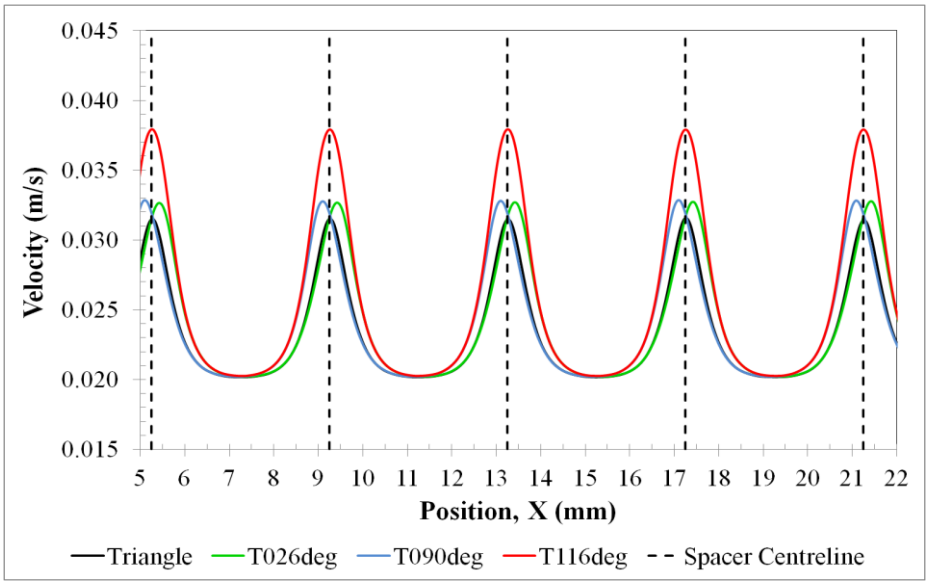

Figure 4.18: Velocity profiles at *Y* = 0.95 mm across channel length for modification of triangular spacer shapes.

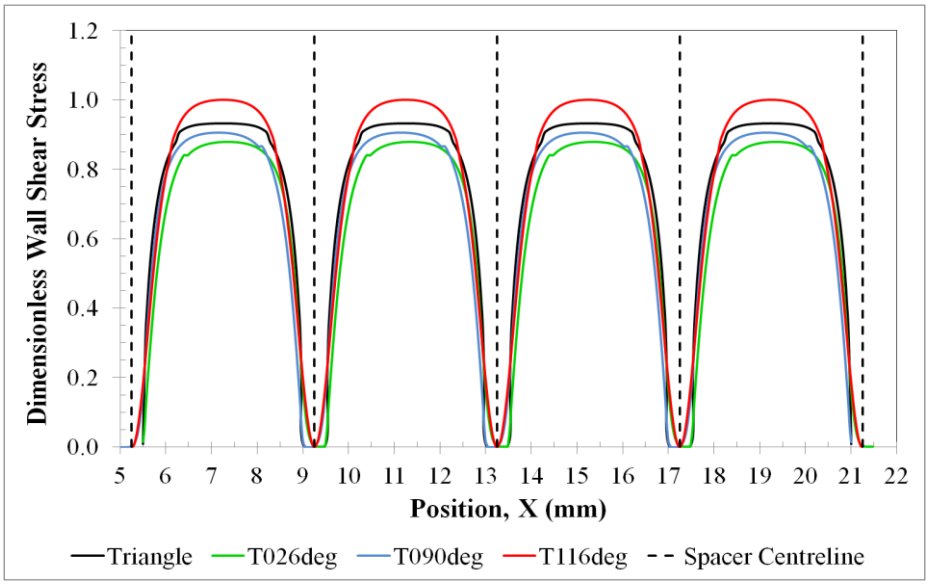

Figure 4.19: Dimensionless wall shear stress at bottom membrane across channel length for modification of triangular spacer shapes.

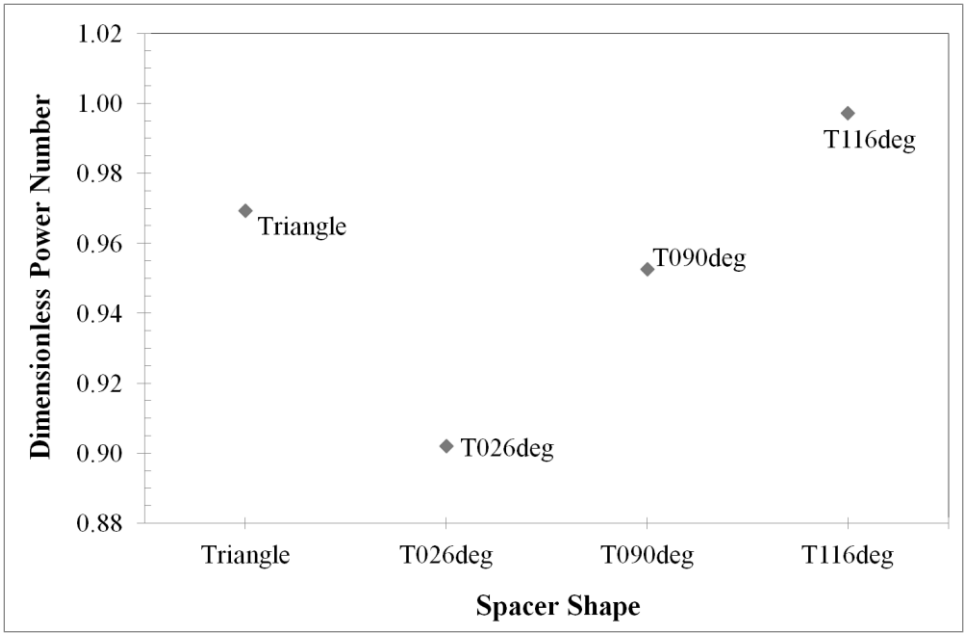

Figure 4.20: Dimensionless power number across channel length for modification of triangular spacer shapes.

Based on the performance comparison as shown in Table 4.3, spacer shapes that have lower wall shear stress also have lower power number. Since lower power number means lower energy consumption in the membrane channel,

spacer shape with lowest power number, i.e. T026deg shape is a better design in terms of energy consumption.

Table 4.3: Performance comparison for modification of triangular spacers.

Shape	Wall Shear Stress at Bottom	Power Number
Triangle	medium	medium
T026deg	low	low
T090deg	medium	medium
T116deg	high	high

4.2.3.3 Modification of Square Spacers

The modification of square spacer resulted in two new spacer shapes, i.e. Arc 0.25 and Arc 0.50. As discussed in the previous section, pointed tip (Square spacer) could accelerate the flow nearby and caused a high increase in the velocity magnitude around that region (Figure 4.21). This effect can also be observed from the velocity profiles of the different spacers (Figure 4.22) where Square spacer has the highest velocity magnitude. The stagnant regions right before and after the spacers were lesser for Arc 0.50 spacer compared to the rest due to its geometry that has a bigger curvature which provides a smoother path for the flow and reduces stagnant region.

Square spacer also causes the highest wall shear stress on the membrane as shown in Figure 4.23, followed by Arc 0.50 and Arc 0.25 shapes. Pressure drop is an unavoidable phenomenon in a spacer-filled channel and the extent of pressure drop, which can be translated into power number, depends on the geometry of the spacer in the channel. Figure 4.24 presents the dimensionless

power number for the modification of square spacer shapes, which shows that modification of square spacers are better in term of lower power consumption.

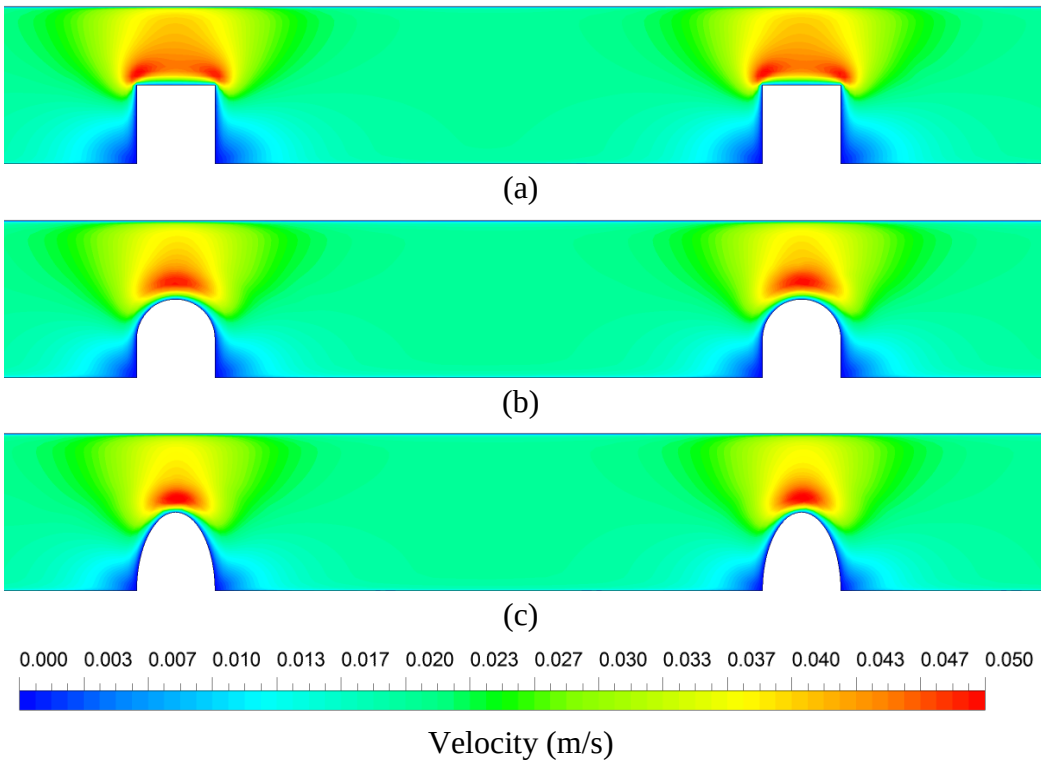

Figure 4.21: Velocity contours across channel length for modification of square spacer shapes. (a) Square, (b) Arc 0.25 and (c) Arc 0.50. Flow direction is from left to right.

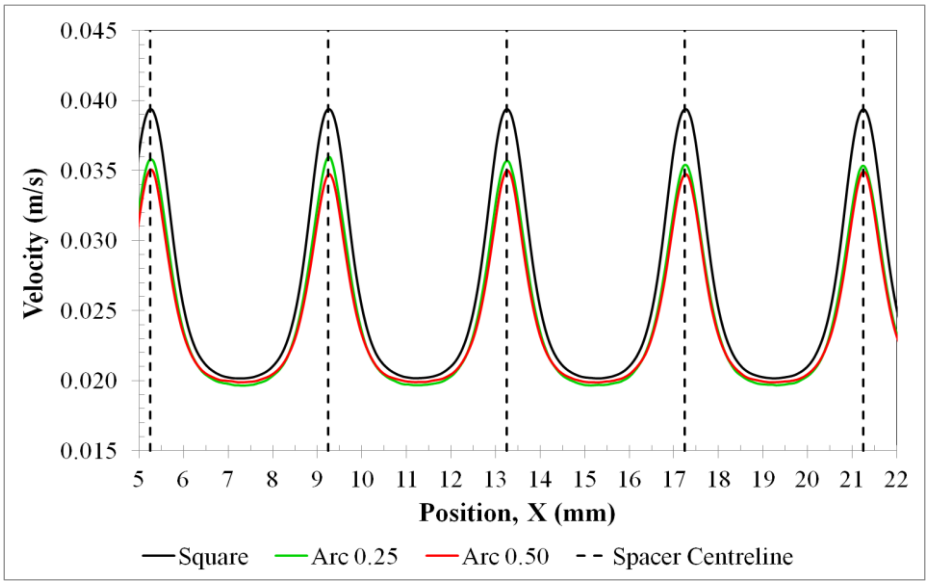

Figure 4.22: Velocity profiles at *Y* = 0.95 mm across channel length for modification of square spacer shapes.

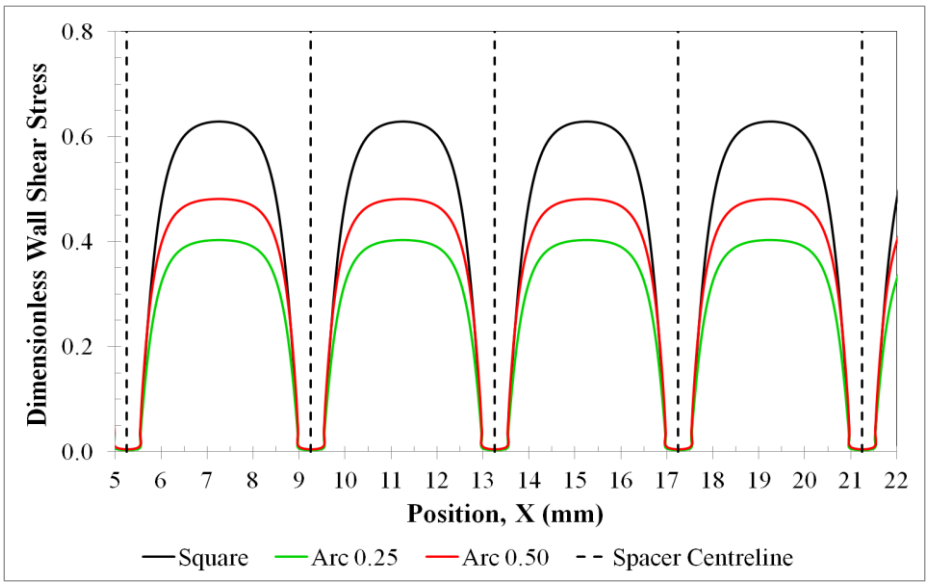

Figure 4.23: Dimensionless wall shear stress at bottom membrane across channel length for modification of square spacer shapes.

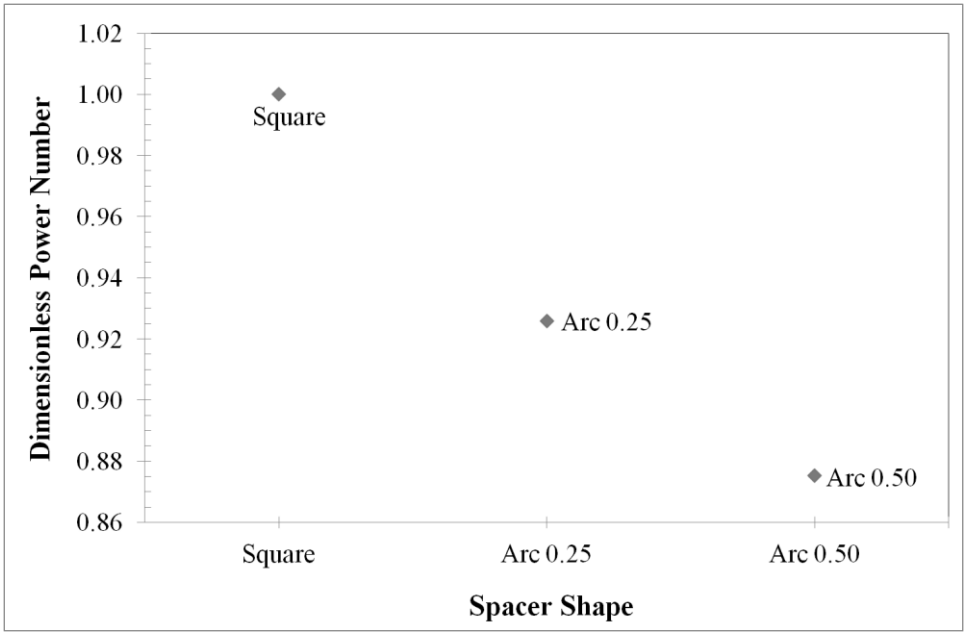

Figure 4.24: Dimensionless power number across channel length for modification of square spacer shapes.

Based on the performance comparison as shown in Table 4.4, Arc 0.50 shape is a better design since it has the lowest power number and at the same time still be able to cause medium wall shear stress on the membrane compared to the other two shapes.

Table 4.4: Performance comparison for modification of square spacers.

Shape	Wall Shear Stress at Bottom	Power Number
Square	high	high
Arc 0.25	low	medium
Arc 0.50	medium	low

4.2.3.4 Summary of Spacer Designs with Better Performance

The spacer designs with better performance from the modifications of circular, triangular and square shape as discussed in the previous sections, i.e. circle, Oval-B tilt, T026deg and Arc 0.50 shapes, are compared and summarised in this section. Figure 4.25 depicts the velocity profiles for these four spacer shapes and the results show that Oval-B tilt shape has the highest velocity magnitude and T026deg shape has the lowest as the flow passed across the spacer. However, in terms of wall shear stress (Figure 4.26), T026deg shape has the highest and the circular shapes have the lowest.

The dimensionless power number for all the spacer shapes investigated in this work is shown in Figure 4.27. The modification of square spacer shapes show lower power consumption compared to the modification of circular or triangular spacer shapes.

Based on the performance comparison as shown in Table 4.5, Arc 0.50 shape is a better design among the other selected spacers since it can provide a good balance by having medium wall shear stress (which could help in mitigating concentration polarisation and fouling on the membrane) and lowest power number (which means lower power consumption).

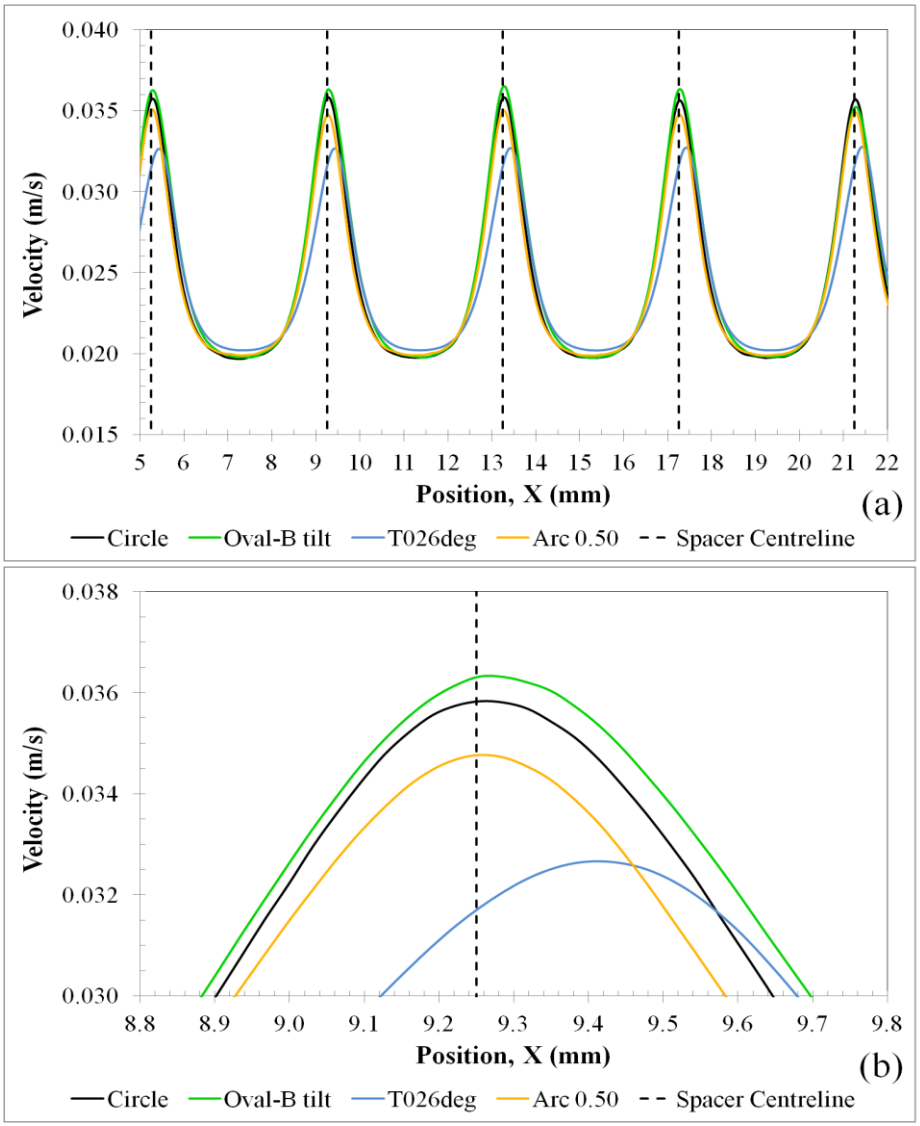

Figure 4.25: Velocity profiles at Y = 0.95 mm across (a) channel length and (b) second spacer for selected spacer shapes.

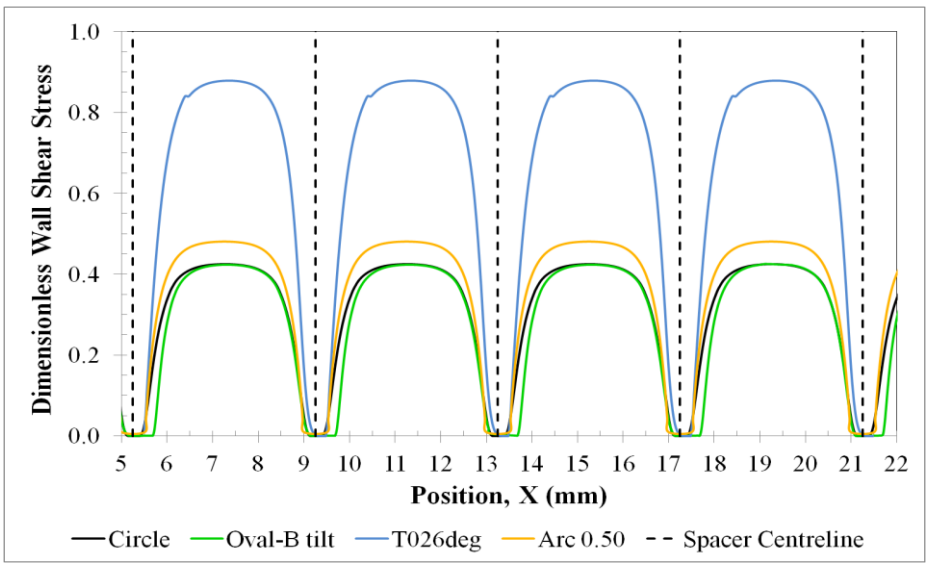

Figure 4.26: Dimensionless wall shear stress at bottom membrane across channel length for selected spacer shapes.

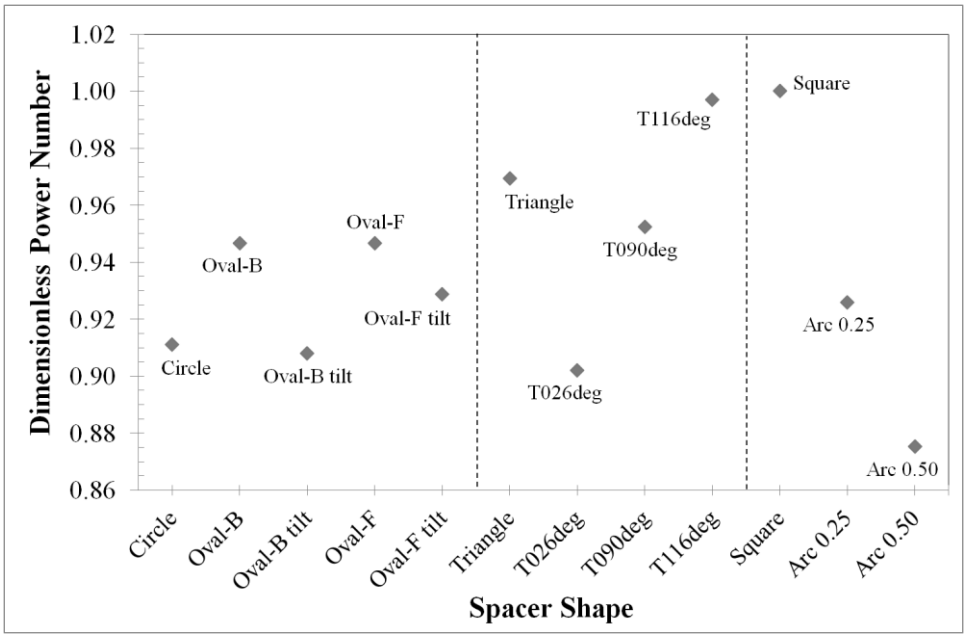

Figure 4.27: Dimensionless power number across channel length for new designs of spacer shapes.

Table 4.5: Performance comparison for selected spacer shapes.

Shape	Wall Shear Stress at Bottom	Power Number
Circle	low	high
Oval-B tilt	low	high
T026deg	high	high
Arc 0.50	medium	low

4.2.4 Studies on Concentration Polarisation

4.2.4.1 Modification of Circular Spacers

Figure 4.28 illustrates the contours of concentration factor for modification of circular spacer shapes. From the contours, it can be observed that the highest concentration occurred in the "hidden" regions between the spacers and the bottom membrane. From the results in Section 4.2.3.1, these were the stagnant regions. Since the stagnant regions were smaller for tilted spacers,

namely Oval-B tilt and Oval-F tilt spacers, the concentration polarisation phenomenon was also lesser in the channel equipped with these spacers. This same phenomenon was also observed by Amokrane, et al. (2015b).

Figure 4.29 demonstrates that the concentration factor increased along the channel, but dropped as the flow encountered the spacers. At the bottom membrane (Figure 4.29 (b)), the high concentration factor right next to the spacers were due to the stagnant regions as discussed above. As the fluid flows along the channel, it can be observed that the effect of different spacer shapes on concentration factor became obvious. Initially (between the first and second spacers), all the spacers exhibited almost the same concentration factor, but when the flow reached the fifth spacer, some spacers give lower concentration factor than the others. Channel with Oval-B and Oval-F spacers exhibits lower concentration factor at the top membrane due to the higher velocity generated by these spacers (Section 4.2.3.1), whereas at the bottom membrane, channel with Oval-B tilt and Oval-F tilt spacers exhibits lower concentration factor.

Figure 4.30 shows the *Y*-position where the concentration started to build-up and how it evolved. The concentration factor started to increase around 0.15 mm from the bottom membrane and 0.10 mm from the top membrane. From the top and bottom zoom boxes in the figure, initially when the concentration started to build-up, Oval-F and Oval-B spacers give lower concentration factor at the top membrane, and Oval-B and Oval-B tilt spacers at the bottom membrane. However, as we move nearer to the membrane, the concentration factor profile changes for different spacers, and finally at the membrane surface, the concentration factor for different spacers is as demonstated in Figure 4.29.

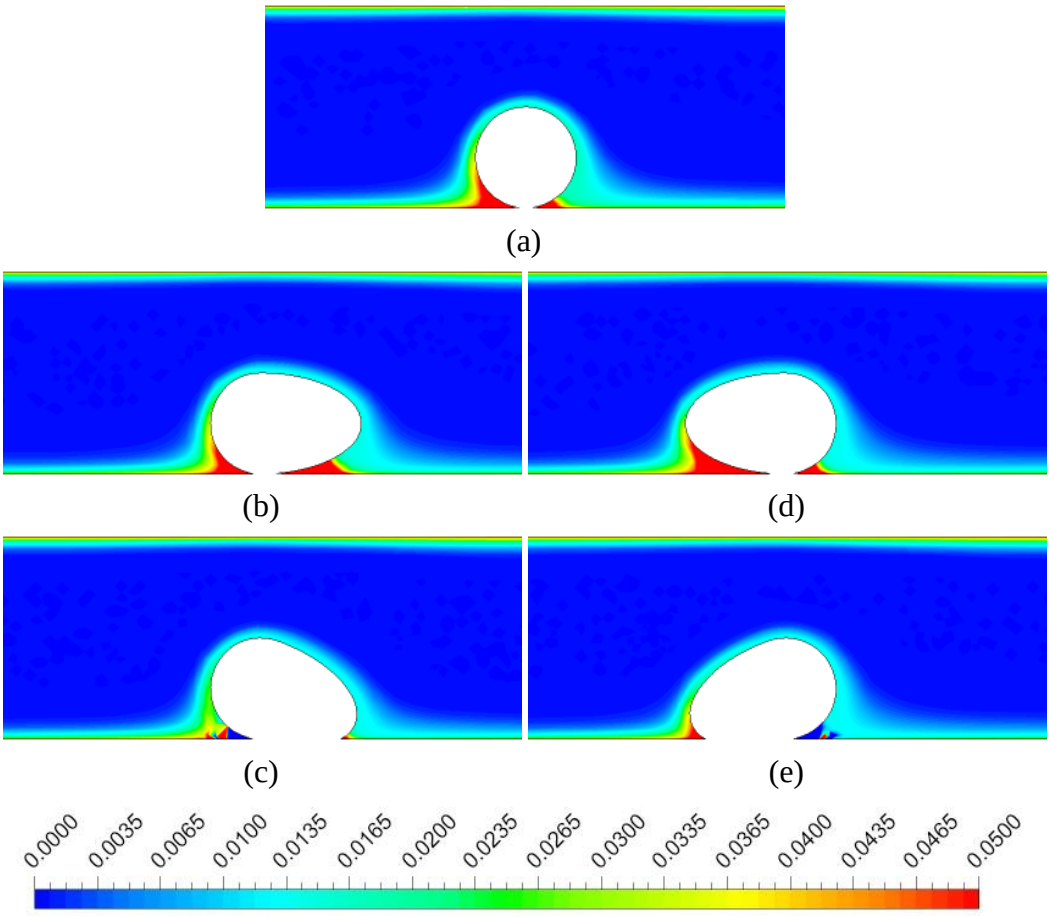

Figure 4.28: Contours of concentration factor, Γ for modification of circular spacer shapes. (a) Circle, (b) Oval-B, (c) Oval-B tilt, (d) Oval-F and (e) Oval-F tilt. Flow direction is from left to right.

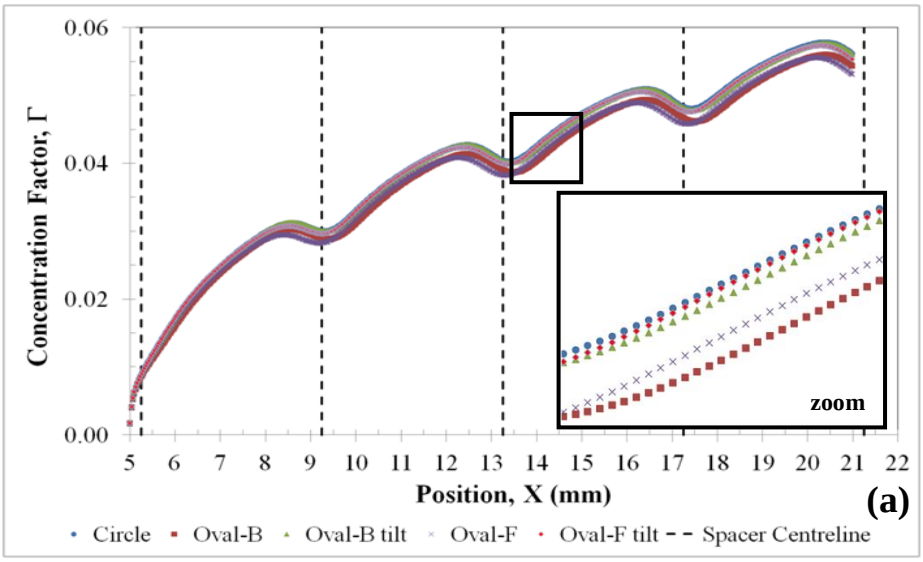

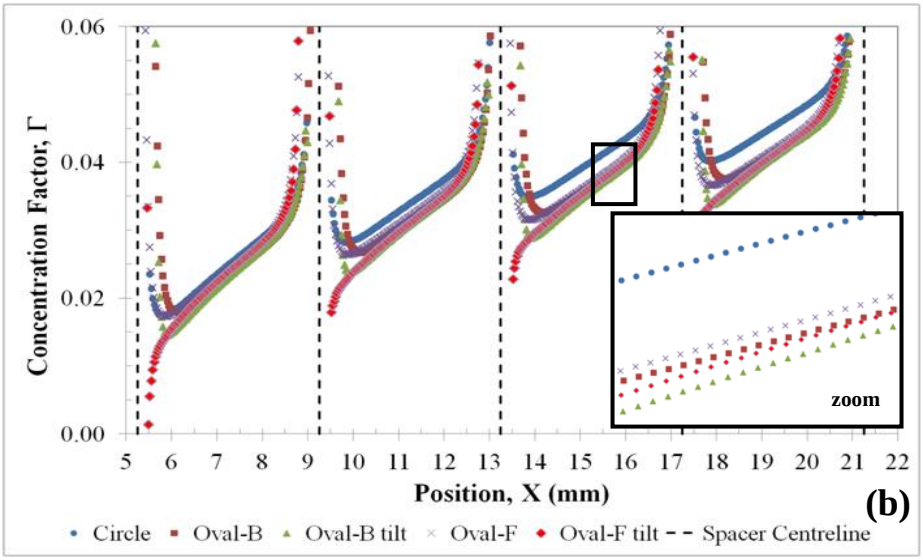

Figure 4.29: Profiles of concentration factor, Γ on (a) top and (b) bottom membranes across channel length for modification of circular spacer shapes.

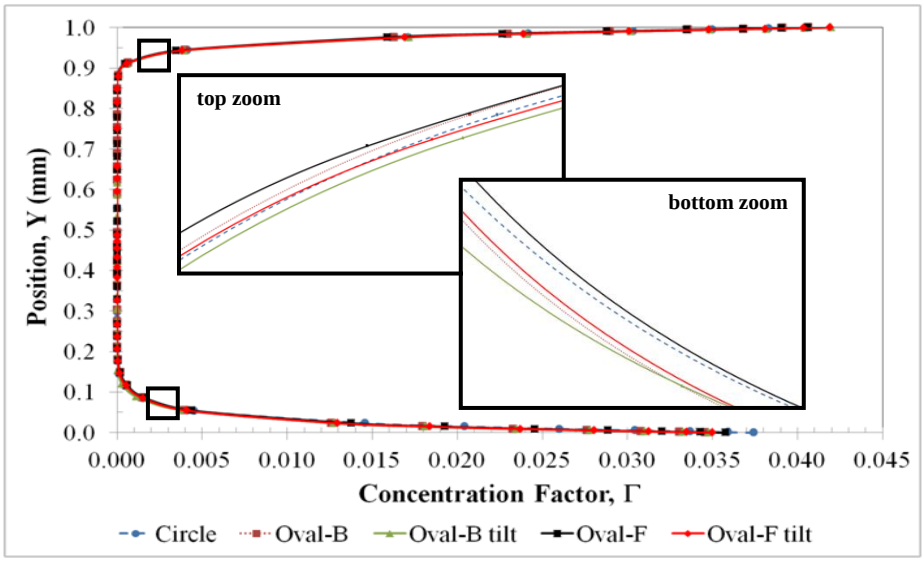

Figure 4.30: Profiles of concentration factor, Γ along *Y*-position at location *X* = 15 mm for modification of circular spacer shapes.

4.2.4.2 Modification of Triangular Spacers

Figure 4.31 shows the contours of concentration factor for modification of triangular spacer shapes. The highest concentration occurred around the stagnant regions (Section 4.2.3.2) between the spacers and the bottom membrane. The Triangle spacer has the least concentration factor due to its geometry, whereby its

slanted sides provide unobstructed path to the flow and better mixing of the fluid. This trend also can be observed in Figure 4.32 (b). From Figure 4.32 (a), the top membrane exhibits lower concentration factor for channel with T116deg spacer due to the higher velocity generated by these spacers (Section 4.2.3.2) that can increase the scouring force on the membrane surface (Teoh and Lai, 2014).

Figure 4.33 illustrates the height of the channel where the concentration started to build-up and how it evolved. The concentration factor started to increase around 0.20 mm from the bottom membrane and 0.10 mm from the top membrane. The evolution of concentration factor profiles for various spacers as we move nearer to the membrane is consistent with the results in Figure 4.32, where channel with T116deg spacer and Triangle spacer exhibit lower concentration factor at the top and bottom membrane, respectively.

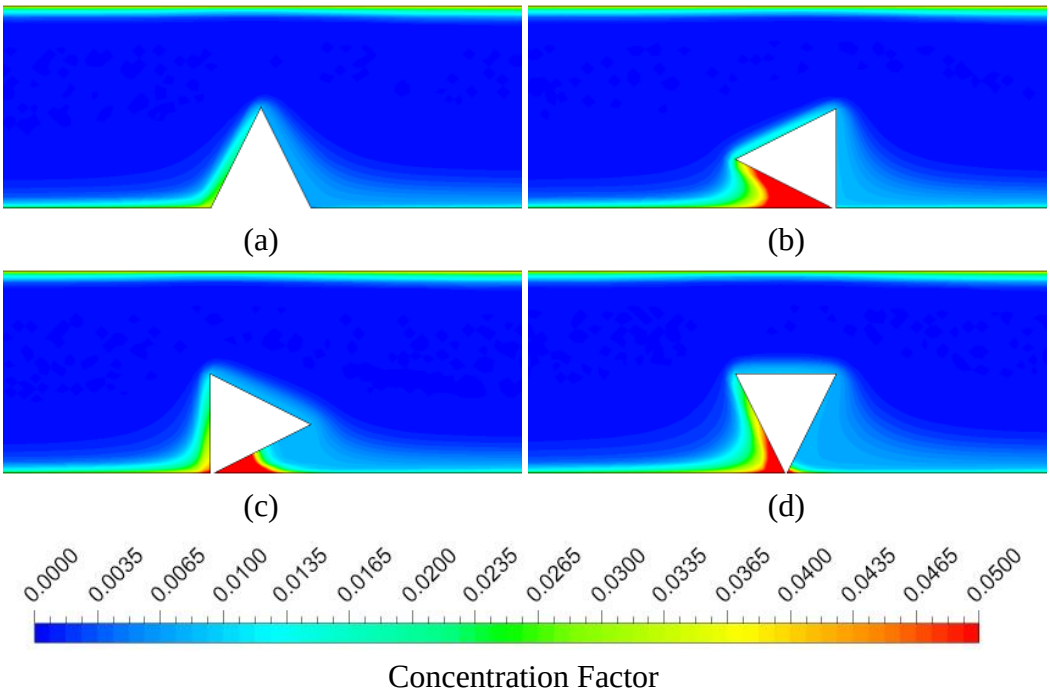

Figure 4.31: Contours of concentration factor, Γ for modification of triangular spacer shapes. (a) Triangle, (b) T026deg, (c) T090deg and (d) T116deg. Flow direction is from left to right.

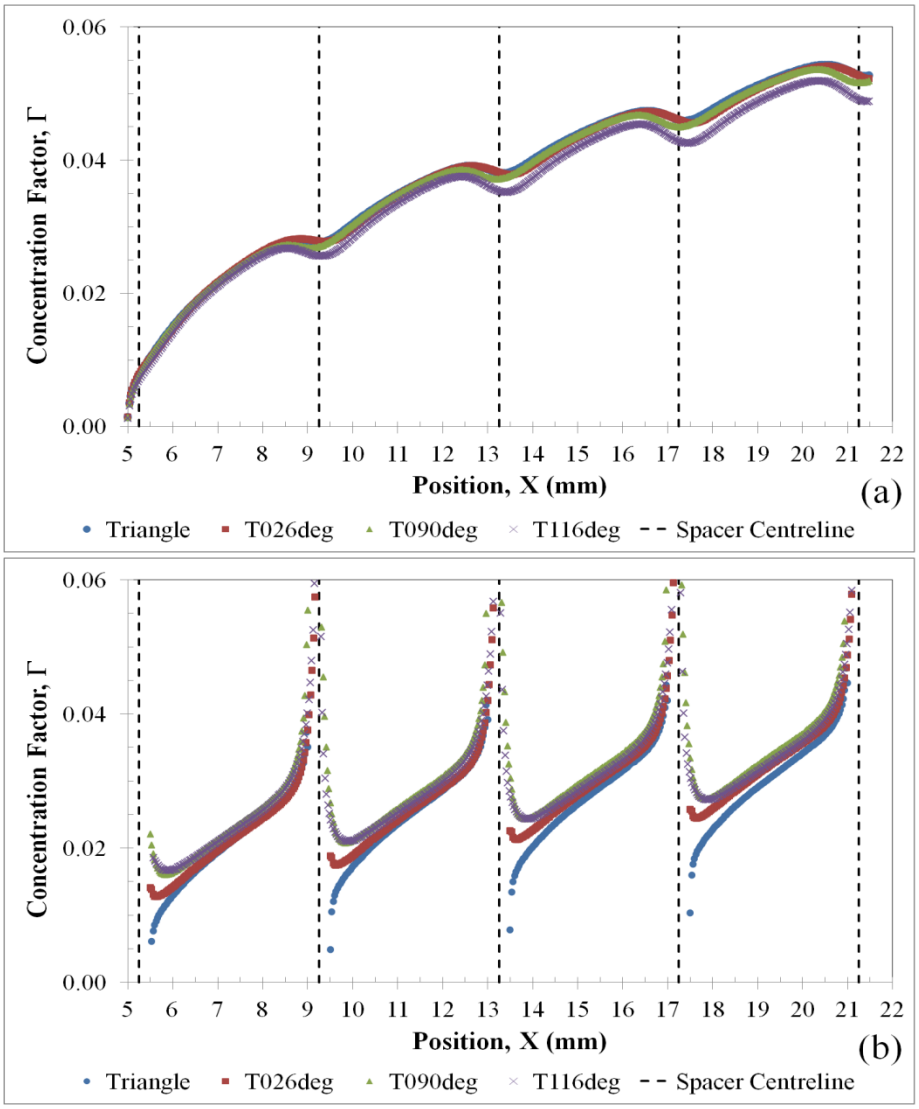

Figure 4.32: Profiles of concentration factor, Γ on (a) top and (b) bottom membranes across channel length for modification of triangular spacer shapes.

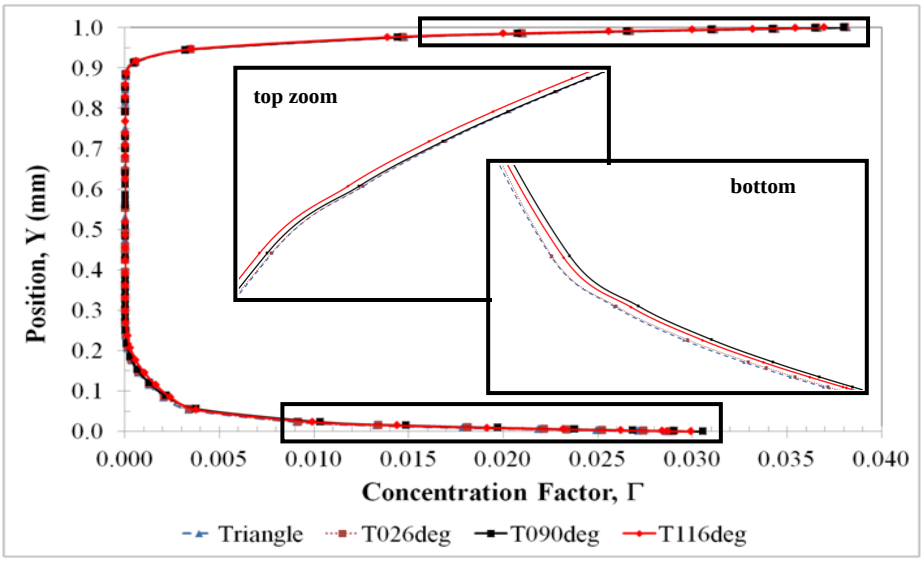

Figure 4.33: Profiles of concentration factor, Γ along *Y*-position at location *X* = 15 mm for modification of triangular spacer shapes.

4.2.4.3 Modification of Square Spacers

Figure 4.34 illustrates the contours of concentration factor for modification of square spacer shapes showing that the highest concentration occurred in the region before the spacers. These high concentration regions are much smaller compared to circular or triangular spacers (Figure 4.28 and Figure 4.31) due to the absence of "hidden" region between the spacer and the bottom membrane. From Figure 4.35, the effect of different spacer shapes on concentration factor is very obvious as the fluid flow down the channel, where it can be observed that Square spacer is very effective in reducing concentration polarisation phenomenon on the membranes.

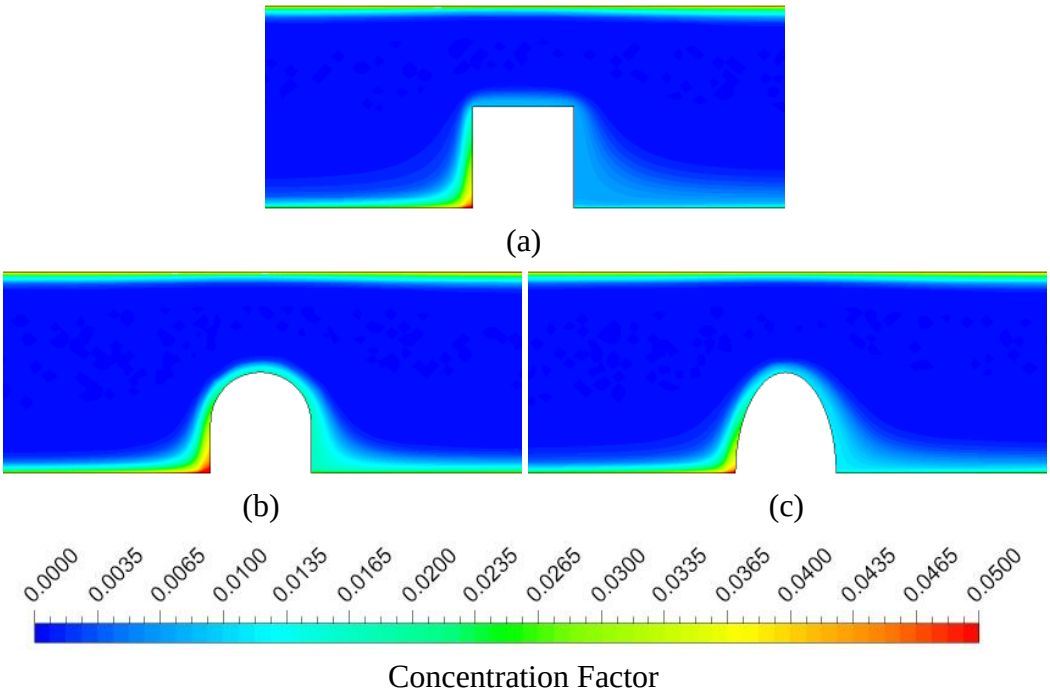

Figure 4.34: Contours of concentration factor, Γ for modification of square spacer shapes. (a) Square, (b) Arc 0.25 and (c) Arc 0.50. Flow direction is from left to right.

Figure 4.36 shows the build-up and evolution of concentration polarisation along the *Y*-position. The concentration factor started to increase around 0.10 mm from the top membrane and 0.20 mm from the bottom membrane for Square spacer and Arc 0.50 spacer, and 0.15 mm for Arc 0.25 spacer. Although initially the concentration for Square spacer build-up earlier and higher, as the flow moves towards the bottom membrane, the concentration became lesser compared to the other two spacer shapes. This suggested that the concentration profile can be significantly altered by having different spacers in a membrane channel (Ahmad and Lau, 2006).

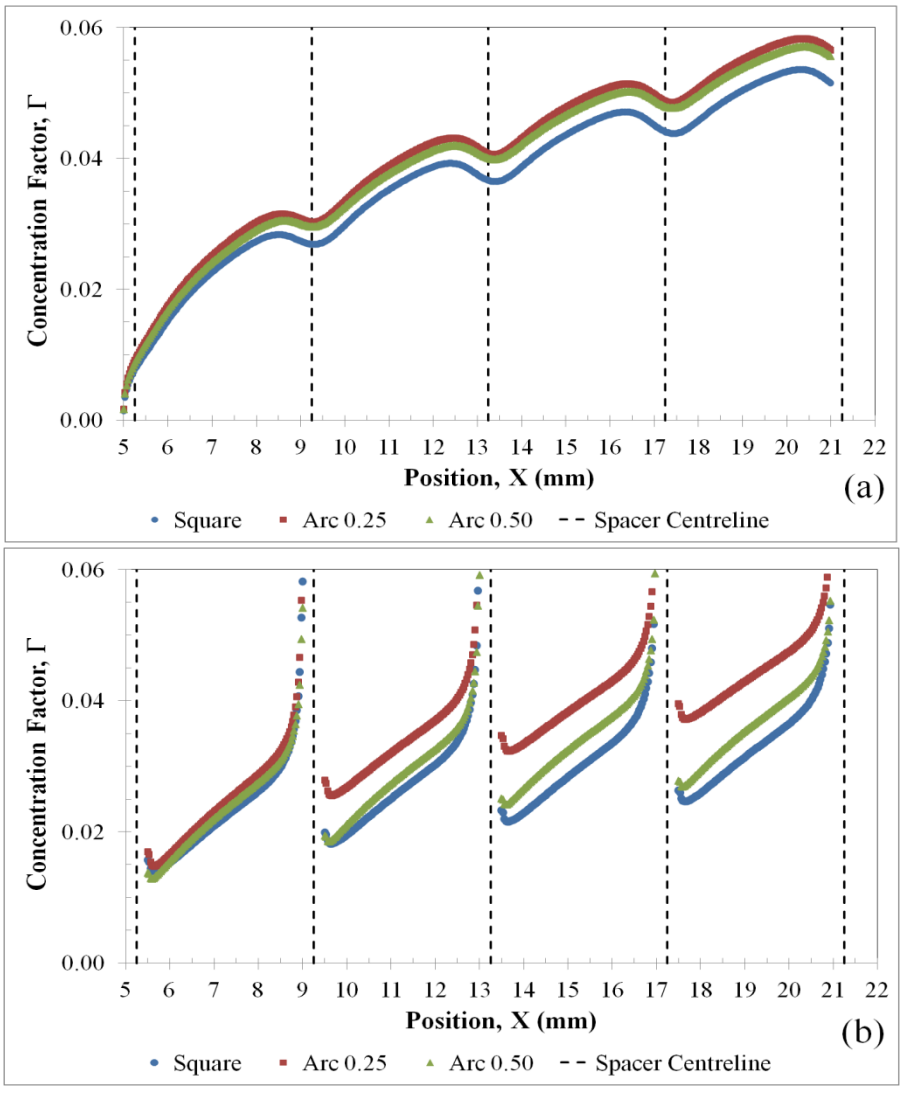

Figure 4.35: Profiles of concentration factor, Γ on (a) top and (b) bottom membranes across channel length for modification of square spacer shapes.

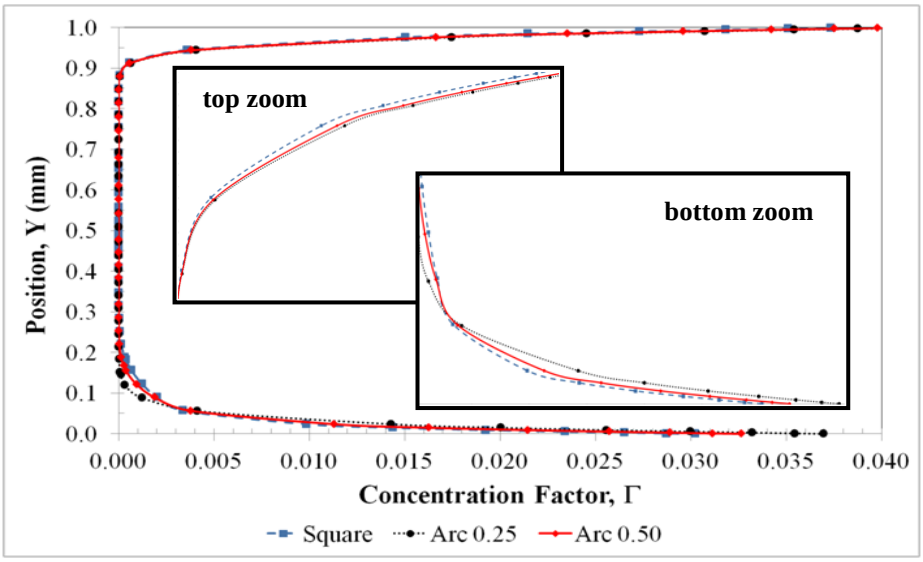

Figure 4.36: Profiles of concentration factor, Γ along *Y*-position at location *X* = 15 mm for modification of square spacer shapes.

4.2.4.4 Average Mass Transfer Coefficient

Table 4.6 summarised the average mass transfer coefficient between the first and last spacer for all the spacers studied in this work. The mass transfer coefficient results agreed with the concentration factor results where lower concentration factor implied higher mass transfer. The modification of triangular spacer shapes perform slightly better in term of mass transfer, followed by modification of square spacer shapes and modification of circular spacer shapes. However, if took power consumption into account (Figure 4.27), modification of square spacer shapes are a better choice that in view that they can provide a good balance between mass transfer and power consumption.

Table 4.6: Average mass transfer coefficient, *k* across channel length.

Shape	Average Mass Transfer Coefficient, *k* (m/s) 10^{-4}	
	Top	Bottom
Circle	1.2639	1.3639
Oval-B	1.3191	1.4139
Oval-B tilt	1.2690	1.4834
Oval-F	1.3134	1.4388
Oval-F tilt	1.2685	1.6624
Triangle	1.5892	2.0170
T026deg	1.5964	1.7141
T090deg	1.6014	1.5850
T116deg	1.6838	1.6275
Square	1.3887	1.7637
Arc 0.25	1.2514	1.4265
Arc 0.50	1.2848	1.6355

4.2.5 Studies on Particle Deposition

A total of 12 spacer designs from the modifications of circular, triangular and square shape were investigated in this work to study their effect on particle deposition. From this study, six of them that have better performance in terms of lesser particle deposition, higher mass transfer and lower power consumption were compared and discussed below.

Figure 4.37 shows the particle trajectory for particles injected at different channel height. The *Y*-axis in the figure is the normalised channel height given as the distance from the bottom membrane over the channel height and the *X*-axis is the distance from the channel inlet. The movement of particle is mainly governed by normal drag force towards the membrane surfaces. Initially, particles moved along the field line until they encountered the spacers or membrane surfaces

(deposited). For particles injected at Y = 0.3 mm and below, it can be clearly seen that the shapes of the spacer significantly affected the trajectories of the particles and also the positions where the particles deposited on the bottom membrane surface (at Y = 0 mm). On the other hand, the particles injected at Y = 0.65 mm and above, the trajectories of the particles in the channel with various spacers were almost similar and the positions where the particles deposited on the top membrane surface (at Y = 1.0 mm) were the same (Figure 4.38 (a)). This is due to the absence of spacers at the top membrane to considerably affect the particle trajectories. Another observation can be made from Figure 4.37 is that the positions of particle deposited on the bottom membrane were further from the inlet compared to those deposited on the top membrane. This results demonstated that spacer can play a role in reducing fouling condition on membrane.

Figure 4.38 depicts the positions of particles injected at different channel height deposited on the top and bottom membrane surfaces. In other words, it shows the distance a particle travelled before it deposited on the membrane. For example in Figure 4.38 (b), particles injected at position Y = 0.05 mm travelled a distance of 8.5, 8.2, 9.0, 8.5 and 8.8 mm before deposited on the bottom membrane for spacer shape of Oval-B tilt, Oval-F tilt, Triangle, Square and Arc 0.50, respectively. An earlier particle deposition is undesirable as this means that the tendency for particles to deposit on the membrane surface is higher. From Figure 4.38 (b), it is obvious that the shape of a spacer can affects particle deposition. Triangle and Square spacers are the best among the spacers, which allowed particles to travel further before deposition, followed by Arc 0.25 and Arc 0.50 spacers.

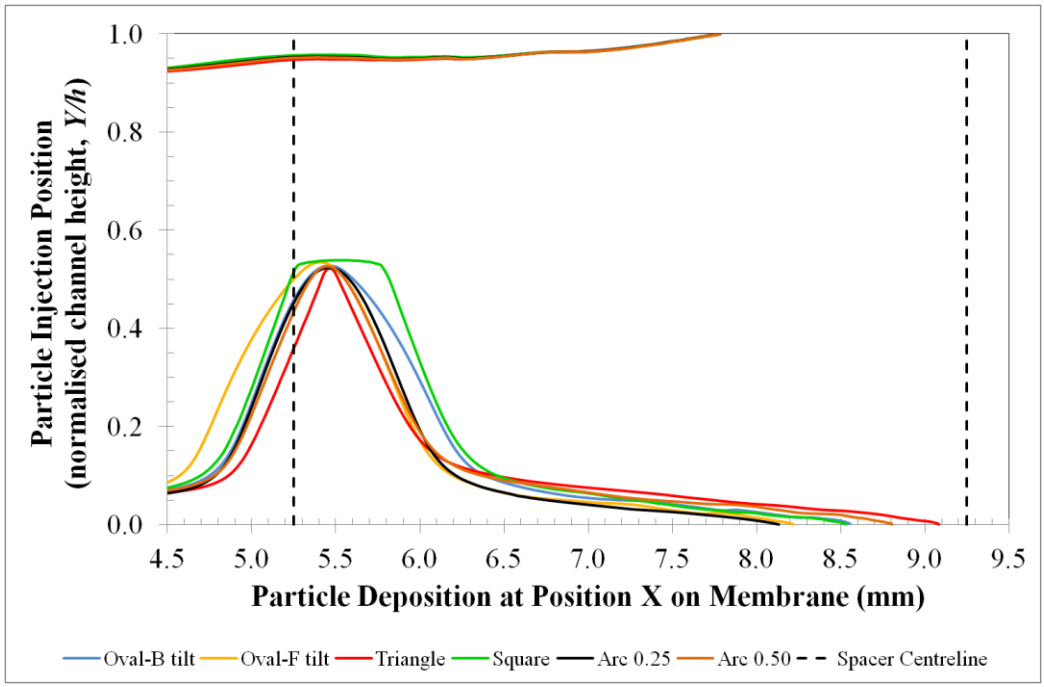

(a)

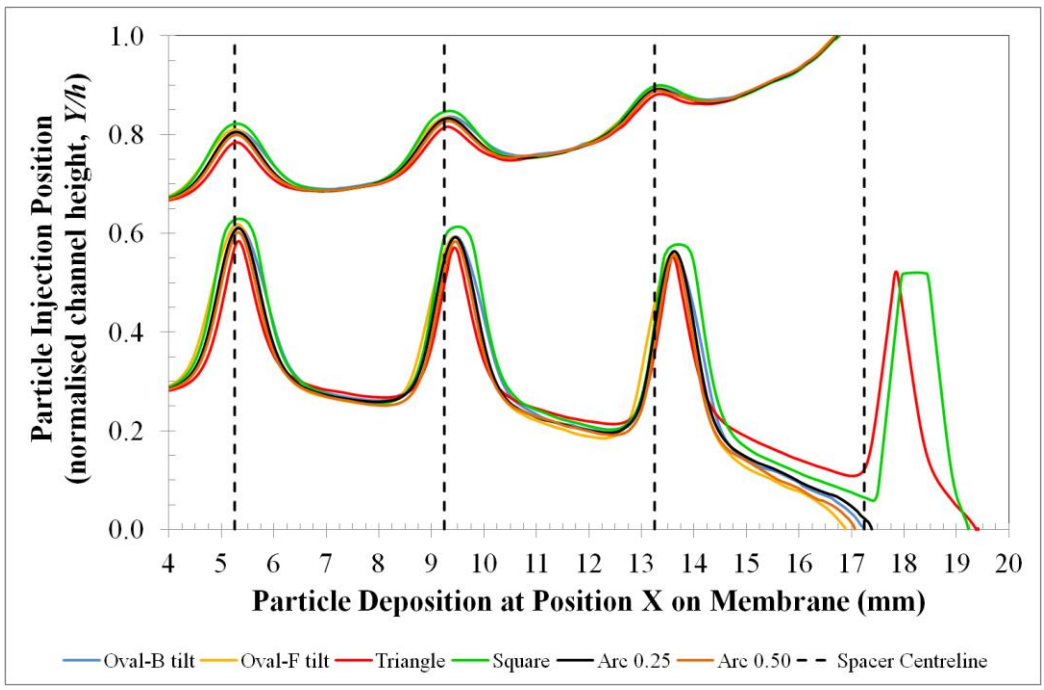

(b)

Figure 4.37: Particle trajectory across channel length for injection positions at (a) top / bottom and (b) middle for selected spacer shapes.

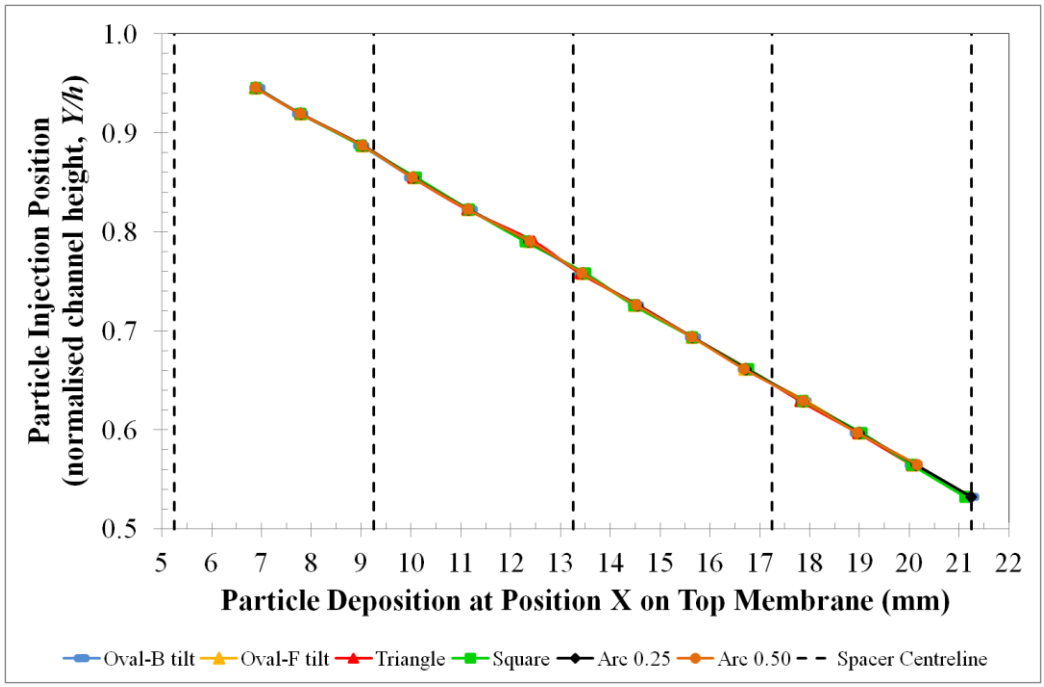

(a)

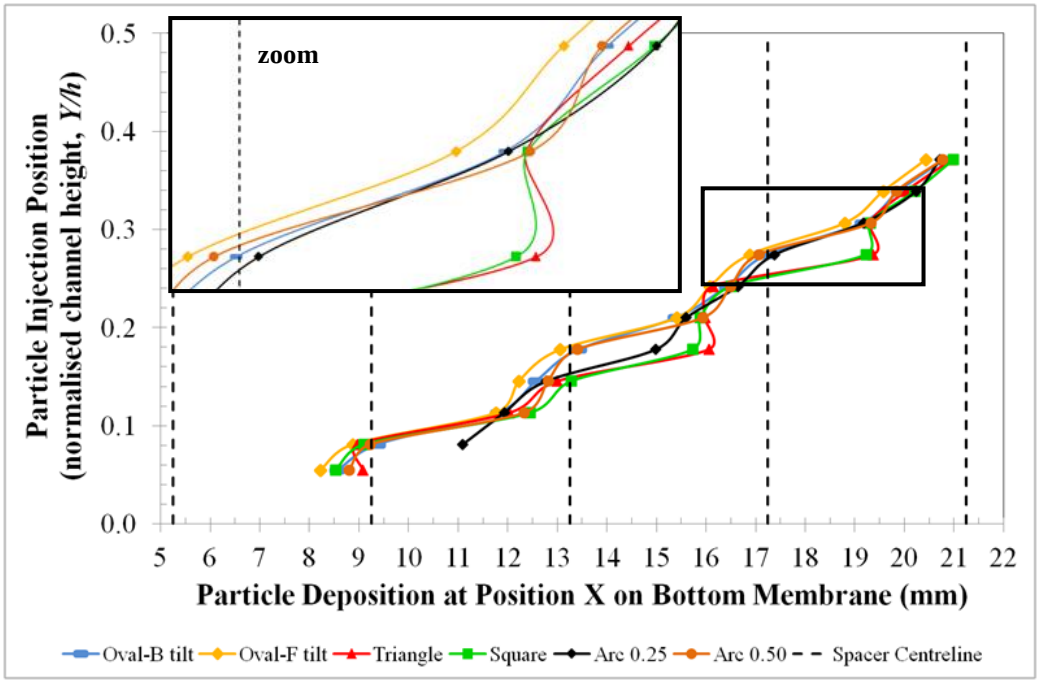

(b)

Figure 4.38: Particle deposition on (a) top and (b) bottom membranes across channel length for selected spacer shapes.

4.3 3D Simulations

The focus of 3D simulation was to investigate the effect of spacer orientation relative to the bulk flow in a membrane channel, i.e. the flow attack angle of the spacers (Figure 3.3) on fluid hydrodynamics, concentration polarisation and particle deposition. Spacers that provided the best balance between higher mass transfer, lesser particle deposition and lower power consumption as determined in the 2D simulations, namely the Square spacer and its modification spacers (Arc 0.25 and Arc 0.50 spacers), were used in the 3D simulations.

4.3.1 Flow Patterns across Channel Length

Four flow attack angle (α = 90°, 15°, 30° and 45°) were simulated with three different types of spacers (Square, Arc 0.25 and Arc 0.50) to investigate the effect of flow attack angle and spacer shape on the flow patterns across the channel, as presented in Figures 4.39 – 4.41.

These figures illustrate how the flow direction changed over the spacers with different flow attack angle. For α = 90°, the flow direction mainly followed the top spacers orientation with minimum vortices created. There are no major changes in the flow directions across the channel. Some of the flow streamlines near the bottom of the channel were terminated as they encountered the bottom spacers. When the flow attack angle is small, i.e. less than 30°, the flow direction at the top section of the channel mostly follows the top spacers' orientation. For α

= 15°, the flow direction near the bottom wall started to change at the location of the top spacers. As the flow attack angle increases, the changes in flow direction became more obvious. There is a 45° change in the flow direction when the flow encountered the intersections of top and bottom spacers as the flow tried to align itself along the main flow direction. Vortices also started to appear at these intersections.

Comparing Figure 4.40 with Figure 4.39 and Figure 4.41 found that the flow pattern for Arc 0.25 spacers was smoother compared to square and Arc 0.50 spacers, which were more chaotic. The chaotic nature of the flows was especially obvious when the flow attack angle is 15°. Overall, the simulation results indicated that at relatively small Reynolds number (less than 180 in this simulation) the flow is steady, which are in line with the findings of Bucs et al. (2015).

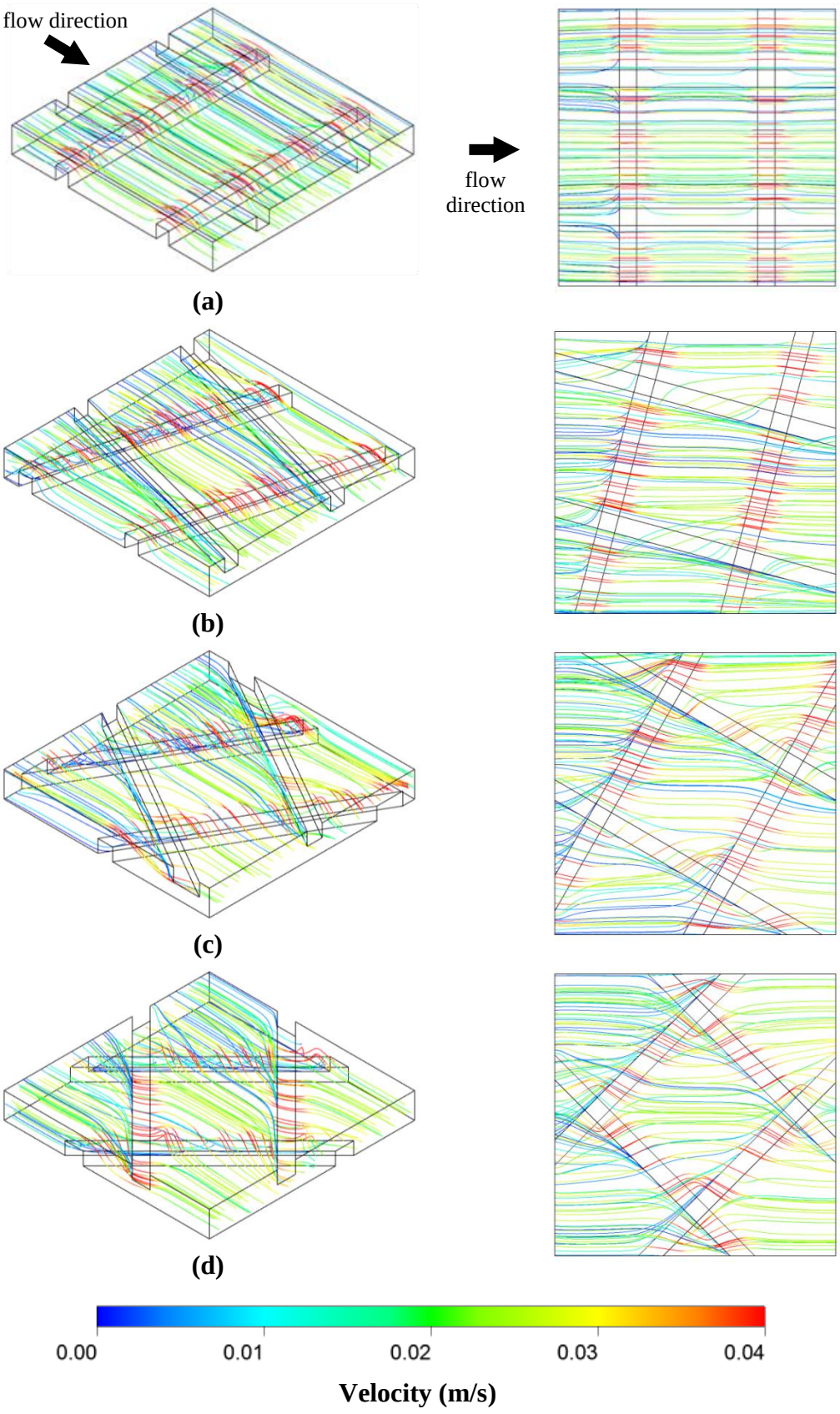

Figure 4.39: Flow pattern across channel length for Square spacer with flow attack angle of (a) 90°, (b) 15°, (c) 30° and (d) 45°. Left: 3D view, Right: Top view. The flow velocity magnitude is represented by the colour scale of a streamline.

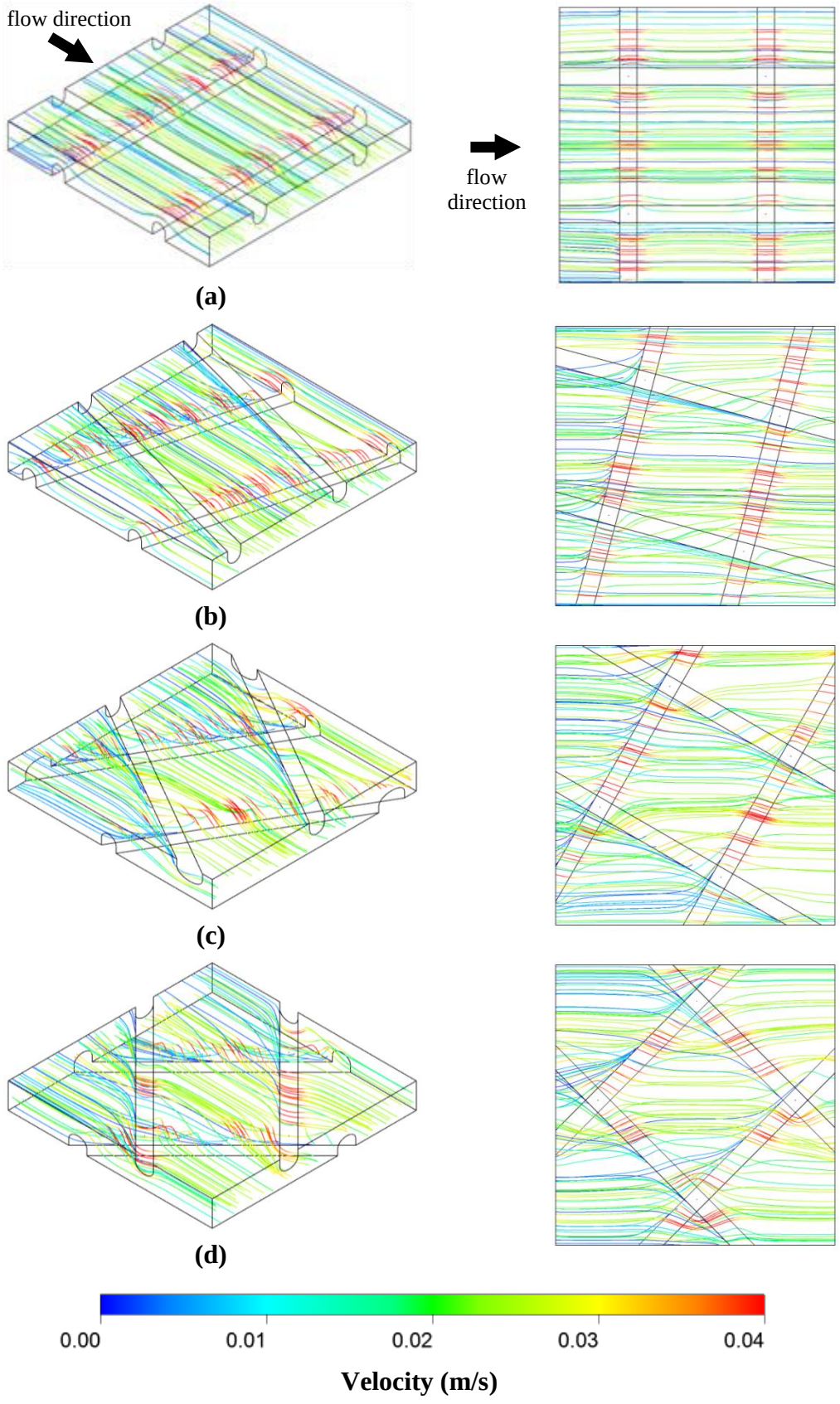

Figure 4.40: Flow pattern across channel length for Arc 0.25 spacer with flow attack angle of (a) 90°, (b) 15°, (c) 30° and (d) 45°. Left: 3D view, Right: Top view. The flow velocity magnitude is represented by the colour scale of a streamline.

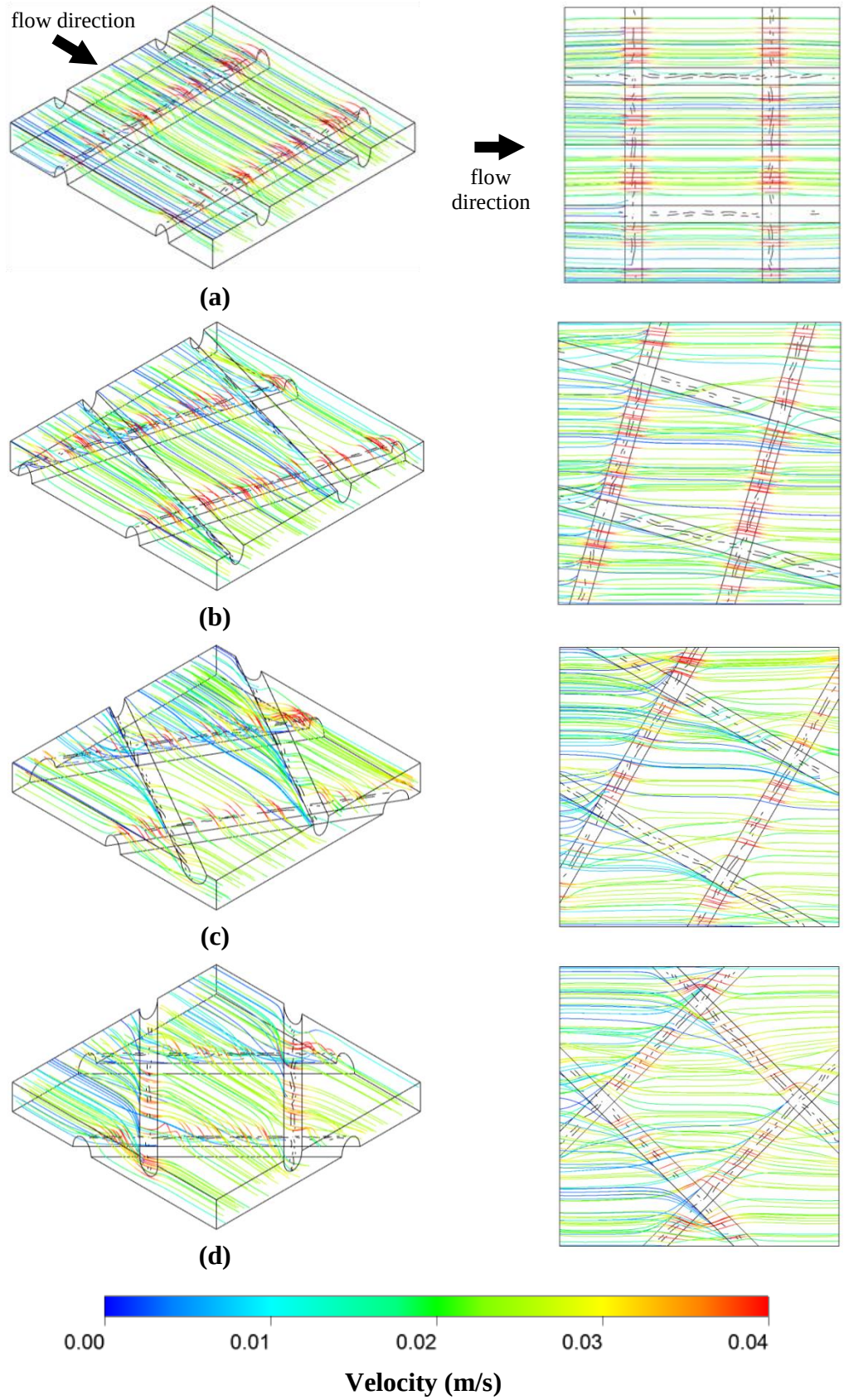

Figure 4.41: Flow pattern across channel length for Arc 0.50 spacer with flow attack angle of (a) 90°, (b) 15°, (c) 30° and (d) 45°. Left: 3D view, Right: Top view. The flow velocity magnitude is represented by the colour scale of a streamline.

4.3.2 Velocity Profiles across Channel Length

Figures 4.42 – 4.44 present the velocity vectors and contours for various shape of spacers with four different flow attack angles. The diagrams on the left of these figures show that in general the bulk flow velocity increased when passed across spacers. The velocities are higher when the flow attack angle is smaller, and when the angle is 90°. For smaller flow attack angle and α = 90°, since there are no major changes in the flow direction, the flows are not interrupted when passing across spacers. This allowed a higher increase in velocity as the flow passes through the narrow gap between spacers and membrane. For spacers with flow attack angle of 30° and 45°, the increase in velocity across the spacers is lesser compared to α = 15° and 90°. The flow tends to realign itself with the main flow direction after the spacers causing major changes in flow direction and hence lesser increase in velocity.

Comparing the 3D velocity vector profiles of different spacer shapes indicated that in general Arc 0.50 spacer has a lower velocity profile. The density of higher velocity across the spacer also is lower compared to Square and Arc 0.25 shape.

The diagrams on the right of Figures 4.42 – 4.44 show the velocity contour near to the top membrane surface. The velocity near to the top membrane surface at the location of bottom spacers was the highest for α = 15°, and the velocity decreases as the flow attack angle increases, which is inline with the trend of the bulk flow velocity. When the flow attack angle is 45°, the flow is not

parallel with the spacers and as the flow passes across the spacers, it tries to align itself with the bulk flow direction causing major changes in its direction and hence lesser acceleration.

The velocity across the bottom spacers is the highest for Square spacer due to the geometry of the Square spacer which has sharp edges that can drag and accelerate the flow near to the membrane wall. Arc 0.25 spacer with 45° flow attack angle has the lowest increase in velocity near the top membrane.

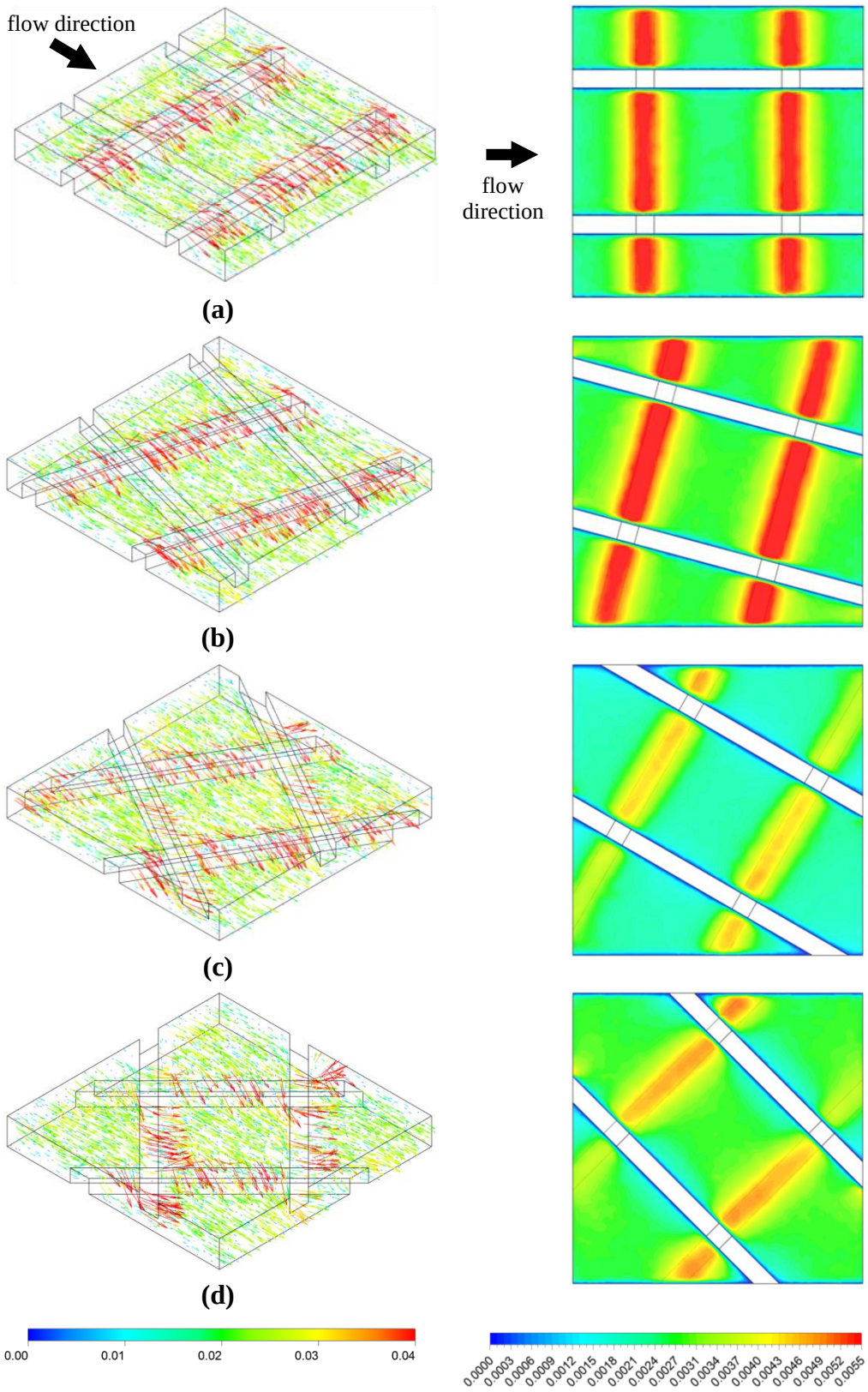

Figure 4.42: Velocity vectors of bulk flow (left) and velocity contour near to the top membrane wall (right) across channel length for Square spacer with flow attack angle of (a) 90°, (b) 15°, (c) 30° and (d) 45°. The flow velocity magnitude is represented by the colour scale.

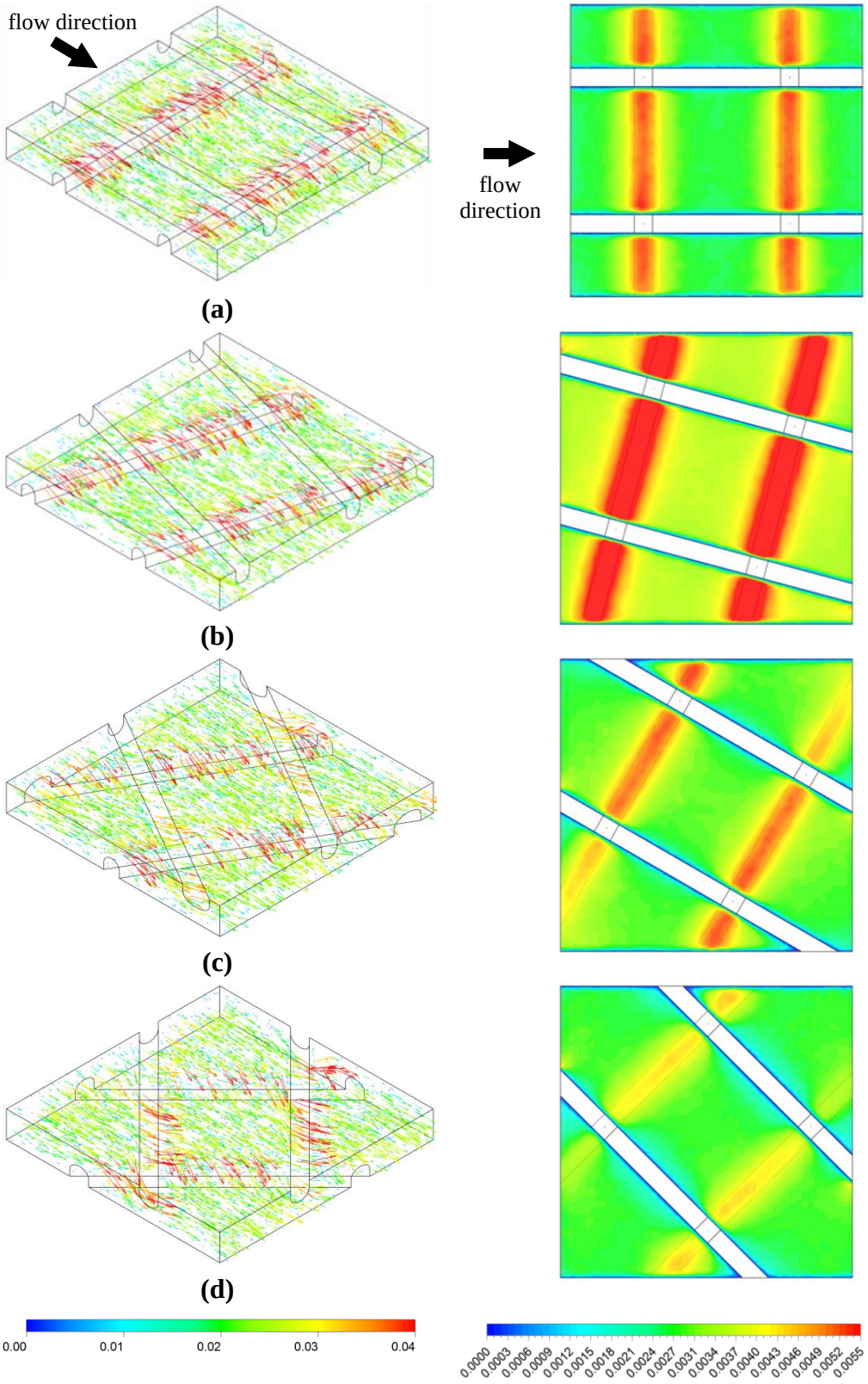

Figure 4.43: Velocity vectors of bulk flow (left) and velocity contour near to the top membrane wall (right) across channel length for Arc 0.25 spacer with flow attack angle of (a) 90°, (b) 15°, (c) 30° and (d) 45°. The flow velocity magnitude is represented by the colour scale.

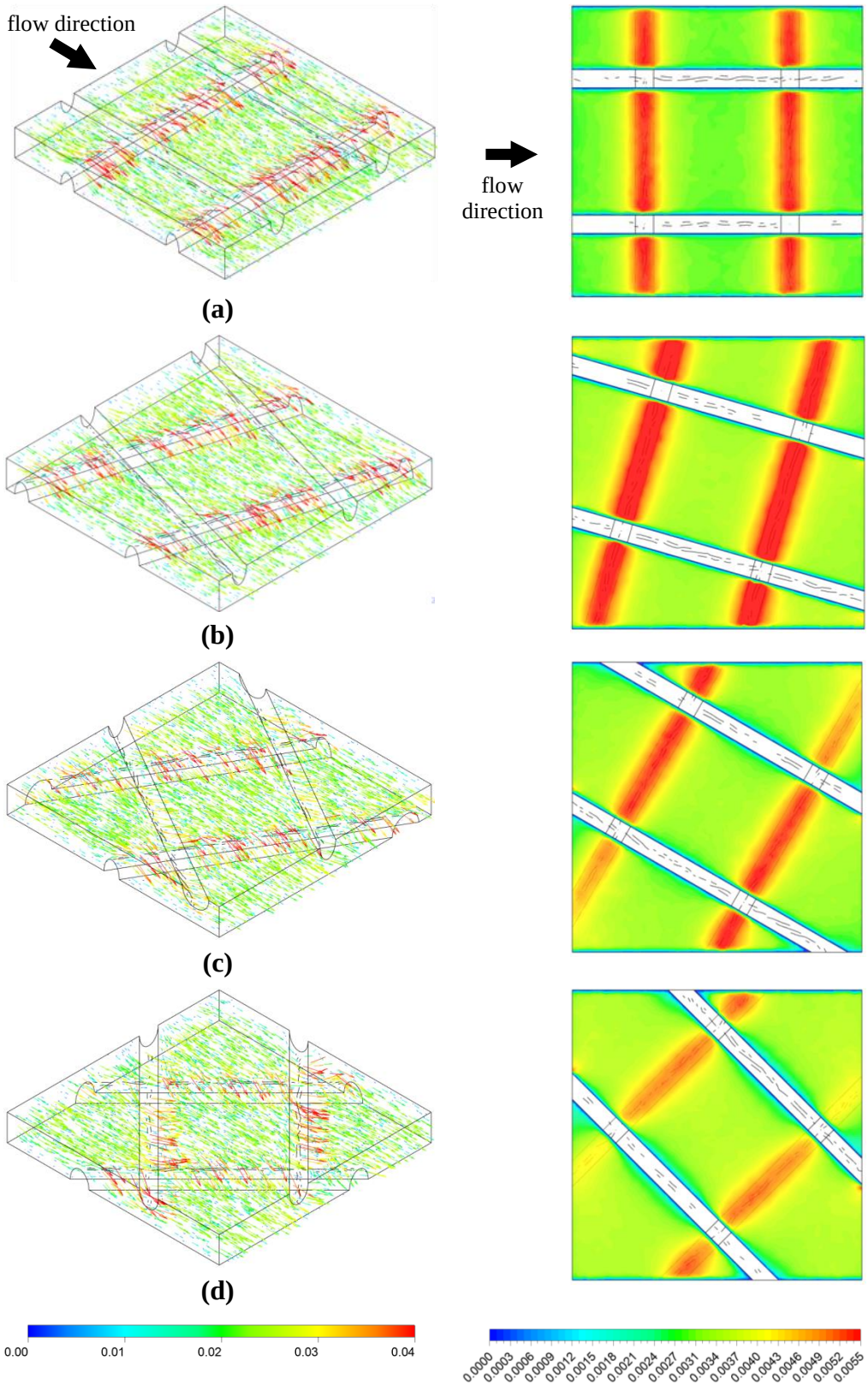

Figure 4.44: Velocity vectors of bulk flow (left) and velocity contour near to the top membrane wall (right) across channel length for Arc 0.50 spacer with flow attack angle of (a) 90°, (b) 15°, (c) 30° and (d) 45°. The flow velocity magnitude is represented by the colour scale.

4.3.3 Spatial Distribution of Wall Shear Stresses on Membrane Surfaces across Channel Length

The distribution pattern of wall shear stress on the top and bottom membrane surfaces for different spacer shapes are presented in Figures 4.45 – 4.47. The wall shear stresses on the top membrane surface increase significantly at the location of bottom spacers. Spacers with flow attack angle of 90° and 15° exhibit the highest wall shear stress on the top membrane surface at these locations. At α = 90° and 15°, the bottom spacers were perpendicular or almost perpendicular to the bulk flow direction and when the flow encounters the bottom spacers, it was forced harder through the narrow gap between the spacers and the top membrane causing higher increase in velocity, and consequently higher increase in wall shear stress on the top membrane.

For the arc shaped spacers, as the flow attack angle increases from 15° to 45°, the wall shear stress on the top membrane near the bottom spacers reduces. The lower wall shear stress on the top membrane as the flow attack angle increases are caused by the change in the flow path which allows milder flow, and thus lower shear stress, across the bottom spacers. However, for Square spacer, the wall shear stress is highest when the flow attack angle is 90° and 15°, followed by 45° and 30°. The trend for Square spacer is different from the arc shaped spacers could be caused by the geometry of square shaped spacers in which the sharp edges could drag and accelerate the flow near to the membrane wall (Figure 4.42), which in turn will increase the wall shear stress.

At the bottom membrane surface, the wall shear stresses are the lowest just before and after the bottom spacers. For channel with flow attack angle of 90°, the areas for zero or low wall shear stress are rather extensive and these areas are prone to become stagnant zones whereby the velocities are also the lowest here. These areas are favourable for the undesirable phenomena of fouling and concentration polarisation and should be avoided. When the flow attack angle is 90°, the wall shear stresses on the bottom membrane surface at the location of the top spacers also exhibited the lowest values. This is because the top spacers were parallel to the main flow direction, and the flow just followed the top spacer orientation without causing much disruption to the flow, and thus prevented the acceleration of flow which will result in higher shear stress.

When the flow attack angle increases from 15° to 45°, the wall shear stresses on the bottom membrane surface at the location of the top spacers increases. The top spacer orientation became more and more perpendicular to the bulk flow direction as the flow attack angle increases, and became an obstacle for the flow. This situation forced the flow through the narrower gap between the spacer and the membrane, accelerating the flow in the process that resulted in higher wall shear stress.

Figures 4.45 – 4.47 also imply that the overall spatial distribution of wall shear stress on the top and bottom membranes for different flow attack angles depends on the spacer shapes. For Square spacer, flow attack angle of 45° and 30° exhibit the highest and lowest overall wall shear stresses on the membrane surfaces, respectively. For Arc 0.25 spacer, flow attack angle of 15° and 90° yield

the highest and lowest overall wall shear stresses, respectively. The trend for the highest and lowest wall shear stress for Arc 0.50 spacer is the same as Arc 0.25 spacer. The different trend between the square shaped and arc shaped spacers might be due to the sharp edges that exist in Square spacer.

Comparing the spatial distribution of wall shear stresses on membrane surfaces for the various spacer shapes (Figures 4.45 – 4.47) showed that Arc 0.50 spacer exhibit highest wall shear stresses on the membrane surfaces. This may implied that spacers with sharp edges might not be an optimum spacer design due to the lower overall wall shear stress. Spacer with smooth edges (Arc 0.50 shape) which can yield higher overall wall shear stress is a better design.

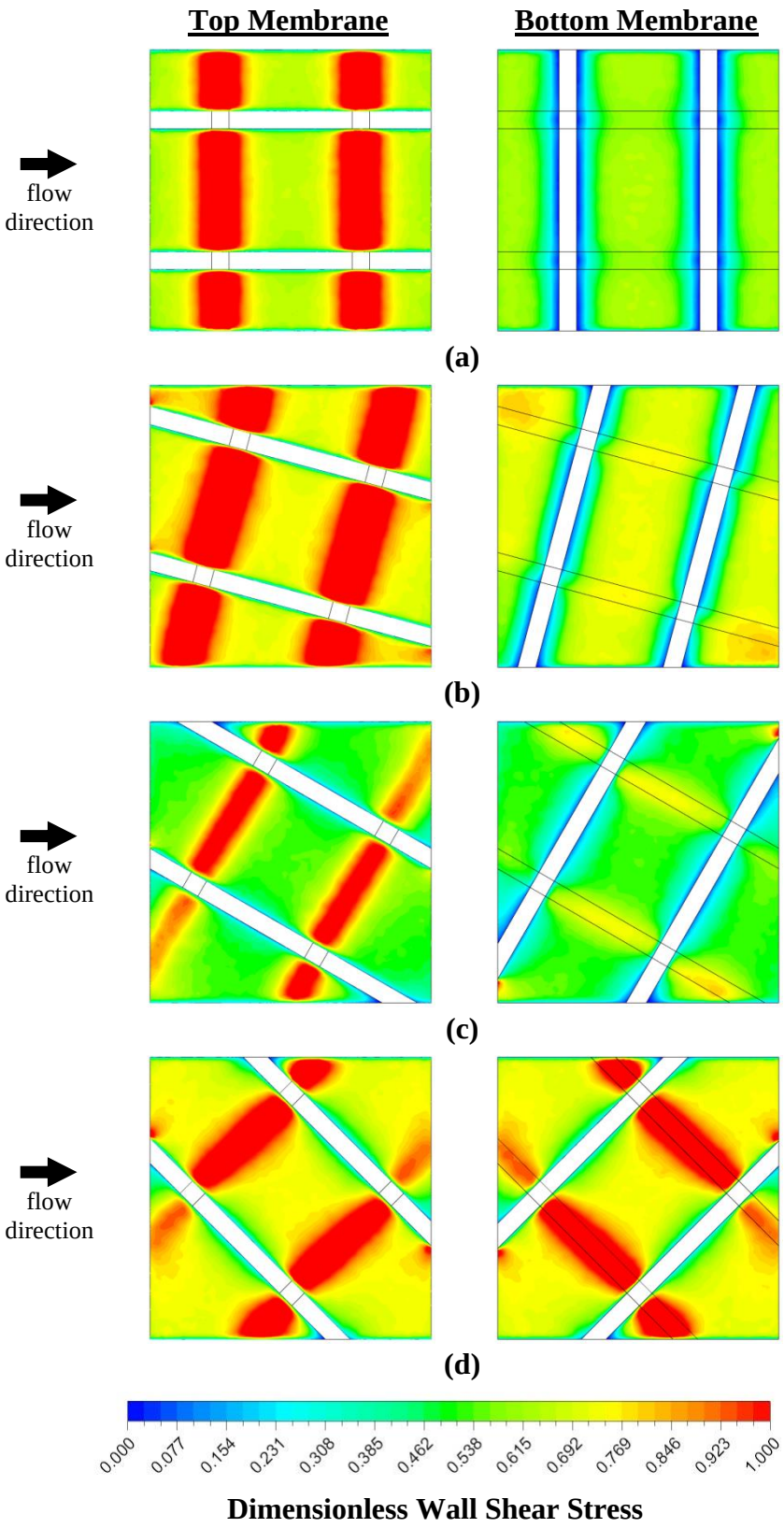

Figure 4.45: Spatial distribution of wall shear stresses on top and bottom membrane surfaces across channel length for Square spacer with flow attack angle of (a) 90°, (b) 15°, (c) 30° and (d) 45°.

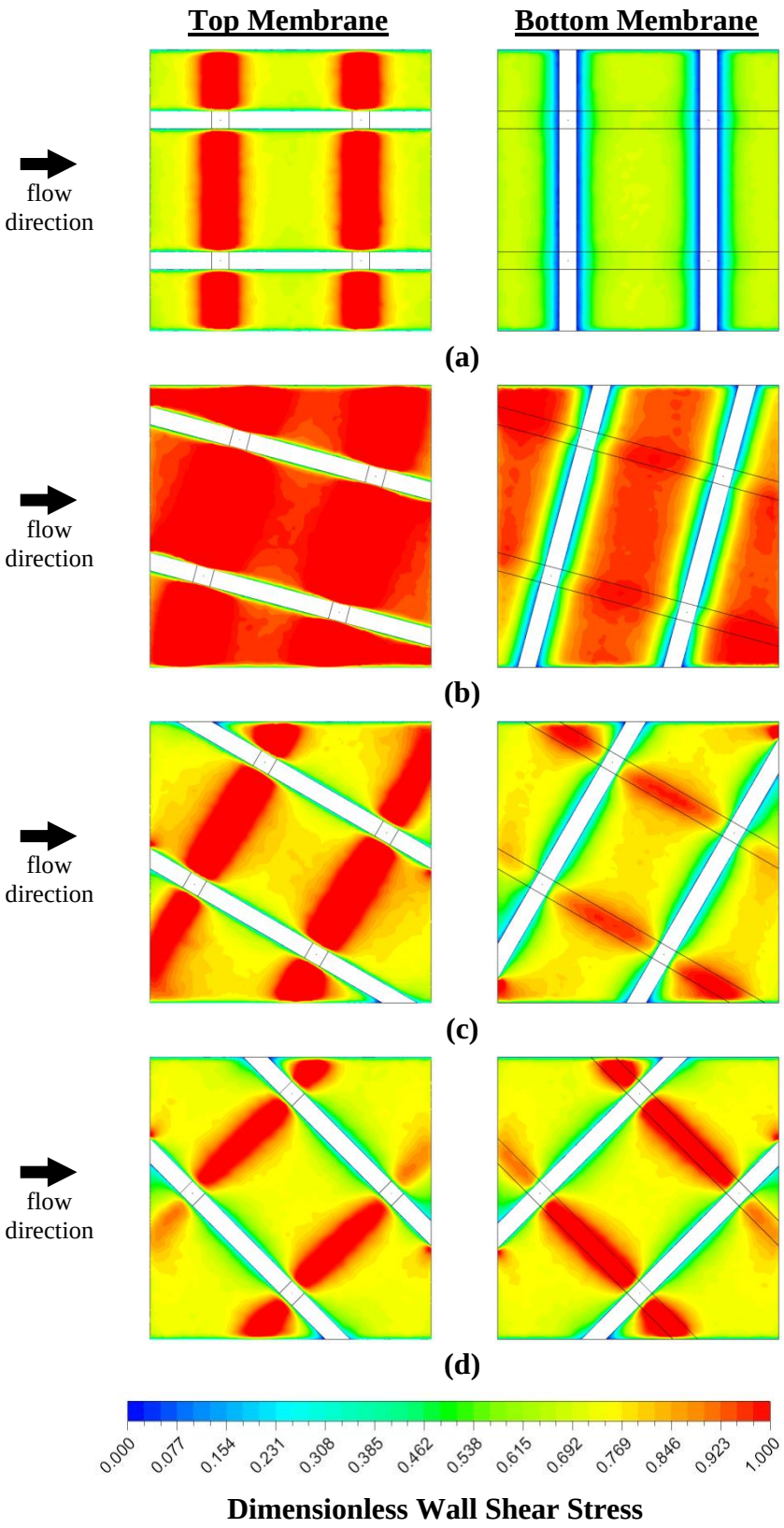

Figure 4.46: Spatial distribution of wall shear stresses on top and bottom membrane surfaces across channel length for Arc 0.25 spacer with flow attack angle of (a) 90°, (b) 15°, (c) 30° and (d) 45°.

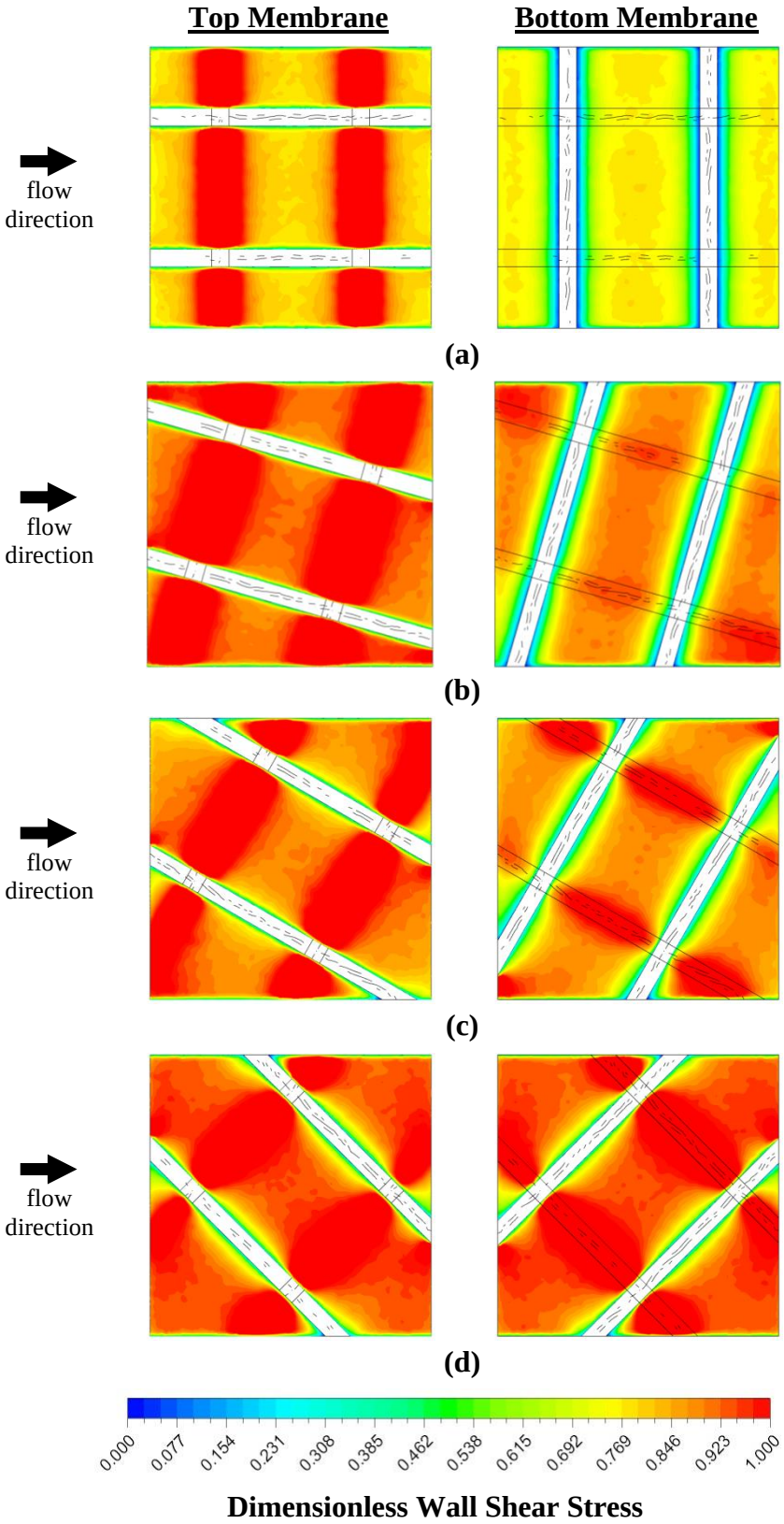

Figure 4.47: Spatial distribution of wall shear stresses on top and bottom membrane surfaces across channel length for Arc 0.50 spacer with flow attack angle of (a) 90°, (b) 15°, (c) 30° and (d) 45°.

Figure 4.48 and Figure 4.49 present the dimensionless wall shear stress at the top membrane for 2D and 3D simulations, respectively. It can be seen that the wall shear stress patterns for 2D simulation were straightforward and repetitive, but they were more complex and non-uniform for 3D simulation; the changes in wall shear stresses for various spacer shapes were different at different location along the channel. For instance, the wall shear stress at the top membrane for Square spacer in 2D simulation was the highest compared to the others and it maintained the same trend throughout the whole channel. However, for 3D simulation, Square spacer resulted in lowest wall shear stress among the three spacer shapes at regions between the spacers, and the highest at the location of the bottom spacer.

In a 2D simulation (*XY* plane), the flow hydrodynamics were only affected by the height of the channel (up-and-down in the *Y*-direction), and along the channel length (left-and-right in the *X*-direction). Given that the spacers in the 2D channel were repetitive, the wall shear stress patterns were also repetitive. The complexity of 3D simulation was due to the additional *Z*-dimension (in-and-out of the *XY* plane) apart from the *X*- and *Y*-dimension. The addition of top spacers along the *Z*-position (which was not included in the 2D simulation) could altered the overall flow hydrodynamics in the channel especially at regions near to the intersection of the top and bottom spacers, and produced different trends between the 2D and 3D simulations. In such situation, the interaction of the flow with the spacer depended strongly on the shape of the spacer, and shape was one of the factors contributing to the changes in flow pattern and subsequently, the wall shear stress and concentration polarisation behaviour.

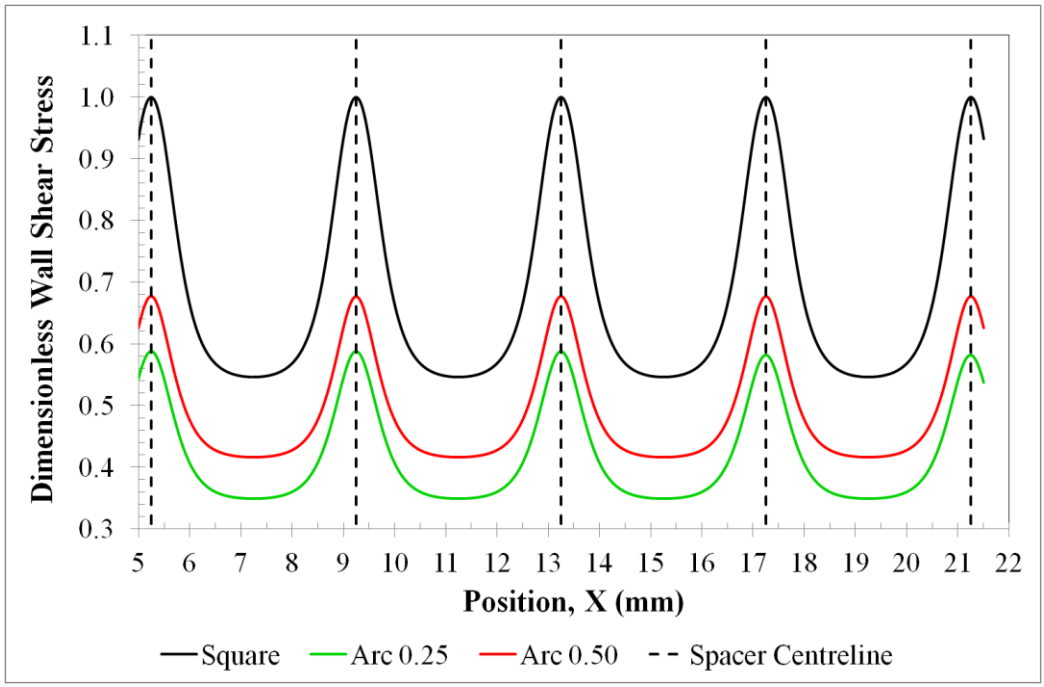

Figure 4.48: Dimensionless wall shear stress at top membrane across channel length for modification of square spacer shapes for 2D simulation

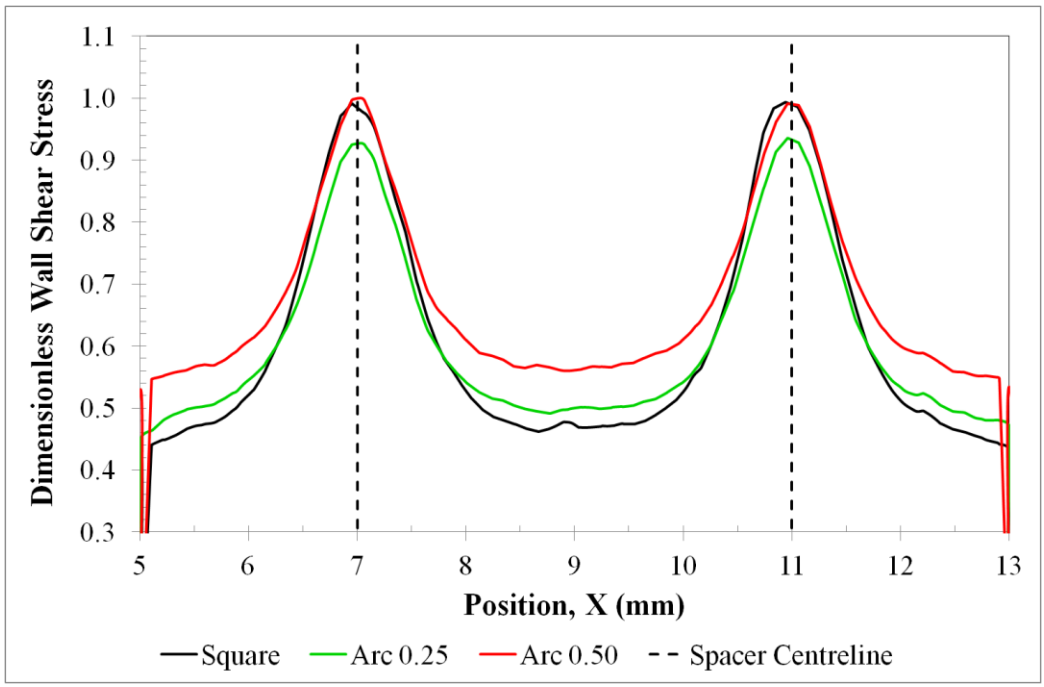

Figure 4.49: Dimensionless wall shear stress at top membrane across channel length for modification of square spacer shapes with flow attack angle of 90° for 3D simulation.

4.3.4 Spatial Distribution of Wall Shear Stresses on Spacer Surfaces

The spatial distribution of wall shear stresses on the spacer surfaces for Square, Arc 0.25 and Arc 0.50 shapes are presented in Figures 4.50 – 4.52, respectively. The edges of the spacer experienced larger wall shear stress compared to the other surfaces, and were the highest when $\alpha = 90°$. At $\alpha = 90°$, the bottom spacers were perpendicular to the main flow direction and the flow was forced harder through the narrow gap between the spacers and the membrane causing higher acceleration and consequently higher increase in wall shear stress. When the flow attack angle increased from 15° to 45°, the wall shear stress reduced at the edges and increased at the intersection of the top and bottom spacers. The areas behind the spacer experienced a lower wall shear stress and were particularly obvious when $\alpha = 45°$.

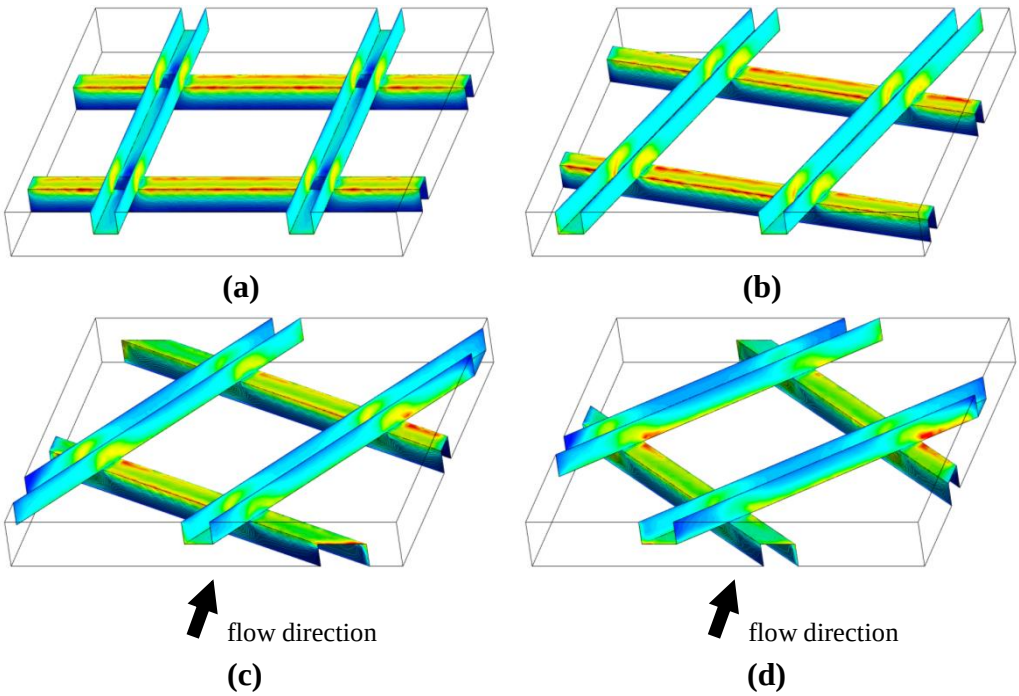

Figure 4.50: Spatial distribution of shear stresses on spacer surfaces for Square spacer with flow attack angle of (a) 90°, (b) 15°, (c) 30° and (d) 45°. Refer to Figure 4.52 for colour-coded legend.

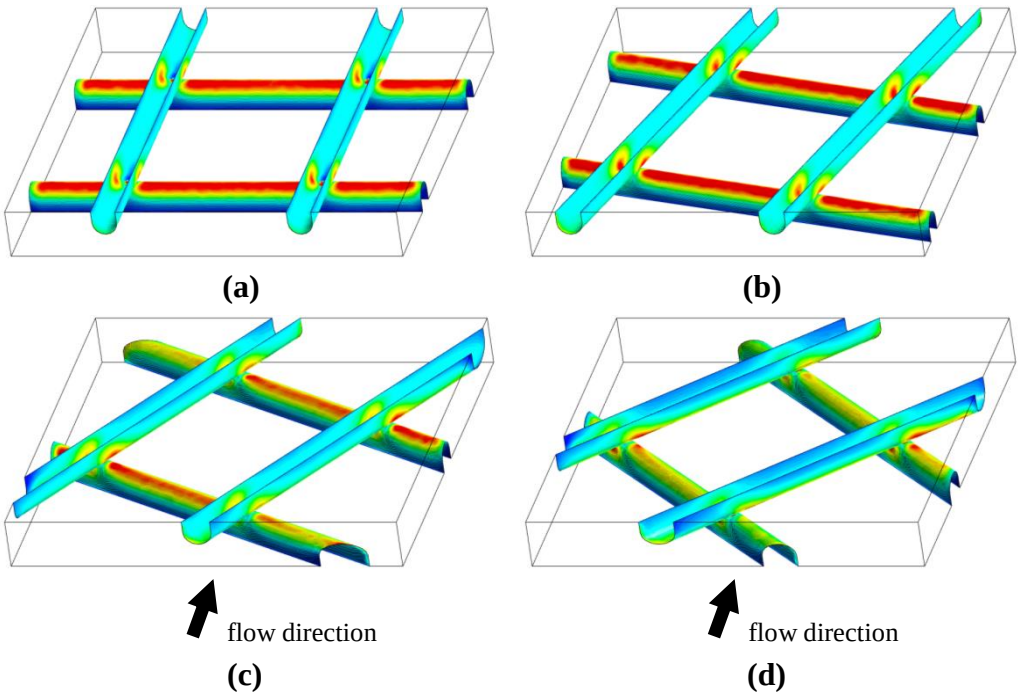

Figure 4.51: Spatial distribution of shear stresses on spacer surfaces for Arc 0.25 spacer with flow attack angle of (a) 90°, (b) 15°, (c) 30° and (d) 45°. Refer to Figure 4.52 for colour-coded legend.

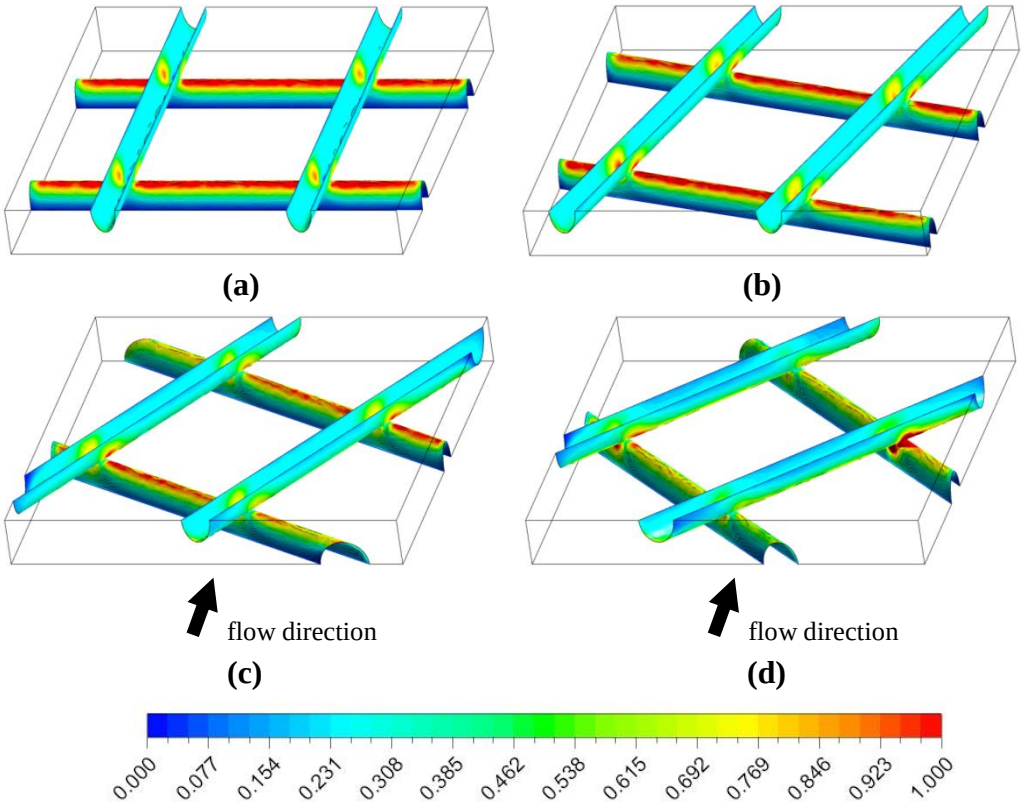

Figure 4.52: Spatial distribution of shear stresses on spacer surfaces for Arc 0.50 spacer with flow attack angle of (a) 90°, (b) 15°, (c) 30° and (d) 45°.

Due to the smoother surface of arc shaped spacers, the spatial distribution of wall shear stresses on the spacer's edges were much more uniform compared to Square spacer. Comparison between Arc 0.25 and Arc 0.50 spacers show that areas with higher wall shear stress were larger for Arc 0.25 spacer due to the smaller curvature of Arc 0.25 spacer.

4.3.5 Concentration Factor on Membrane Surfaces across Channel Length

Figures 4.53 – 4.55 depict the spatial distribution on NaCl concentration factor on the top and bottom membrane surfaces for Square, Arc 0.25 and Arc 0.50 spacers, respectively. The investigations on the effect of flow attack angle on concentration polarisation tendency on the membrane surfaces showed that in general spacers with flow attack angle of 90° has the highest concentration factor on the membrane surfaces. This were followed by spacers with flow attack angle of 15°, and as the angle increased toward 45°, the concentration factor reduced.

On the top membrane surface, the concentration factor is lower at the location where the bottom spacers are located and is higher at the location between the two bottom spacers. The zones where concentration factor is lower coincided with zones with higher wall shear stress (Section 4.3.3), and the zones where concentration factor is higher matched with areas with lower wall shear stress. These findings supported the previous statement that higher wall shear stress is favourable as it can help in reducing concentration polarisation phenomenon.

The concentration factor is lower on the top membrane where the bottom spacers are located shows that the existence of spacers can aid in mitigating concentration polarisation layer on a membrane surface. However, the way how spacers are orientated relative to the bulk flow (the flow attack angle) is important as certain orientation is more favourable to inhibit concentration build-up. When the flow attack angle is 90°, since there are no major changes in the flow path due to the position of the top spacers paralleled with the main flow direction, there is not much disturbance to the flow and hence the concentration is able to build-up in this area. As the flow attack angle increases from 15° to 45°, the flow directions are forced to change as the flow tried to realign itself along the flow path (as discussed in Section 4.3.1 previously). This disturbance is unfavourable for concentration build-up and hence lower concentration factor in this area.

On the bottom membrane surface, it can be observed from Figures 4.53 – 4.55 that the highest concentration factor is located at areas before the spacers. These are stagnant zones where the velocities and wall shear stresses are the lowest. For spacers with α = 90°, the spatial distribution of high concentration factor before and along the bottom spacers are very uniform. The distribution of areas with high concentration becomes patchy as the flow attack angle increases from 15° to 45°. This is again due to the changes in the flow direction when the flow encounters the intersections of top and bottom spacers. Vortices that started to appear at these intersections as mentioned in Section 4.3.1 could be the contributing factor that concentration factor is lower at these areas.

Comparing the spatial distribution of concentration factor on the top and bottom membrane surfaces show that concentration factor is higher at the top membrane for channel with spacers at flow attack angle of 90°, 15° and 30°. The high concentration factor became more evenly distributed between the top and bottom membranes as the flow attack angle increases and were almost symmetry for flow attack angle of 45°. This condition is more favourable as uneven distribution of concentration factor could cause the lifespan of one membrane become shorter than the other, and is forced to replace both although only one is deteriorating and not performing well.

In general, channel with Square spacer exhibits the highest concentration factor followed by Arc 0.25 and Arc 0.50 spacers on both the top and bottom membrane surfaces. The results imply that the sharp edges on a Square spacer compared to the smoother edges of Arc 0.50 spacer do play a role in determining the flow hydrodynamics in a membrane channel and subsequently the way how concentration is able to build-up in a particular area.

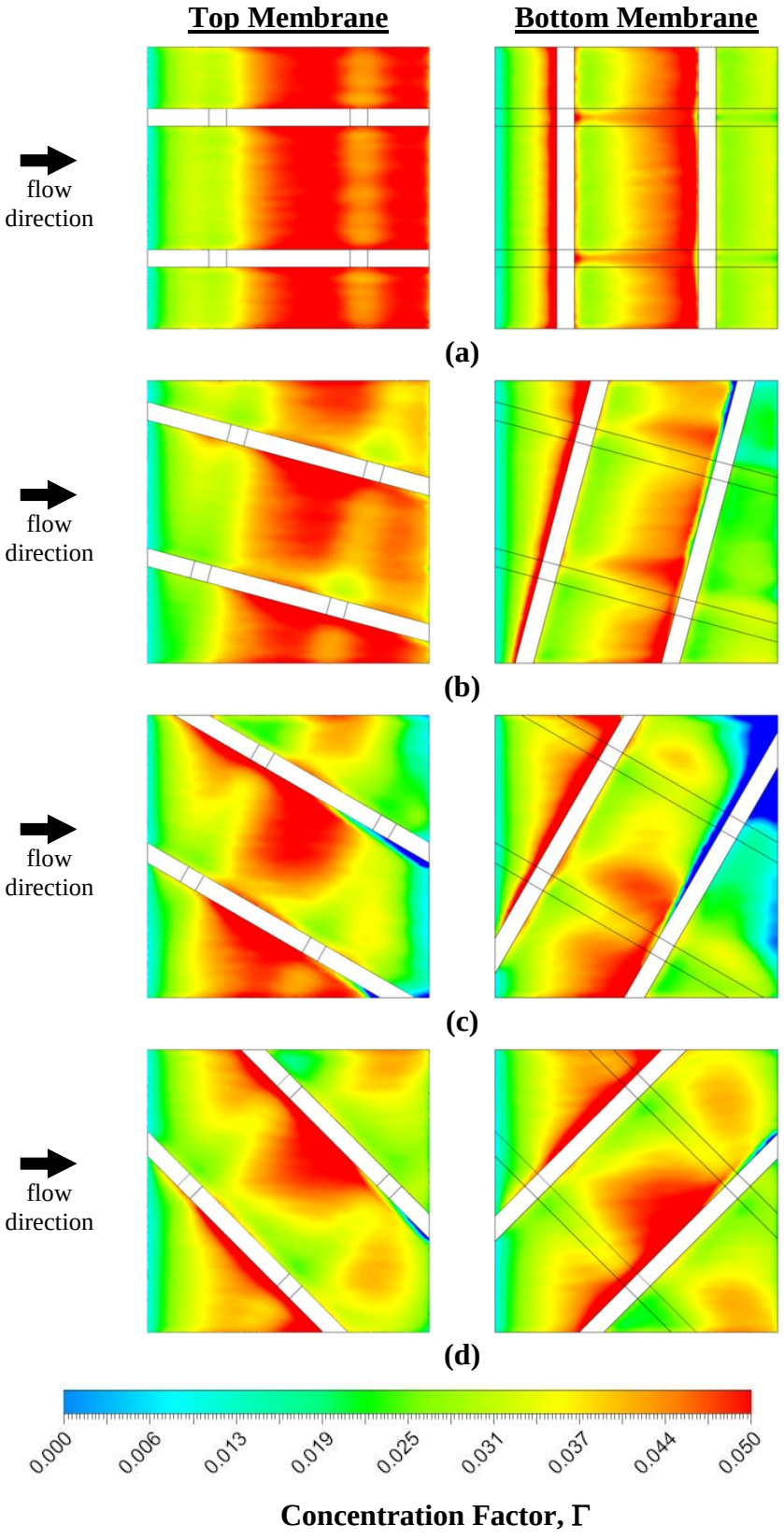

Figure 4.53: Spatial distribution of NaCl concentration factor, Γ on top and bottom membrane surfaces across channel length for Square spacer with flow attack angle of (a) 90°, (b) 15°, (c) 30° and (d) 45°.

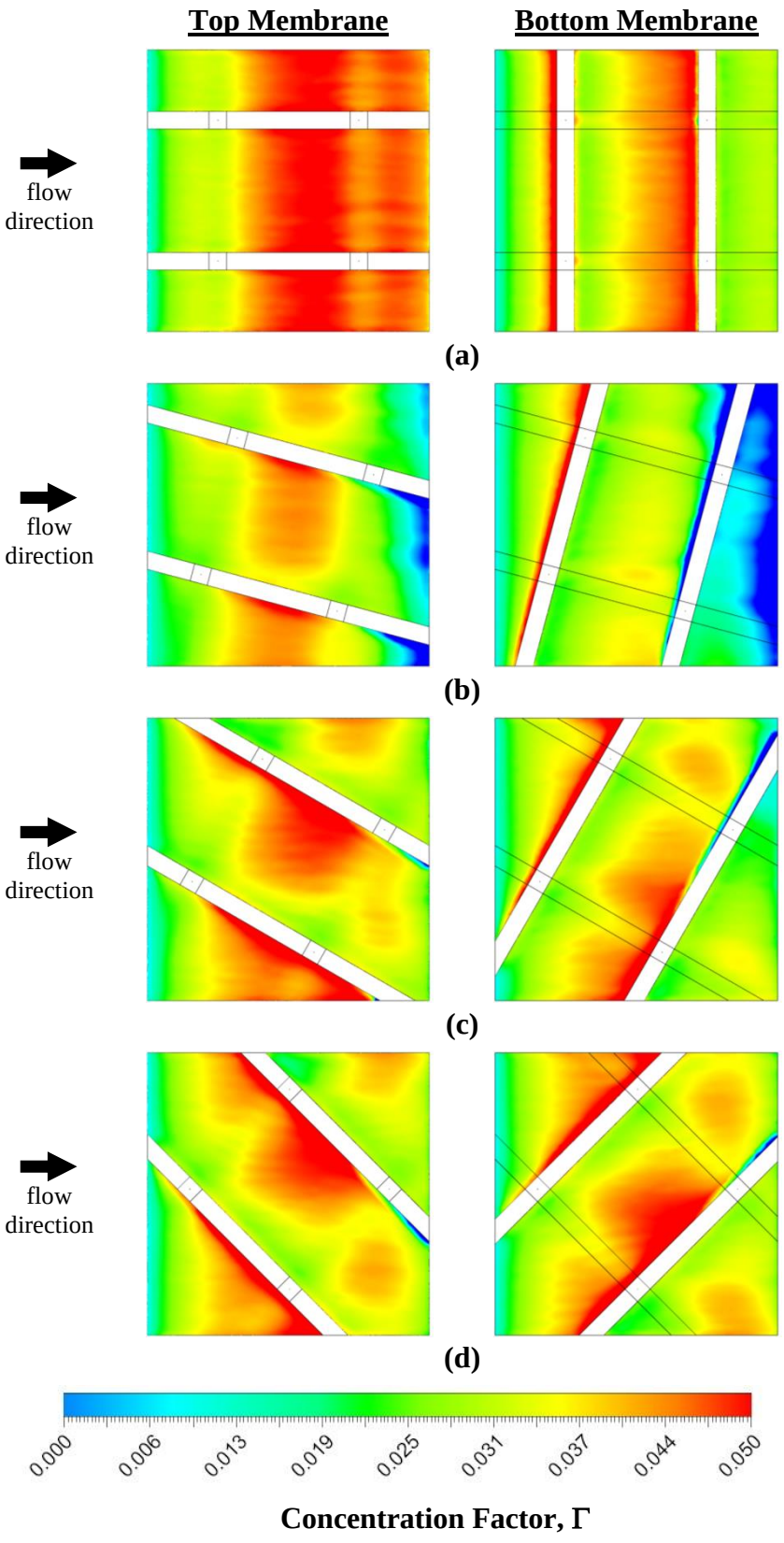

Figure 4.54: Spatial distribution of NaCl concentration factor, Γ on top and bottom membrane surfaces across channel length for Arc 0.25 spacer with flow attack angle of (a) 90°, (b) 15°, (c) 30° and (d) 45°.

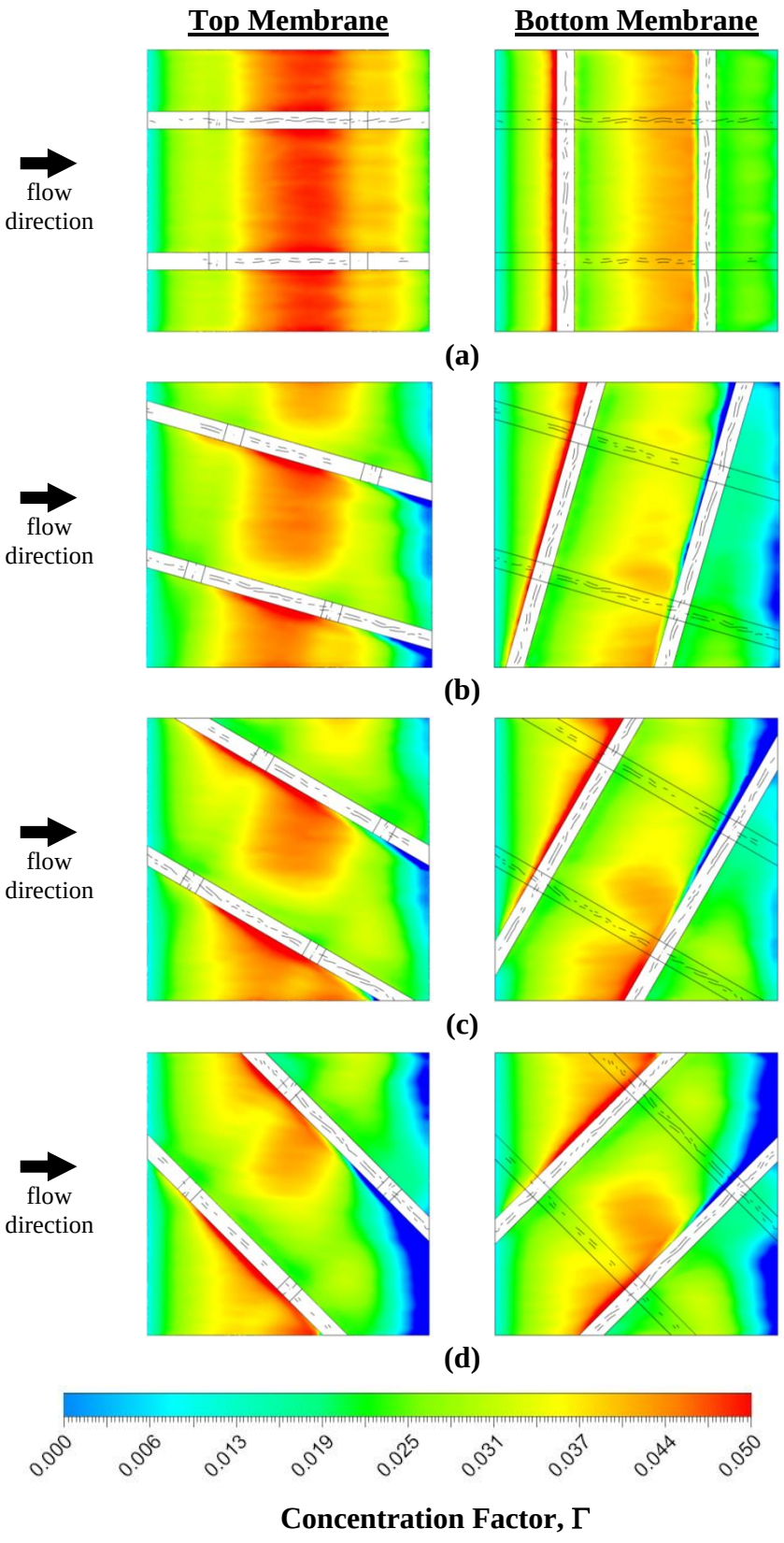

Figure 4.55: Spatial distribution of NaCl concentration factor, Γ on top and bottom membrane surfaces across channel length for Arc 0.50 spacer with flow attack angle of (a) 90°, (b) 15°, (c) 30° and (d) 45°.

4.3.6 Particle Deposition on Membrane Surfaces across Channel Length

The behaviour of particles could be analysed via the interactions of the particles with their surroundings. In present work, particles were subjected to several physical forces such as drag force, Saffman's lift force etc., as mentioned in Section 3.5.1. For instance, a particle nearer to the top membrane would experience a greater magnitude of force acting in the *Y*-direction (towards the top membrane) compared to a particle at the centre of the channel due to the consequence arise from permeation flux. This particle was then more likely to be drawn towards the membrane surface. If the other physical forces acted on this particle yielded a smaller net force in the opposite direction, then the particle would ended up depositing on the membrane surface and vice versa.

The bar charts in Figure 4.56 – 4.58 presented the particles deposition ratios at *Z*-position = 4 mm and along *X*-position at the top and bottom membranes for different spacer shapes and flow attack angles. The insert contours show the spatial distribution of particle deposition and their concentration on the top and bottom membrane surfaces. In general, as shown in the particle distribution contours, the highest particle concentration is located at regions before the bottom spacers on the bottom membrane. These are the areas with lowest velocities and wall shear stresses, and hence this shows that stagnant zones in a channel are favourable for particle deposition and shall have lower fouling resistance. The regions where higher velocity flow prevail and hence with higher wall shear stress (Section 4.3.3), the likelihood for particle deposition becomes lesser. At areas with higher velocity, particle exposure to shear-induced lift force can be greater to the extent that this force surpasses other forces that

acted on the particle which draws the particle in the direction towards the membrane surface, so this condition reduces the interaction of the particle with the membrane surface.

On the other hand, on the top membrane, the highest particle concentration is located at areas between the bottom spacers. Due to the existence of spacers, the cross-sectional area of the channel for fluid to flow was reduced. As the fluid flows through the narrower gap between the spacers and the top membrane, it forces the flow towards the top membrane causing higher tendency for particle to deposit here. The onset of fouling arises from interaction between particle and membrane whereby deposition of particle will be initiated if the particle is brought sufficiently close to the membrane by either the flow itself or due to other physical forces such as gravity.

Referring to the bar charts in Figure 4.56 – 4.58, particle deposition on the membrane surfaces are the highest when the flow attack angle of the spacer is 90°, and are more concentrated in the middle of the channel. Since the position of the top spacers is parallel with the fluid motion for channel with spacer at flow attack angle of 90°, the disturbance to the flow is minimal allowing more concentrated particle deposition at a particular region. When the flow attack angle increases from 15° to 45°, the distributions of particle deposition are more spread out with lower deposition ratios across the channel. Although the particle deposited over a larger area for flow attack angle of 15° to 45°, the lower deposition ratios means that the likelihood for fouling to happen is lower. The results suggested that flow attack angle of 90° is not favourable to mitigate fouling in a membrane channel.

For channel with Square spacer, the distributions of particle deposition between the top and bottom membranes are uneven for α = 90°, with more concentrated fouling area and higher deposition ratio on the top membrane compared to the bottom membrane. This condition is unfavourable as uneven distribution of fouling area could cause uneven lifespan of the membranes, and the whole membrane module is forced to be replaced although only a particular section is deteriorating. Meanwhile, for channel with Arc 0.25 and Arc 0.50 spacers, the distributions of particle deposition between both the membranes are quite uniform regardless of the flow attack angle with roughly the same particle deposition ratios on both the top and bottom surfaces. The different trend between the square shaped and arc shaped spacers at flow attack angle of 90° might be due to the effect of sharp edges that exist in Square spacer that is especially significant when the sharp edges are perpendicular to the motion of flow.

All the three spacers under investigation, i.e. Square, Arc 0.25 and Arc 0.50 spacers, in general show almost the same resistance for particle deposition on the membrane surfaces with Square spacer performed just slightly better than the other two in terms of fouling control.

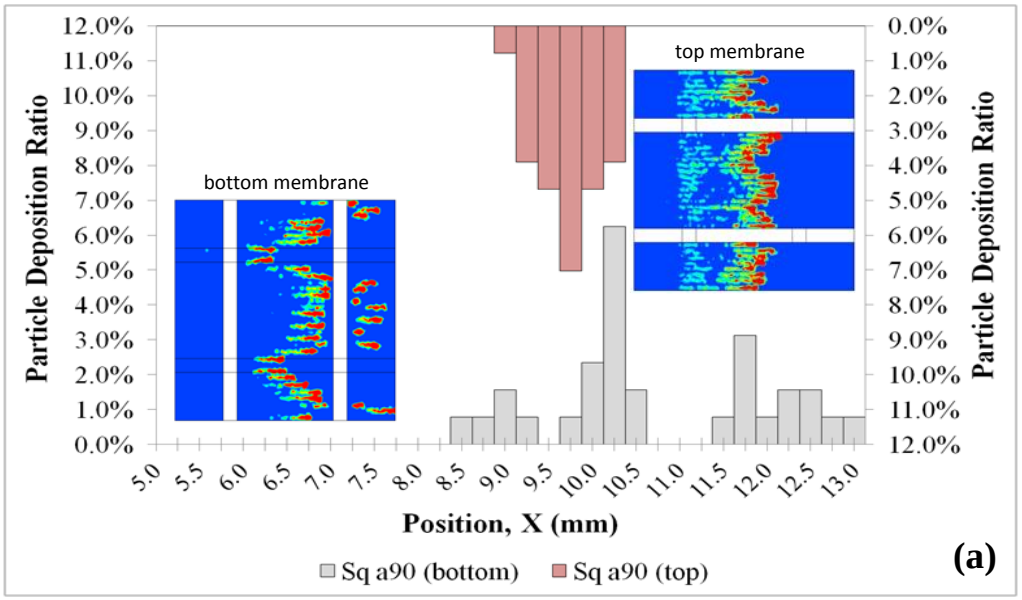
top membrane
bottom membrane
Particle Deposition Ratio
Position, X (mm)
Sq a90 (bottom)
Sq a90 (top)
(a)

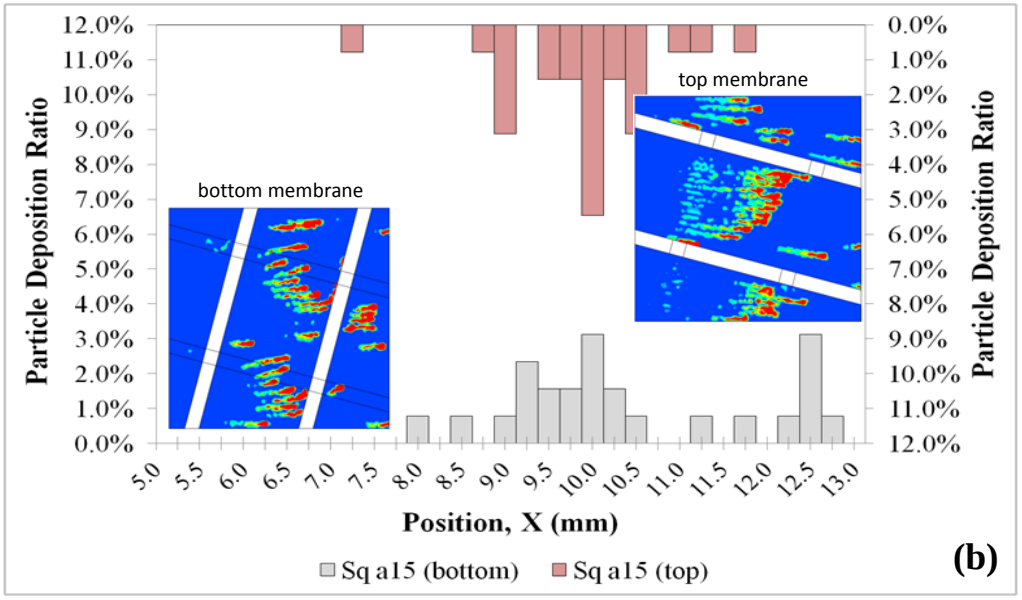
top membrane
bottom membrane
Particle Deposition Ratio
Position, X (mm)
Sq a15 (bottom)
Sq a15 (top)
(b)

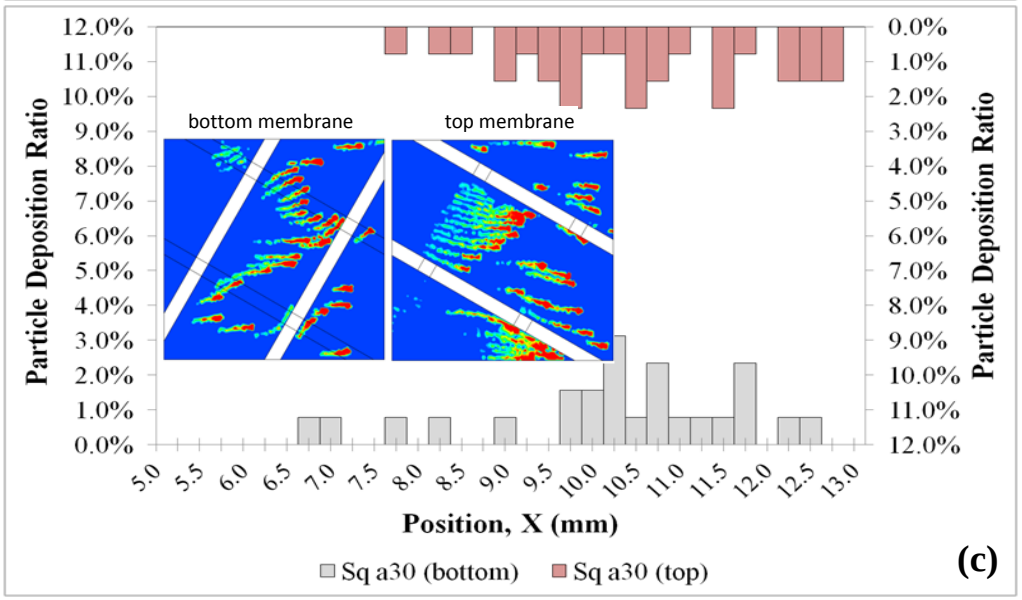
bottom membrane
top membrane
Particle Deposition Ratio
Position, X (mm)
Sq a30 (bottom)
Sq a30 (top)
(c)

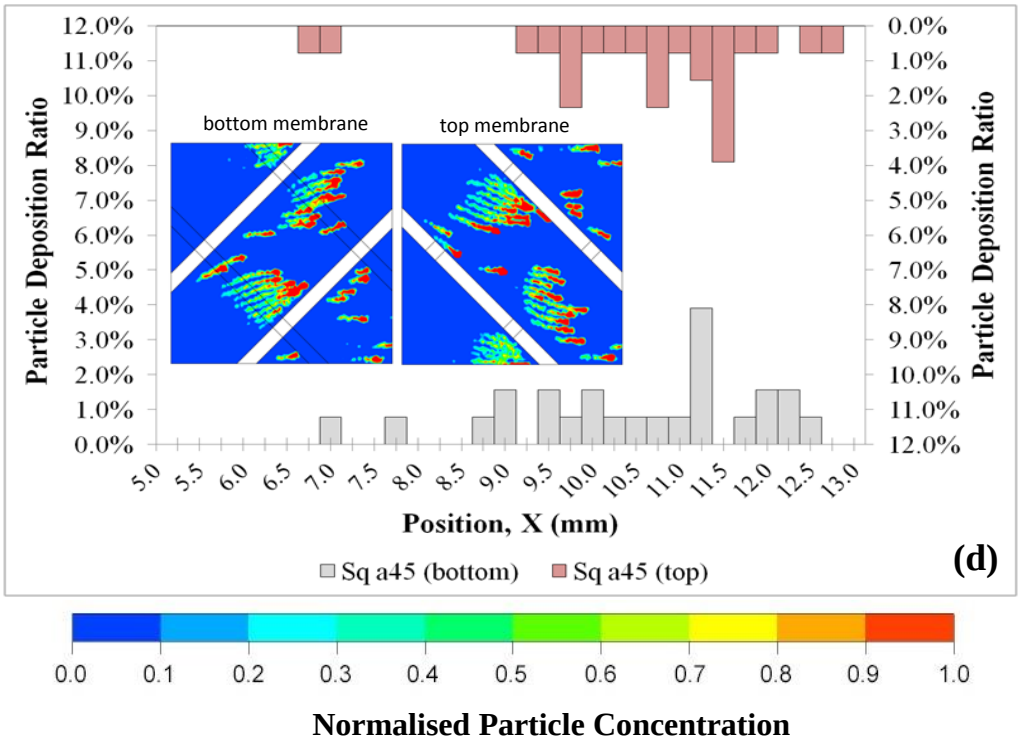

Figure 4.56: Spatial distribution of particles and particle deposition ratios on top and bottom membrane surfaces across channel length for Square spacer with flow attack angle of (a) 90°, (b) 15°, (c) 30° and (d) 45°.

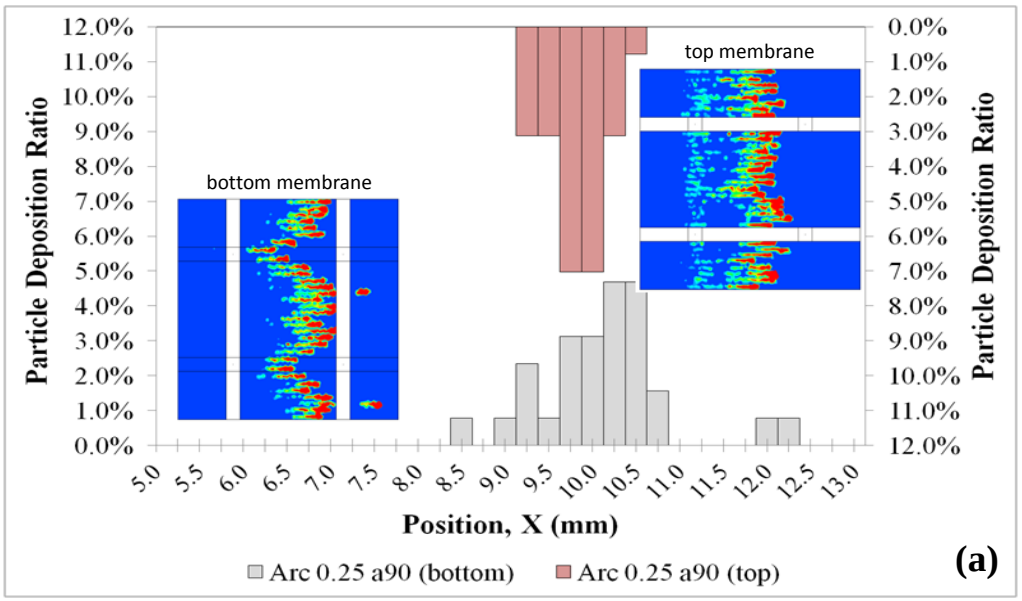

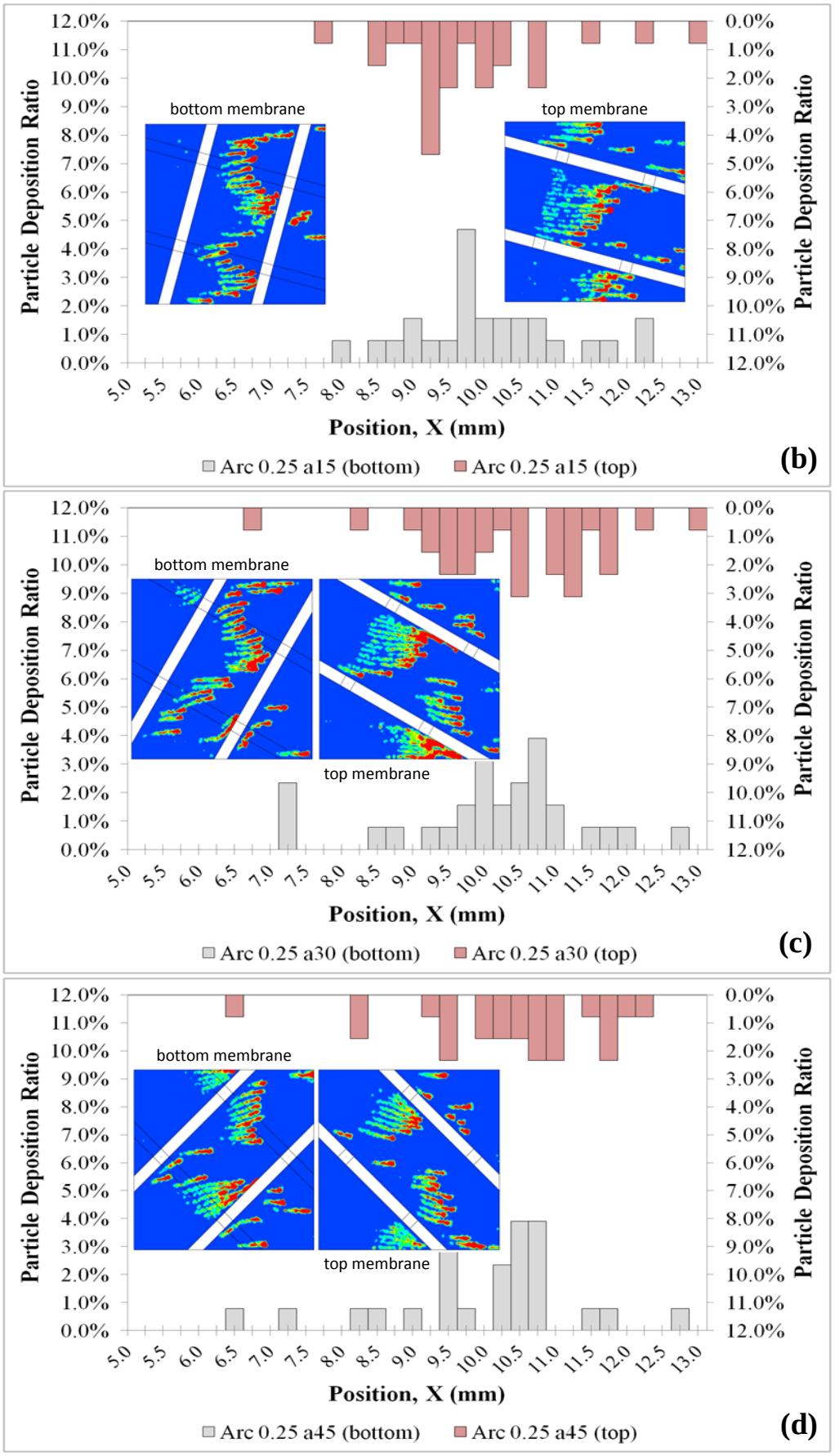

Figure 4.57: Spatial distribution of particles and particle deposition ratios on top and bottom membrane surfaces across channel length for Arc 0.25 spacer with flow attack angle of (a) 90°, (b) 15°, (c) 30° and (d) 45°.

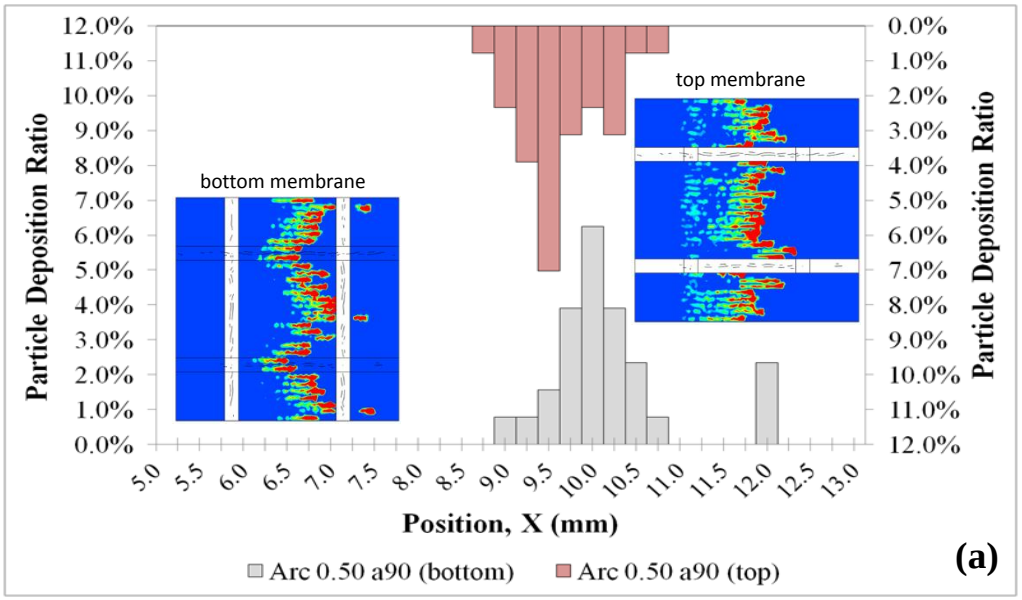
Particle Deposition Ratio
Particle Deposition Ratio
Position, X (mm)
bottom membrane
top membrane
Arc 0.50 a90 (bottom)
Arc 0.50 a90 (top)
(a)

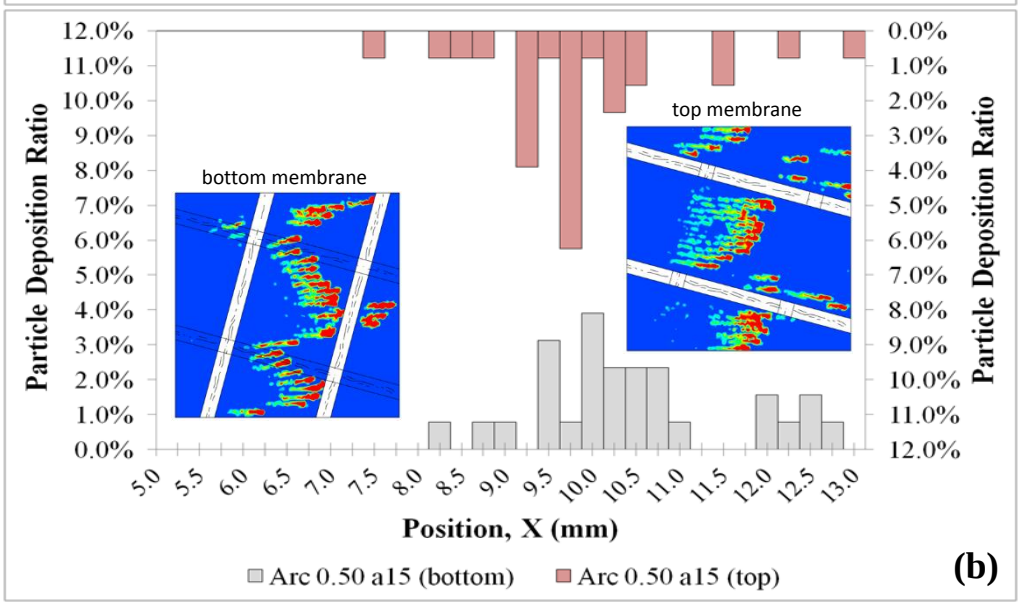
Particle Deposition Ratio
Particle Deposition Ratio
Position, X (mm)
bottom membrane
top membrane
Arc 0.50 a15 (bottom)
Arc 0.50 a15 (top)
(b)

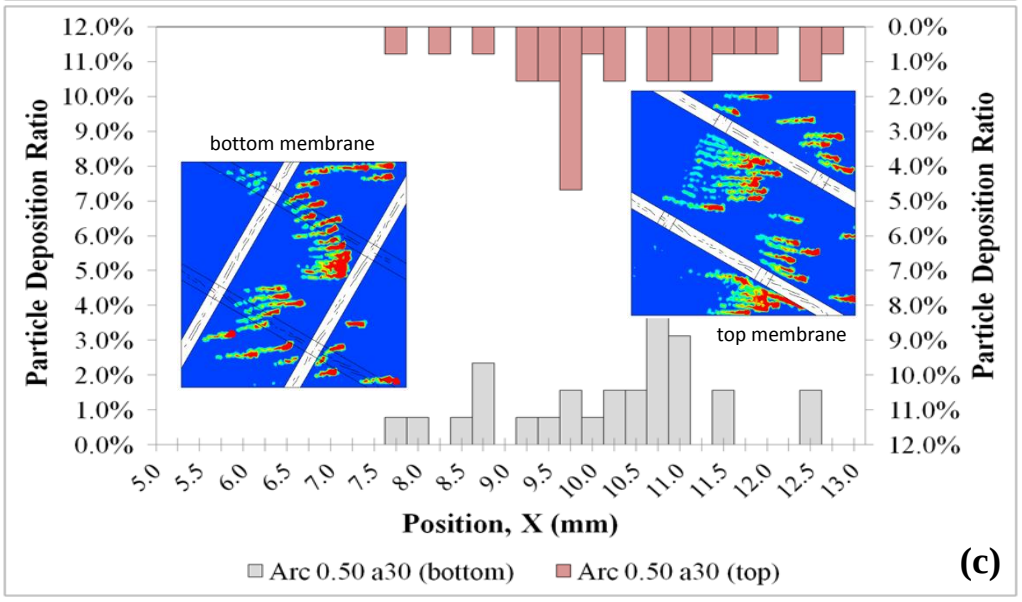
Particle Deposition Ratio
Particle Deposition Ratio
Position, X (mm)
bottom membrane
top membrane
Arc 0.50 a30 (bottom)
Arc 0.50 a30 (top)
(c)

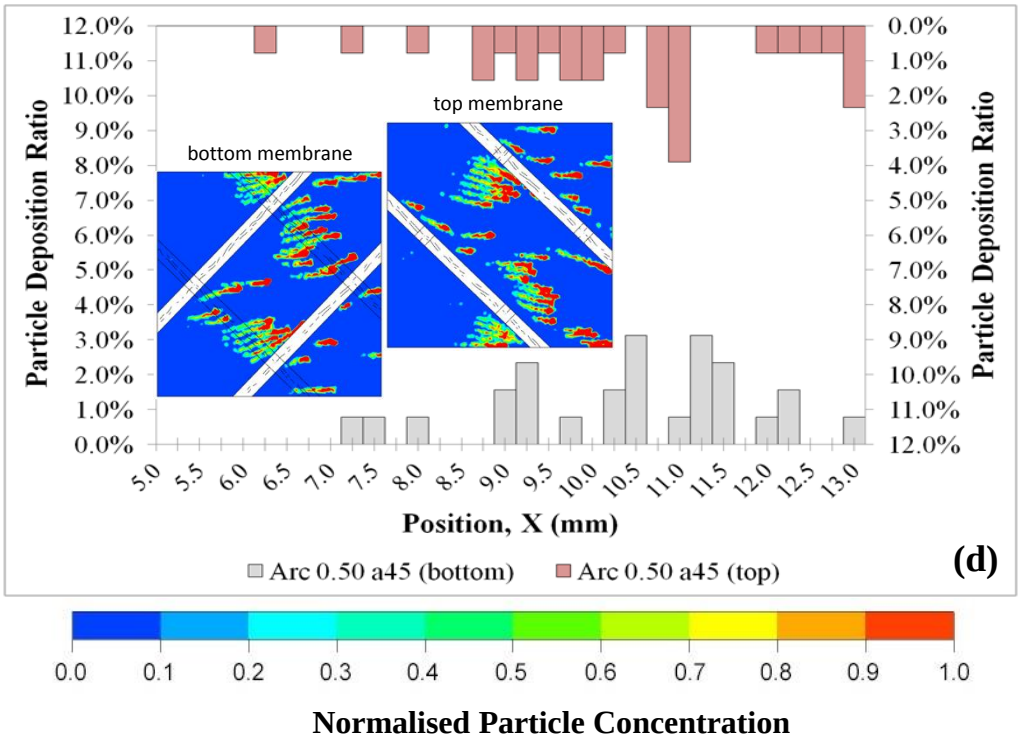

Figure 4.58: Spatial distribution of particles and particle deposition ratios on top and bottom membrane surfaces across channel length for Arc 0.50 spacer with flow attack angle of (a) 90°, (b) 15°, (c) 30° and (d) 45°.

CHAPTER 5

CONCLUSIONS AND RECOMMENDATIONS

5.1 Conclusions

In the present work, two-dimensional (2D) and three-dimensional (3D) models using computational fluid dynamics (CFD) approach to study the flow hydrodynamics, concentration polarisation and fouling behaviours in a narrow spacer-filled channel were investigated. The research delivered flow visualisation that aided in the understanding and developing insights into the flow patterns that could affect concentration polarisation and fouling phenomena. The research also successfully investigated the effects of spacer shape and flow attack angle on mass transfer enhancement, concentration polarisation/fouling tendency and energy loss.

A total of twelve spacer shapes and four flow attack angles were investigated in this work and the results showed that spacers with Circle, Oval-B tilt, T026deg and Arc 0.50 shapes were among the spacers that gave lower pressure drop. In terms of mass transfer coefficient, the modification of triangular spacer shapes were slightly superior to the modification of square spacer shapes with better concentration polarisation control. Finally, Triangle and Square shape spacers were among the better designs to prevent particles from early deposition

on the membrane, followed by Arc 0.25 and Arc 0.50 shapes. This finding might imply that sharp edges of a spacer can aid in mitigating fouling, but the drawback is that it yields higher energy consumption.

The investigations on the effect of Reynolds number (*Re*) showed that the distance the particle travelled before deposition on a membrane surface is linearly proportional to the feed Reynolds number, whereas the decrease of average concentration factor becomes less significant as *Re* increases. The results also revealed that the pressure drop per unit length increases as *Re* increases, and the increase in the pressure gradient is faster than the decrease in the average concentration polarisation. These results suggested the need of a trade-off between the increases in feed velocity (to reduce concentration polarisation and particle deposition) and the increases in pressure drop (which causes the increase in energy consumption) across a membrane module.

Power law correlation between Sherwood number versus Reynolds number was found to be $Sh \propto Re^{0.39}$ and correlation between power number and Reynolds number is $Pn \propto Re^{0.23}$. Both correlations are in good agreement with the range reported in previous literatures (Fimbres-Weihs, Wiley and Fletcher, 2006; Amokrane, et al., 2015a; Haaksman, et al., 2017; Kavianipour, Ingram and Vuthaluru, 2017).

Taking all of the above into consideration, Arc 0.50 shape spacer with flow attack angle of 45° appeared to be the best design among all the spacers investigated in this work, where it demonstrated potential in improving the

performance of membrane processes by having a good balance between energy consumption and a better control on concentration polarisation and fouling.

5.2 Recommendations for Future Works

Currently, the adoption of feed spacers with a variety of designs aiming at concentration polarisation and fouling mitigation show great potential in spiral-wound membrane module operations. The current 3D computational domain can be further expanded axially to include more spacer filaments along the main flow direction in the channel so as to investigate the evolution of concentration polarisation and fouling behaviours further down the channel which may not be periodic. The computational domain can also be expanded in the transverse direction and includes the curvature of the channel in the study. Li, et al. (2012) had noted earlier in their work that there are inherent changes in the particle deposition profile due to variations in curvature of the spacer-filled channel. Thus, further studies on the curvature of a spacer-filled channel can improve the understanding of its influence on concentration polarisation phenomenon, apart from particle deposition.

By increasing the computational domain to include more spacer filaments either axially or transversely, more filament arrangements can be further investigated, for example, partially woven or fully woven spacers. As per the findings by Gu, Adjiman and Xu (2017), their circular shaped fully woven spacer, despite having higher pressure drop, can outperform other spacer arrangements in

terms of lower concentration polarisation and higher flux. Noting the advantages of fully woven spacer, further attention can be given to modify the shape of a fully woven spacer with the expectations to achieve lower pressure drop and improve resistance to concentration polarisation and fouling.

REFERENCES

Abid, H.S., Johnson, D.J., Hashaikeh, R. and Hilal, N., 2017. A review of efforts to reduce membrane fouling by control of feed spacer characteristics. *Desalination*, 420, pp. 384-402.

Ahmad, A.L. and Lau, K.K., 2006. Impact of different spacer filaments geometries on 2D unsteady hydrodynamics and concentration polarization in spiral wound membrane channel. *Journal of Membrane Science*, 286, pp. 77-92.

Ahmad, A.L. and Lau, K.K., 2007. Modeling, Simulation, and Experimental Validation for Aqueous Solutions Flowing in Nanofiltration Membrane Channel. *Industrial & Engineering Chemistry Research*, 46, pp.1316-1325.

Ahmad, A.L., Lau, K.K. and Abu Bakar, M.Z., 2005. Impact of different spacer filament geometries on concentration polarization control in narrow membrane channel. *Journal of Membrane Science*, 262, pp. 138-152.

Ahmad, A.L., Lau, K.K., Bakar, M.Z.A. and Shukor, S.R.A., 2005. Integrated CFD simulation of concentration polarization in narrow membrane channel. *Computers and Chemical Engineering*, 29, pp. 2087–2095.

Amokrane, M., Sadaoui, D., Koutsou, C.P., Karabelas, A.J. and Dudeck, M., 2015a. A study of flow field and concentration polarization evolution in membrane channels with two-dimensional spacers during water desalination. *Journal of Membrane Science*, 477, pp. 139-150.

Amokrane, M., Sadaouia, D., Dudeckb, M. and Koutsou, C.P., 2015b. New spacer designs for the performance improvement of the zigzag spacer configuration in spiral-wound membrane modules. *Desalination and Water Treatment*, 57(12), pp. 1-9.

ANSYS® FLUENT® Theory Guide, (2016). Released 17.0, ANSYS, Inc.

Baker, R.W., 2012. *Membrane Technology and Applications*. 3rd ed. New York: John Wiley & Sons, Inc.

Bucs, S.S., Linares, R.V., Marston, J.O., Radu, A.I., Vrouwenvelder, J.S. and Picioreanu, C., 2015. Experimental and numerical characterization of the water flow in spacer-filled channels of spiral-wound membranes. *Water Research*, 87, pp. 299-310.

Cao, Z., Wiley, D.E. and Fane, A.G., 2001. CFD simulations of net-type turbulence promoters in a narrow channel. *Journal of Membrane Science*, 185(2), pp. 157-176.

Chaumeil, F. and Crapper, M., 2013. DEM simulations of initial deposition of colloidal particles around non-woven membrane spacers. *Journal of Membrane Science,* 442, pp. 254-263.

Da Costa, A.R., Fane, A.G. and Wiley, D.E., 1994. Spacer characterization and pressure drop modelling in spacer-filled channels for ultrafiltration. *Journal of Membrane Science,* 87, pp. 79-98.

Dendukuri, D., Karode, S.K., Kumar, A., 2005. Flow visualization through spacer filled channels by computational fluid dynamics-II: improved feed spacer designs. *Journal of Membrane Science*, 249(1-2), pp. 41-49.

Drioli, E. and Giorno, L., 2010. *Comprehensive Membrane Science and Engineering, Volume 1: Basic Aspects of Membrane Science and Engineering*. Amsterdam: Elsevier.

Fimbres-Weihs, G.A. and Wiley D.E., 2010. Review of 3D CFD modeling of flow and mass transfer in narrow spacer-filled channels in membrane modules. *Chemical Engineering and Processing*. 49(7), pp. 759-781.

Flectcher, D. and Wiley, D.E., 2004. A computational fluids dynamics study of buoyancy effects in reverse osmosis. *Journal of Membrane Science,* 245, pp. 175-181.

Fimbres-Weihs, G.A., Wiley, D.E. and Fletcher, D.F., 2006. Unsteady flows with mass transfer in narrow zigzag spacer-filled channels: A numerical study. *Industrial & Engineering Chemistry Research,* 45, pp. 6594–6603.

Geraldes, V., Semião, V. and de Pinho, M.N., 2001. Flow and mass transfer modelling of nanofiltration *Journal of Membrane Science,* 191, pp. 109–128.

Geraldes, V., Semião, V. and de Pinho, M.N., 2002. Flow management in nanofiltration spiral wound modules with ladder-type spacers. *Journal of Membrane Science,* 203(1-2), pp. 87-102.

Geraldes, V., Semião, V. and de Pinho, M.N., 2004. Concentration polarisation and flow structure within nanofiltration spiral-wound modules with ladder-type spacers. *Computers & Structures*, 82(17-19), pp. 1561-1568.

Giwa, A. and Ogunribido, A., 2012. The Application of Membrane Operations in the Textile Industry: A Review. *British Journal of Applied Science & Technology*, 2(3), pp. 296-310.

Gu, B., Adjiman, C.S. and Xu, X.Y., 2017. The effect of feed spacer geometry on membrane performance and concentration polarisation based on 3D CFD simulations. *Journal of Membrane Science*, 527, pp. 78-91.

Guillen, G. and Hoek, E.M.V., 2009. Modeling the impacts of feed spacer geometry on reverse osmosis and nanofiltration processes. *Chemical Engineering Journal*, 149(1-3), pp. 221-231.

Gurreri, L., Tamburini, A., Cipollina, A., Micale, G. and Ciofalo, M., 2016. Flow and mass transfer in spacer-filled channels for reverse electrodialysis: a CFD parametrical study, *Journal of Membrane Science*, 497, pp. 300-317.

Haaksman, V.A., Siddiqui, A., Schellenberg, C., Kidwell, J., Vrouwenvelder, J.S. and Picioreanu, C., 2017. Characterization of feed channel spacer performance using geometries obtained by X-ray computed tomography. *Journal of Membrane Science*, 522, pp. 124-139.

Karabelas, A.J., Kostoglou, M. and Koutsou, C.P., 2015. Modeling of spiral wound membrane desalination modules and plants – review and research priorities. *Desalination*, 356, pp. 165-186.

Karabelas, A.J., Koutsou, C.P. and Sioutopoulos, D.C., 2018. Comprehensive performance assessment of spacers in spiral-wound membrane modules accounting for compressibility effects. *Journal of Membrane Science*, 549, pp. 602-615.

Karode, S.K. and Kumar, A., 2001. Flow visualization through spacer filled channels by computational fluid dynamics I. Pressure drop and shear rate calculations for flat sheet geometry. *Journal of Membrane Science*, 193(1), pp. 69-84.

Kavianipour, O., Ingram, G.D. and Vuthaluru, H.B., 2017. Investigation into the effectiveness of feed spacer configurations for reverse osmosis membrane modules using computational fluid dynamics. *Journal of Membrane Science*, 526, pp. 156-171.

Kavianipour, O., Ingram, G.D. and Vuthaluru, H.B., 2019. Studies into the mass transfer and energy consumption of commercial feed spacers for RO membrane modules using CFD: Effectiveness of performance measures. *Chemical Engineering Research and Design*, 141, pp. 328-338.

Koutsou, C.P. and Karabelas, A.J., 2015. A novel retentate spacer geometry for improved spiral wound membrane (SWM) module performance. *Journal of Membrane Science*, 488, pp.129-142.

Koutsou, C.P., Yiantsios, S.G. and Karabelas, A.J., 2007. Direct numerical simulation of flow in spacer-filled channels: Effect of spacer geometrical characteristics. *Journal of Membrane Science*, 291, pp. 53-69.

Koutsou, C.P., Yiantsios, S.G. and Karabelas, A.J., 2009. A numerical and experimental study of mass transfer in spacer-filled channels: Effects of spacer

geometrical characteristics and Schmidt number. *Journal of Membrane Science*, 326(1), pp. 234-251.

Lau, K.K., Abu Bakar, M.Z., Ahmad, A.L. and Murugesan, T., 2009. Feed spacer mesh angle: 3D modeling, simulation and optimization based on unsteady hydrodynamic in spiral wound membrane channel. *Journal of Membrane Science*, 343(1), pp. 16-33.

Lau, K.K., Abu Bakar, M.Z., Ahmad, A.L. and Murugesan, T., 2010. Effect of Feed Spacer Mesh Length Ratio on Unsteady Hydrodynamics in 2D Spiral Wound Membrane (SWM) Channel. *Industrial & Engineering Chemistry Research*, 49, pp. 5834-5845.

Li, F., Meindersma, W., de Haan, A.B. and Reith, T., 2004. Experimental validation of CFD mass transfer simulations in flat channels with non-woven net spacers. *Journal of Membrane Science*, 232, pp. 19-30.

Li, W., Chen, K.K., Wang, Y.N., Krantz, W.B., Fane, A.G. and Tang, C.Y., 2016. A conceptual design of spacers with hairy structures for membrane processes. *Journal of Membrane Science*, 510, pp. 314-325.

Li. Y.L., Chang, T.H., Wu, C.Y., Chuang, C.J. and Tung, K.L., 2006. CFD analysis of particle deposition in the spacer-filled membrane module. *Journal of Water Supply: Research and Technology*, 55.7-8, pp. 589-601.

Li. Y.L., Tung, K.L., Chen, Y.S. and Hwang, K.J., 2012. CFD analysis of the initial stages of particle deposition in spiral-wound membrane modules. *Desalination*, 287, pp. 200-208.

Nath, K., 2017. *Membrane Separation Processes*. 2nd ed. Prentice Hall

Neal, P.R., Li, H., Fane, A.G. and Wiley, D.E., 2003. The effect of filament orientation on critical flux and particle deposition in spacer-filled channels. *Journal of Membrane Science*, 214(2), pp. 165-178.

Radu, A.I., van Steen, M.S.H., Vrouwenvelder, J.S., van Loosdrecht, M.C.M. and Picioreanu, C., 2014. Spacer geometry and particle deposition in spiral wound membrane feed channels. *Water Research*, 64, pp. 160-176.

Rahimi, M., Madaeni, S., Abolhasani, M. and Alsairafi, A., 2009. CFD and experimental studies of fouling of a microfiltration membrane. *Chemical Engineering and Processing*, 48, pp. 1405-1413.

Ranade, V. and Kumar, A., 2006. Fluid dynamics of spacer filled rectangular and curvilinear channels. *Journal of Membrane Science*, 271, pp. 1-15.

Saeed, A., Vuthaluru, R., Yang, Y. and Vuthaluru, H.B. 2012. Effect of feed spacer arrangement on flow dynamics through spacer filled membranes. *Desalination*, 285, pp. 163-169.

Saeed, A., Vuthalurub, R. and Vuthalurub, H.B., 2015. Investigations into the effects of mass transport and flow dynamics of spacer filled membrane modules using CFD. *Chemical Engineering Research and Design*, 93, pp. 79-99.

Schock, G. and Miquel, A., 1987. Mass transfer and pressure loss in spiral wound modules. *Desalination*. 64, pp. 339-352.

Schwinge, J., Neal, P.R., Wiley, D.E., Fletcher, D.F. and Fane, A.G., 2004a. Spiral wound modules and spacers; review and analysis. *Journal of Membrane Science*, 242, pp. 129-153.

Schwinge, J., Wiley, D.E. and Fane, A.G., 2004b. Novel spacer design improves observed flux. *Journal of Membrane Science*, 229, pp. 53-61.

Schwinge, J., Wiley, D.E. and Fletcher, D.F., 2002a. A CFD study of unsteady flow in narrow spacer-filled channels for spiral-wound membrane modules. *Desalination*, 146, 195-201.

Schwinge, J., Wiley, D.E. and Fletcher, D.F., 2002b. Simulation of the flow around spacer filaments between narrow channel walls. 1. Hydrodynamics. *Industrial & Engineering Chemistry Research*, 41, pp. 2977–2987.

Schwinge, J., Wiley, D.E. and Fletcher, D.F., 2002c. Simulation of the Flow around Spacer Filaments between Channel Walls. 2. Mass-Transfer Enhancement. *Industrial & Engineering Chemistry Research*, 41(19), pp. 4879-4888.

Schwinge, J., Wiley, D.E. and Fletcher, D.F., 2003. Simulation of Unsteady Flow and Vortex Shedding for Narrow Spacer-Filled Channels. *Industrial & Engineering Chemistry Research*, 42(20), pp. 4962-4977.

Shakaib, M., Hasani, S.M.F. and Mahmood, M., 2007. Study on the effects of spacer geometry in membrane feed channels using three-dimensional computational flow modeling. *Journal of Membrane Science*, 297(1-2), pp. 74-89.

Shakaib, M., Hasani, S.M.F. and Mahmood, M., 2009. CFD modeling for flow and mass transfer in spacer-obstructed membrane feed channels. *Journal of Membrane Science*, 326, pp. 270-284.

Siddiqui, A., Farhat, N., Bucs, S.S., Linares, R.V., Picioreanu, C., Kruithof, J.C., van Loosdrecht, M.C.M., Kidwell, J. and Vrouwenvelder, J.S., 2016. Development and characterization of 3D-printed feed spacers for spiral wound membrane systems. *Water Research*, 91, pp. 55-67.

Subramani, A., Kim, S. and Hoek., M.V., 2006. Pressure, flow, and concentration profiles in open and spacer-filled membrane channels. *Journal of Membrane Science,* 277, pp. 7-17.

Teoh, H.C. and Lai, S.O., 2014. Study of the effect of spacer orientation and shape in membrane feed channel using CFD modelling. *Jurnal Teknologi*,70(2), pp.47-53.

Wardeh, S. and Morvan, H.P., 2008. CFD simulations of flow and concentration polarization in spacer-filled channels for application to water desalination. *Chemical Engineering Research and Design,* 86(10), pg. 1107-1116.